Absorbed dose assessment in the presence of tissue heterogeneities in external radiotherapy

Doctoral dissertation

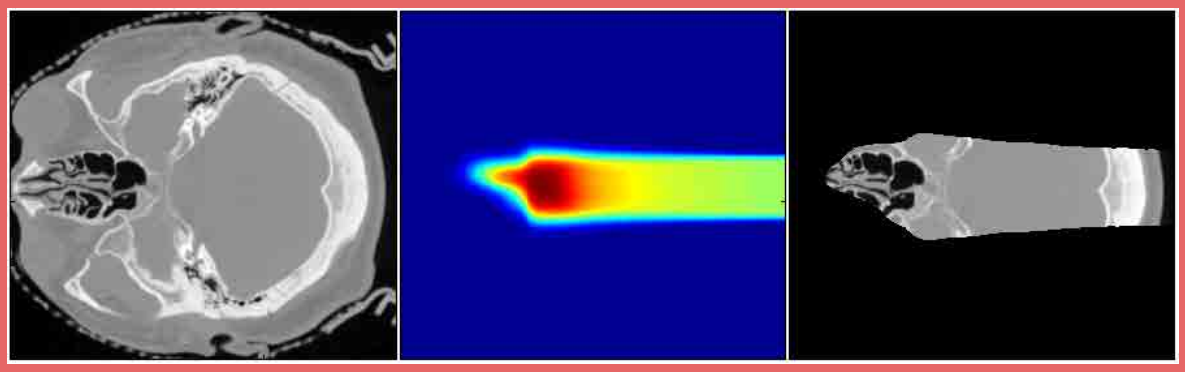

Marta Bueno Vizcarra

Supervisor: Dr. Maria Amor Duch

PhD in Biomedical Engineering

December 2013

UNIVERSITAT POLITÈCNICA DE CATALUNYA
BARCELONATECH
Institut de Tècniques Energètiques

Absorbed dose assessment in the presence of tissue heterogeneities in external radiotherapy

Marta Bueno Vizcarra

Doctoral dissertation

December 2013

Institut de Tècniques Energètiques

Universitat Politècnica de Catalunya

A mi familia.

Acknowledgements

I feel deeply fortunate for having had such amazing people around along this bittersweet period of my life. I would most likely not have been able to do it without the support of many people.

Foremost, I would like to express my sincere gratitude to my advisor, Maria Amor Duch, without whose motivation and encouragement I would not have completed my doctoral graduate training. I deeply appreciate her time, guidance, assistance and aid throughout the development of this thesis. She offered me her immense knowledge and expertise; she was always open to suggestions and she respectfully considered my ideas. She pushed me to become an independent researcher while closely examining my work and being supportive at all levels. Above all, I want to thank her for the trust and confidence bestowed upon me, her understanding and patience, her willingness, unwearying kindness and persevering helpfulness. I am extremely grateful for her unconditional support along these last years. She was the greatest supervisor I could have had.

I also want to thank my colleagues at the Institut de Tècniques Energètiques for making the institute a pleasant place to work in. I want to highlight the support of my officemates and friends Adela, Imma, Luis, Consuelo and Sara. They turned the hardships into laughs and made the happy moments all more satisfying. I am profoundly glad I could share part of my time with them and I really appreciate their helpfulness.

A very special thanks goes to Prof. Harald Paganetti. I deeply acknowledge his warm embrace to the group from the very beginning and his guidance and support throughout my stay at the Massachusetts General Hospital in Boston. Harald was an exceptional mentor; he supervised my work and steered me in the right direction while allowing me to come up with new ideas and work on my own. I sincerely thank him for sharing his vast knowledge in proton therapy as well as for his hospitality, willingness and endless patience. I am very thankful for having had the opportunity to be part of such brilliant group. Working at Harvard Gardens was one of the most fulfilling, profitable and rewarding experiences I have ever had, both from a professional and a personal point of view. I thank all my colleagues (and also friends) from Harvard

Gardens for the fruitful discussions on proton physics and programming, for generating such magical atmosphere in the carpeted cubicles, and for the comforting and restorative afterwork Sam Season's: Nick, Clemens, Chul-Hee... Among all, I would like to specially acknowledge Dr. Jan Schümann for being an extraordinary advisor, teacher, colleague and friend. I appreciate his expertise in C++ and Monte Carlo simulations and I am extremely glad for the chance to have worked side-by-side with him. Jan made the adventure specially successful, worthwhile, fun and pleasant.

I want to acknowledge the medical physicists from the institutions involved in this thesis work: Dr. Pablo Carrasco, Dr. Núria Jornet and Artur Latorre from the Hospital de la Santa Creu i de Sant Pau; Carles Muñoz-Montplet, Diego Jurado-Bruggeman and Sebastià Agramunt-Chaler from the Institut Català d'Oncologia Girona; and Josep Puxeu from the Institut Català d'Oncologia Barcelona. This thesis would not have been possible without their contribution. I profoundly thank them for carrying out part of the measuring campaign, for being involved in the reviewing processes of the articles this thesis gave rise to, and for offering their expertise in the clinical aspects. I am honored to have had the opportunity to work with such bright professionals.

I am very thankful to Jose María Fernández-Varea. He provided me with direction and became more of a mentor and friend than a teacher.

My deepest thanks to Carles for his unconditional support and helpfulness at all levels.

I doubt I will ever be able to convey my appreciation fully, but I owe my family my eternal gratitude: my grandma, my grandpa, my mum, my dad, my sister, my brother-in-law and my marvelous nephews Martí and Gerard, whose smiles and hugs constantly remind me how wonderful and worthy life is. They are always there for drying my tears and celebrating my successes, for cheering me up and reminding me I must believe in me.

I am profoundly grateful to my other family: my friends. A very special thanks goes to my dearly beloved Sara and Mimi; to Tania, Neus and Charline; to my ecstatic siblings Berta, Anne-Sophie, David, Albert and Jose; to my crazy physicists Xènia, Paz, Cris, Núria, Andreu, Miki and Géraldine; to the best performers ever: Marc, Ruth, Laura, etc. So many dinners, trips and conversations to be grateful for.

This thesis has been developed with the financial support from the Institute for Bioengineering of Catalonia (IBEC) and the Institut de Tècniques Energètiques, and I express my gratitude to these agencies.

Summary

The absorbed dose assessment in the presence of tissue heterogeneities in external radiotherapy is an issue that has concerned the medical physics community for almost three decades and it is still a matter of concern. Aiming to obtain dose distributions in clinically-acceptable computation times, analytical dose calculation algorithms integrated in treatment planning systems based their calculations on water-equivalent properties and elemental compositions of each material are disregarded despite the fact that radiation interaction processes strongly depend on them. This approximation provides reasonable accuracy in water-like tissues but the reliability of predicted dose distributions in the patient might be questioned when the radiation beam is traversing complex density heterogeneities, such as air, lung or bone. Experimental verification of dose calculation algorithms is essential and ionization chambers (IC) are the reference detectors for this purpose. However, correction factors to determine the absorbed dose in materials other than water are unknown for most IC types and therefore, they cannot procure reliable measurements in heterogeneous media. Monte Carlo (MC) simulations offer a high precision in dose calculation by tracking all particles individually taking into account the specific properties of each material. Unfortunately, accuracy and computation speed are inversely proportional and MC-based approaches generally entail long calculation times, unaffordable in the clinical routine. Nevertheless, for the cases where the expected errors in the predicted dose distributions during treatment planning are significant, *i.e.* when the radiation beam path is highly inhomogeneous, the benefit of resorting to MC dose calculations to achieve higher accuracy would be undoubtedly worth a presumably long computation time.

In this thesis the suitability of several detectors to accurately determine the absorbed dose in the presence of high-density heterogeneities was evaluated. Ultra-thin thermoluminescent detectors (TLDs) and radiochromic films were considered as potential candidates for entailing low perturbation effects. MC dose calculations enabled to validate and understand the experimental results. Further, both dosimetric techniques were employed to thoroughly examine the behavior of a recently-released non-analytical dose calculation algorithm (AXB)—which copes with the elemental composition of materials and thus, is claimed to yield promising results—in heterogeneous phantoms. Fi-

nally, a fast algorithm named the heterogeneity index (HI) was developed to quantify the level of patient tissue heterogeneities traversed by the radiotherapy beam. The validity of this HI to easily predict the accuracy of dose distributions based on analytical dose calculations was analyzed by evaluating the correlation between the HI and the dose uncertainties estimated by using MC as the reference.

The results show that a detector of 50 μm thickness can provide reliable absorbed dose measurements in high-density heterogeneities since perturbation correction factors are unneeded. AXB was found to provide comparable accuracy to MC dose calculations in the presence of heterogeneities but uncertainties in the material assignment procedure might lead to significant changes in the dose distributions, which deserves a word of caution when carrying out experimental verifications. Finally, HI was found to be a fast and good indicator for the accuracy of dose delivery in terms of tumor dose coverage. Accordingly, HI can be implemented in the clinical routine to decide whether or not a MC dose recalculation of the plan should be considered to ensure that dose uncertainties are kept within tolerance levels. In conclusion, this thesis work tackled the main concerns on the absorbed dose calculation and measurement in the presence of tissue heterogeneities.

Contents

List of Figures

List of Tables

List of Abbreviations

AAA	Anisotropic Analytical Algorithm
AAPM	American Association of Physicist in Medicine
ADWS	Absorbed Dose to Water Standards
AXB	Acuros XB
CCC	Collapsed Cone Convolution
CTV	Clinical Tumor Volume
DVH	Dose-Volume Histogram
EPL	Equivalent Path Length
FFF	Flattening Filter Free
GTV	Gross Tumor Volume
HI	Heterogeneity Index
HSCSP	Hospital de la Santa Creu i de Sant Pau
IAEA	International Atomic Energy Agency
IC	Ionization Chamber
ICOB	Institut Català d'Oncologia Barcelona
ICOG	Institut Català d'Oncologia Girona
ICRP	International Commission on Radiological Protection
ICRU	International Commission on Radiation Units and Measurements

IMRT Intensity Modulated Radiation Therapy

LBTE Linear Boltzmann Transport Equation

LET Linear Energy Transfer

MC Monte Carlo

MGH Massachusetts General Hospital

MU Monitor Unit

MV MegaVoltage

OAR Organs At Risk

PB Pencil Beam

PDD Percentage Depth-Dose distribution

PSF Phase-Space File

PTCOG Particle Therapy CoOperative Group

PTV Planning Tumor Volume

RBE Relative Biological Effectiveness

SOBP Spread-Out Bragg Peak

SSD Source-to-Surface distance

TLD Thermoluminescent Dosimeter

TPS Treatment Planning System

UPC Universitat Politècnica de Catalunya

VMAT Volumetric Modulated Arc Therapy

VR Variance Reduction

Chapter 1

Introduction

1.1 Cancer incidence

Cancer is a group of diseases characterized by uncontrolled growth and spread of abnormal cells that may end up forming malignant tumors. Cancer is a leading cause of death worldwide, accounting for 7.6 million deaths (around 13% of all deaths) in 2008[1]. Figure 1.1 shows the cancer incidence worldwide grouped by tumor type. The 5-year relative survival rate for all cancers diagnosed between 2002 and 2008 is 68%, up from 49% in 1975-1977, which reflects both progress in diagnosing certain cancers at an earlier stage and improvements in treatment[2].

Cancer treatment requires a careful selection of one or more intervention, such as surgery, radiotherapy, and chemotherapy—based on the tumor type, location and stage. At present, radiation therapy contributes to the cure of approximately 70% of all cancer patients, when used alone or in combination with surgery or chemotherapy-immunotherapy. This proportion illustrates the important role of radiation therapy in cancer management[3].

In radiotherapy (RT) treatments ionizing radiation is used to damage the tumor

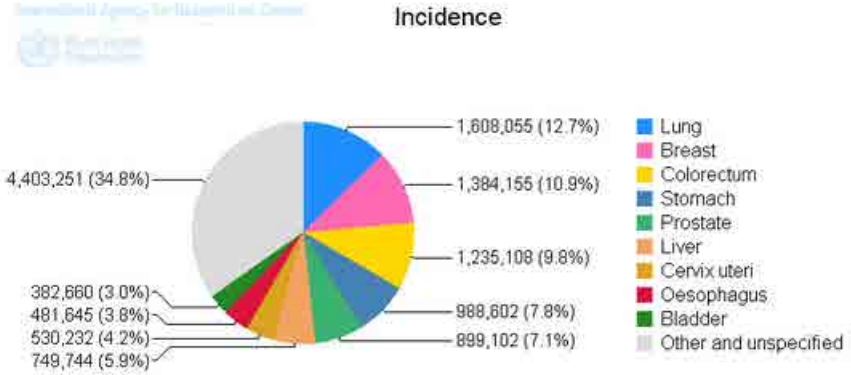

Figure 1.1: Worldwide cancer incidence. From the World Health Organization (WHO)[1], 2013.

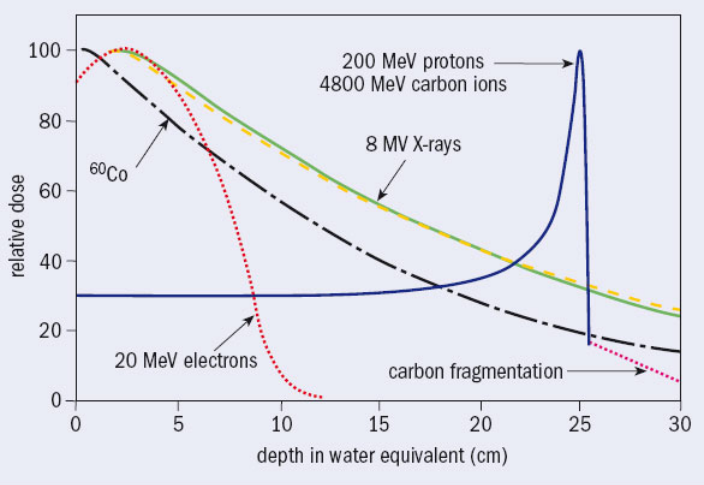

Figure 1.2: Percent depth-dose deposition curves for electron, photon, proton and carbon ion beams. From Cern Courier, International Journal of High-Energy Physics, December 6, 2006.

cells either by direct break-up of DNA structure or by indirect interactions of free radicals generated from the ionization of water followed by DNA oxidation. RT has two main modalities: external beam RT and brachytherapy[4]. In external beam RT, the radiation source is external to the patient whereas in brachytherapy radioactive seeds are placed inside the patient in direct contact with the tumor. This thesis will be focused on external beam RT treatments to which we will refer as RT for abbreviation.

1.2 RT basis

Different types of particle RT co-exist nowadays and the appropriate choice among them depends on many factors such as the type of tumor, its size and location, the patient age and the availability of the technique. Tumors can be treated with electrons, photons, protons or heavier ions beams. Characteristic dose distributions in water are depicted in figure 1.2 for all particles.

1.2.1 Megavoltage (MV) electron and photon beams

Two of the oldest and most popular modalities are MV electrons and photon beams. Both electron and photon RT beams are commonly generated by modern linear accelerators (linacs). Electrons are accelerated to kinetic energies ranging from 6 to 25 MeV using microwave radiofrequency fields. Electrons impinge on a scattering foil in order to obtain a wider beam to cover the tumor area and then a set of collimators shape the beam according to the tumor contour. The characteristic fall-off in depth of MV electron beams makes them suitable for the treatment of superficial tumors—such as skin tumors.

Figure 1.3: Linac accelerator head for electron and photon radiotherapy. From Varian Medical Systems web.

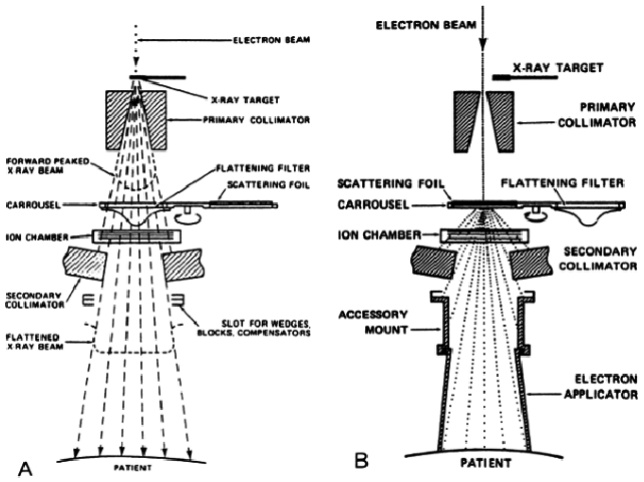

Figure 1.4: Schematic representation of the basic components of the head of a linac for photon (A) and electron (B) radiotherapy. From Khan [4].

MV photon beams are produced by the rapid deceleration of electrons in a high-density target (bremsstrahlung photons). The dose distribution in depth of MV photon beams is characterized by a steep dose gradient within the first millimeters of tissue which is known as the *build-up* region. This kind of therapy can be useful in a wide range of cases. Usually, a treatment involves several fields entering the patient from different angles, in such a way that they all aim at the tumor. A scheme of a typical accelerator gantry is shown in figure 1.3.

The main components of a linac in electron and photon mode are shown in figure 1.4. Further information about electron and photon therapy can be found elsewhere [5].

1.2.2 Proton and heavier ion beams

It was not until the beginning of the 1990's that radiation oncologists started to recognize proton therapy as a therapeutic method. By 1993 about 10,000 patients worldwide had been treated with protons. In 2010, there were 28 centers for proton therapy around the world; by the end of 2006 this has reached 50,000. Last year, the Particle Therapy Co-Operative Group (PTCOG) registered a total of 73,804 patients treated with protons since the first facility—Loma Linda (California, USA)—was built. Today five companies supply turnkey proton-therapy facilities.

The depth-dose distribution which characterizes proton's interaction with matter is known as the Bragg-peak curve, and it is very sharp for a given beam energy (see figure 1.2). Protons deposit the vast majority of their energy at the end of their trajectory—where the tumor should be located. The sharp fall-off[1] of the proton dose deposition after the Bragg-peak leads to a significant reduction in the dose deposited beyond the tumor site (see figure 1.2). All in all, the characteristic depth-dose distributions of proton beams result in a significantly reduced integral dose compared to photon treatments[6].

Two main beam delivery methods co-exist nowadays: the passive-scattering technique and the active scanning technique. In passive spreading techniques, the proton beam is spread by placing scattering material into the path of the protons. A single scatterer broadens the beam sufficiently for treatments requiring small fields. For larger fields, a second scatterer is needed to ensure a uniform dose profile. A combination of custom-made—patient-specific—collimators (commonly named apertures) and compensators conform the dose to the target volume laterally and distally, respectively (see figure 1.5). The spread out Bragg peak (SOBP), shown in shown in figure 1.6, is obtained via a set of range modulator wheels or ridge filters inside the nozzle of the delivery system.

In scanning-beam techniques, magnets deflect and steer the proton beam. Under computer control, a narrow mono-energetic beam paints the treatment volume, voxel-by-voxel, in successive layers. The depth of penetration of the Bragg peak is adjusted by varying the energy of the beam before it enters the nozzle. The delivery is done either in a step-and-shoot mode or continuously. The two techniques are described schematically in figure 1.7.

In 1975 a heavy ion therapy program began at the Lawrence Berkeley National Laboratory where, until 1992, 2054 patients were treated with helium ions and 433 with heavier ions (Ne, N, O, C, Si and Ar). Currently, heavy ion therapy is performed at three centers—two in Japan and one in Germany—using carbon ions and around 3500 patients have been treated.

Ion beams have two important features arising both from the physical aspects of

[1] The fall-off is usually considered to be the distal region of the Bragg peak where the dose decreases from 80% to 20%.

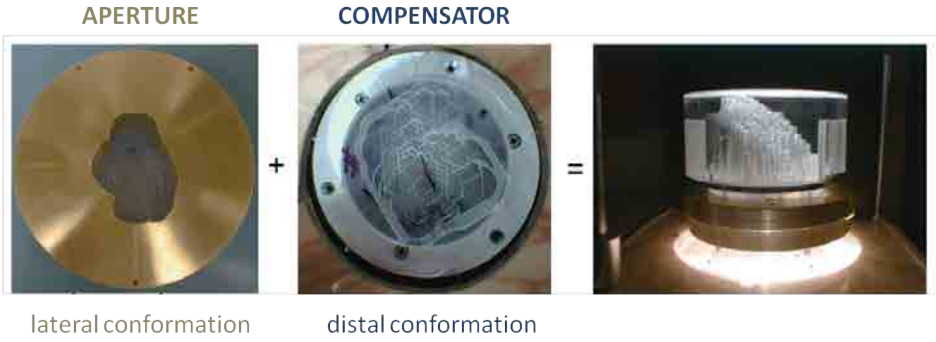

Figure 1.5: Patient-specific devices for dose conformation to the tumor in passively-scattered proton therapy fields.

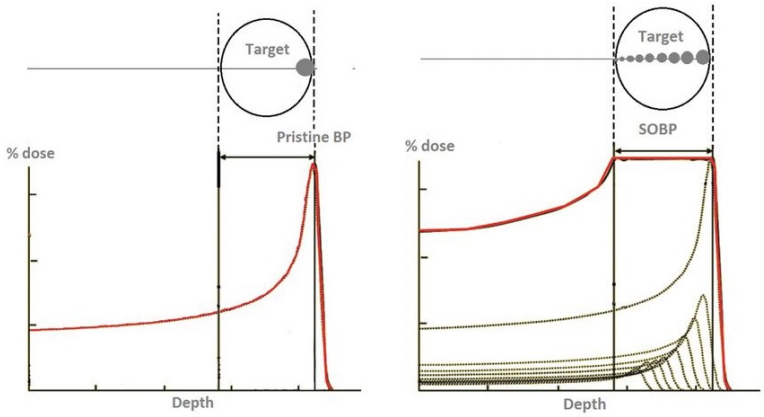

Figure 1.6: Generation of an SOBP for passively-scattered proton beams. From McGowan, Burnet, and Lomax [7].

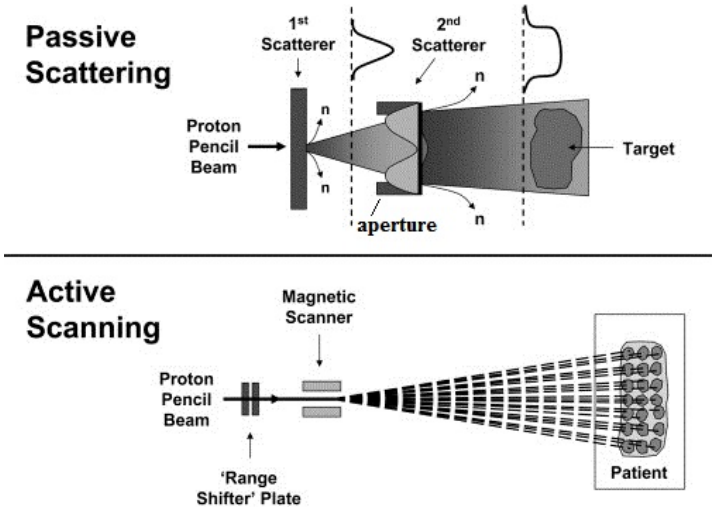

Figure 1.7: Generation of an SOBP for passively-scattered proton beams. Extracted from Hall [8].

their dose distribution in the patient and from potentially advantageous biological phenomena resulting from their high rate of energy deposition (high linear energy transfer (LET)) over a portion of the particle track which can often be located in the tumor volume. Probably the most important of these biological phenomena is a markedly increased efficiency of cell killing, *i.e.* the relative biological effectiveness (RBE[2]) of heavy ions is higher than that of protons. Thus, a lower dose is needed with heavy ion beams to produce the same cell damage. On the other hand, the main drawback of this kind of therapy is that the nuclear fragmentation of the heavy ions produces secondary charged fragments. These are responsible for the extra dose tail beyond the Bragg peak as it can be appreciated in figure 1.2. This tail might damage the healthy tissue behind the tumor during treatment.

Further information about the history and future developments of heavy ion therapy can be found elsewhere[10].

This thesis work will be focused on photon and proton RT.

1.3 Uncertainties in RT

Radiotherapy, as well as the rest of disciplines that aim to overcome cancer, undergoes continuous development in all steps involved in the treatment procedure. Technological advances in imaging and patient positioning, development of dose calculation algorithms integrated in treatment planning systems (TPS), progress in gated treatments to account for inter-fractional geometry changes in the patient and advances in delivery techniques—such as intensity-modulated radiation therapy (IMRT)—, lead to better accomplish the main goal of radiotherapy: to ensure maximum tumor coverage while sparing surrounding healthy tissues which will lead to mitigate the severity of side effects and lower the risk of secondary malignances[11].

The aforementioned areas of advance in radiotherapy are, at the same time, sources of uncertainty in the assessment of the delivered dose to the patient[12–17], *i.e.* the precision and quality of a treatment are limited by the daily reproducibility of patient positioning in the radiation field, the ability to locate and delineate the tumor volume on a planning image and the accuracy in the predicted dose distributions. A difference in absorbed dose of about 10% is detectable in tumor control, and a difference of about 7% in absorbed dose can be observed for a number of normal tissue reactions[18].

Dose uncertainties during treatment planning contribute to discrepancies in dose delivery that might lead to underdosage of the tumor and overexposure of surrounding healthy tissue. According to the ICRU, the overall uncertainty in the delivered dose to the patient should not be greater than 5%[19;20]. A further analysis of uncertainties associated with radiation treatment shows that this would require the accuracy for the

[2]RBE is defined as the ratio of a dose of a reference radiation quality (usually photons) to a dose of a test radiation (such as protons or carbon ions) to produce the same biological effect[9].

dose calculation algorithm alone to be on the order of 2%-3%. This accuracy level is generally achievable with modern TPS in water-equivalent phantoms. However, it can be verified only for a limited set of dosimetric tests, normally performed during system commissioning and as a part of a quality assurance program. Owing to the complexity of patient heterogeneities combined with a broad range of external beam treatment conditions, slightly larger errors might be expected in three-dimensional patient dose distributions.

1.4 Coping with tissue heterogeneities in the treatment planning procedure

Radiotherapy treatment planning can be described as the procedure that, taking as input a model of both the radiation beam and the patient anatomy—given usually by a computed tomography (CT)—, produces as output two kinds of information: machine instructions to deliver the treatment (such as beam energy, beam shape and number of particles to be delivered in each beam—also known as monitor units (MU)) and the expected dose distribution in the patient, which allows to quantify the probability of tumor control and of complications to the normal tissues.

In the clinics, plans are usually obtained from analytical dose calculation algorithms integrated in TPS.

1.4.1 Deficiencies of analytical dose calculations

Analytical dose calculation algorithms provide dose distributions in clinically acceptable timescales. The computation speed lies on several approximations in the dose calculation procedure. Dose calculations are based on water-equivalent properties and elemental compositions of each material are disregarded. Considering that our body is 90% water, this approach seems reasonable to a first approximation, even though interaction of radiation with matter strongly depends on the atomic composition of the medium. Analytical dose calculation algorithms provide reasonable accuracy in water-like tissues but the reliability of predicted dose distributions in the patient might be questioned when the radiation beam is traversing complex tissue heterogeneities, such as air, lung or bone, which radically differ from water in terms of density and atomic number (Z).

Analytical dose calculation algorithms are usually validated using Monte Carlo (MC) simulations and experimental measurements.

1.4.2 MC simulations

MC is a powerful and accurate tool in dose computations in RT. MC simulations are stochastic solutions to the linear Boltzmann transport equation (LBTE). The LBTE

takes the form of the partial differential equations:

$$\hat{\Omega} \cdot \vec{\nabla}\Phi^{\gamma} + \sigma_t^{\gamma}\Phi^{\gamma} = q^{\gamma\gamma} + q^{e\gamma} + q^{\gamma} \tag{1.1}$$

$$\hat{\Omega} \cdot \vec{\nabla}\Phi^{e} + \sigma_t^{e}\Phi^{e} - \frac{\partial}{\partial E}\left(S_R\Phi^{e}\right) = q^{ee} + q^{\gamma e} + q^{e} \tag{1.2}$$

Equation 1.1 describes photon (γ) transport and equation 1.2 describes electron (e) transport. $\Phi^{\gamma}\left(\vec{r}, E, \hat{\Omega}\right)$ and $\Phi^{e}\left(\vec{r}, E, \hat{\Omega}\right)$ are the photon and electron angular fluence, respectively. $\vec{r}$ is a position vector, E is the energy of the particle and $\hat{\Omega}$ is the unit direction vector. $\sigma_t^{\gamma}\left(\vec{r}, E\right)$ and $\sigma_t^{e}\left(\vec{r}, E\right)$ are the total photon and electron cross sections, respectively, and $S_R\left(\vec{r}, E\right)$ is the restricted collisional and radiation stopping power representing the continuous slowing down operator. The terms on the right hand side of equations 1.1 and 1.2 are primary and scatter source terms. q^{γ} and q^{e} are primary photon and electron source terms, respectively, $q^{\gamma\gamma}$ represents scattered photons due to photon interactions, q^{ee} represents scattered electrons due to electron interactions, $q^{e\gamma}$ represents scattered photon due to electron interactions and $q^{\gamma e}$ represents the reverse[21].

A random number generator is used to sample the interactions experienced by a particle in chronological succession. These interactions are stored in particle histories and accumulated over millions of particles to obtain the exact solution to the LBTE—apart from inherent statistical uncertainties. Thus, errors are primarily stochastic provided that reliable physical models are considered.

Unlike analytical dose calculations, MC simulations take into account the specific properties of each material, such as its atomic composition, electronic density or ionization potential. Further, MC dose calculations distinguish explicitly between electromagnetic and nuclear interactions (non-elastic interactions and multiple scattering). Hence, MC simulations yield highly-accurate dose distributions provided proper source and tissue models are available[22] and are taken as the benchmark in many situations in radiotherapy[13]. The accuracy is also limited by the finite number of particles simulated.

The development of efficient computation code and the advances in computer processor technology in recent years, have significantly enabled applications of the MC method in radiation therapy[23]. These advances have motivated several major treatment planning system vendors to embark upon the path of MC techniques. Several MC algorithms for photon, electron and/or proton have already been released—or are currently in the process of being released. Some examples for photons and electrons are the PEREGRINE system[24], the series of codes based on the Voxel Monte Carlo (VMC) (XVMC, VMC++)[25], the dose planning method (DPM)[26] or the recently developed PRIMO[27]. The VMCpro, based on the VMC, was developed for treatment planning in proton beam therapy[28]. Paganetti *et al.*[22] built a fully-MC proton dose calculation algorithm to support routine treatment planning and delivery with the GEANT4 code[29]. A further development of the code has culminated in a full TPS named TOPAS[30;31], a

TOol for PArticle Simulation.

Unfortunately, accuracy and calculation time are inversely proportional. Thus, despite offering a high precision, MC-based approaches generally entail long calculation times unaffordable in the clinical routine and are often reserved for research applications. Further, it should be born in mind the sensitivity of the MC results to the input parameters and the choice of models. In this sense, experimental measurements might be essential to procure real dose estimations provided a proper detector is available.

1.4.3 Experimental measurements

The commissioning of a therapeutic radiation beam requires reference dose measurements to calibrate the beam monitor chambers for the MU calculation, relative dose measurements to feed the TPS and field-specific dose distribution measurements to validate the dose distribution predicted by the TPS.

The general problem is expressed as follows: a detector is placed in a medium irradiated by a particle beam and yields a signal corresponding to a certain quantity of radiation or "exposure". The signal collected by the detector, M_{det}, is proportional to the energy deposited in it, and thus, so it is to the absorbed dose, D_{det}. The step from M_{det} to D_{det} at some reference conditions and radiation quality, is known as calibration.

The aim of the measurement is to determine the absorbed dose in the medium, D_{m}, as of D_{det} *in the absence of the detector*, alternatively expressed as *in the undisturbed medium*. In general, the relation between D_{det} and D_{m} is given as:

$$D_{\mathrm{med}} = D_{\mathrm{det}} \cdot s_{\mathrm{det,med}} \cdot p \tag{1.3}$$

where $s_{\mathrm{det,med}}$ is the stopping power ratio derived from the Spencer-Attix cavity theory[32] and p is the perturbation factor. The term *perturbation* is used in the sense of a perturbation by the detector of the electron fluence present at the position of interest P in uniform medium, $\Phi_{\mathrm{med}}(P)$, where the relevant fluence in the detector, inevitably a mean value over a finite volume, $\bar{\Phi}_{\mathrm{det}}$ is that which gives rise to the signal. p is a property of the detection material, the detector size and the radiation field. If the detector is small compared to the ranges of the charged particles crossing the cavity then it behaves as a Bragg-Gray detector (or a small cavity) and p is unity[33]—therefore, the conversion from D_{det} to D_{med} relies only on $s_{\mathrm{det,med}}$.

For multiple charged particles, the $s_{\mathrm{det,med}}$ is calculated as follows:

$$s_{\mathrm{det,med}} = \frac{\sum_i \int_{E^i_{\mathrm{cut}}}^{E_{\mathrm{max}}} \Phi^i_{\mathrm{det}}(E)(L_\Delta(E)/\rho)^i_{\mathrm{det}}\mathrm{d}E + \Phi^i_{\mathrm{det}}\left(E^i_{\mathrm{cut}}\right)\left(S_{\mathrm{el}}\left(E^i_{\mathrm{cut}}\right)/\rho\right)^i_{\mathrm{det}} E^i_{\mathrm{cut}}}{\sum_i \int_{E^i_{\mathrm{cut}}}^{E_{\mathrm{max}}} \Phi^i_{\mathrm{det}}(E)(L_\Delta(E)/\rho)^i_{\mathrm{med}}\mathrm{d}E + \Phi^i_{\mathrm{det}}\left(E^i_{\mathrm{cut}}\right)\left(S_{\mathrm{el}}\left(E^i_{\mathrm{cut}}\right)/\rho\right)^i_{\mathrm{med}} E^i_{\mathrm{cut}}} \tag{1.4}$$

where $i = \{p, e, \alpha, ...\}$ are all the charged particles that contribute to the dose

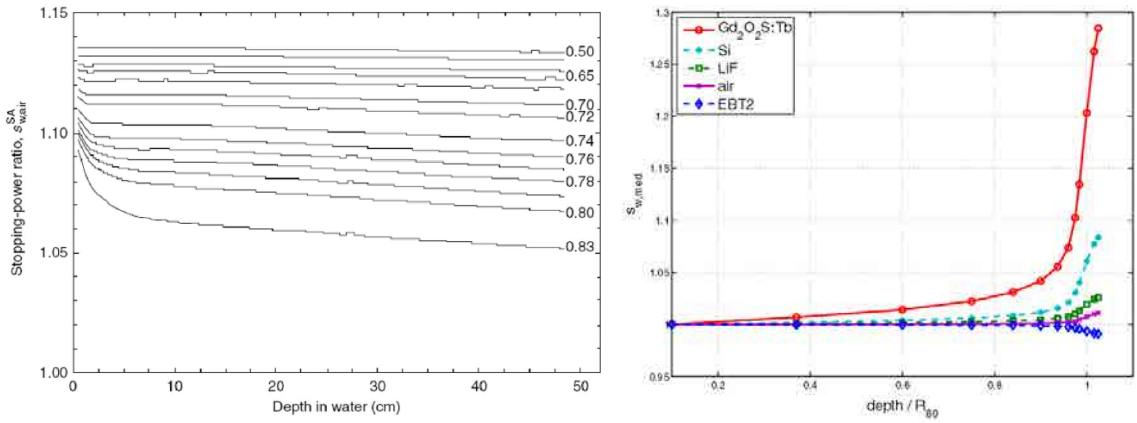

(a) photon beams (b) proton beams

Figure 1.8: Spencer-Attix $s_{\mathrm{det,med}}$ values as a function of depth for (a) photon beams of different energies (adapted from reference Andreo and Brahme[39]) and (b) a 150 MeV proton beam for different detection materials (from Gomà, Andreo, and Sempau[38]).

in the detector or cavity; E^i_{cut} is the cut-off energy of the i-th particle; $\Phi^i_{\mathrm{det}}(E)$ is the distribution of the fluence of the i-th particle in the detector with respect to the energy; and $(L_\Delta/\rho)^i_{\mathrm{med}}$ and $(S_{\mathrm{el}}/\rho)^i_{\mathrm{med}}$ are the mass linear energy transfer and the mass electronic stopping power, respectively, of the i-th particle in the medium. An upper limit for E^i_{cut} is typically defined as the mean energy of the i-th particle with a sufficient residual range to cross the cavity.

A set of stopping power ratios have been calculated over the years for different detector/medium combinations[32;34–38]. An example of Spencer-Attix $\mathrm{S_{det,med}}$ values as a function of depth for different detection materials are depicted in figure 1.8 for photon and proton beams.

According to the IAEA TRS-398[40], D_{w} under reference conditions must be measured in water with cylindrical or plane-parallel ionization chambers (IC). Dosimetry protocols provide a set of correction factors p for converting ionization into dose, but only for water-equivalent materials and at a reference depth[40;41]. The dosimetric data to obtain the dose in materials other than water, such as stopping power ratios and mass energy absorption coefficients are not given in the dosimetry protocols and the perturbation correction factors in combination with heterogeneous media are also unknown for most IC types. Hence, IC can not be used for the absorbed dose determination in media other than water if p is unknown. Recently, Araki[42] evaluated the perturbation correction factors for a PTW31010 IC for MV photon beams in heterogeneous media. The author reported that p was up to 6% in bone for 15 MV.

Despite being IC the detectors of reference in clinical dosimetry, other detectors—commonly calibrated to yield dose to water—are used in the clinical routine to assess the absorbed dose and can be useful for measurements in the presence of heterogeneities.

Radiochromic films[43] or scintillation screens, for example, are suitable for measuring lateral dose profiles given that they offer a high spatial resolution. MOSFET detectors are especially useful for *in vivo* dosimetry or high-dose gradient fields[44]. Yet they are not very common in the clinical practice, thermoluminescent dosimeters (TLDs)[45] have several advantages. Their small size (usually $\approx 1\,\text{mm}$-thick) makes them potentially good candidates for generating a low fluence perturbation factor p in MV beams—the smaller the size of the detector the lower the perturbation factor[46;47], as mentioned above. In particular, ultra-thin TLDs[48] (active layer thickness $< 100\,\mu\text{m}$)—unmatched for personal dosimetry—might be of interest in this context. Ultra-thin TLDs have been used for the dose assessment in regions of steep dose gradient, such as for skin dose measurements in high-energy photon treatments[49–51].

1.5 On the verification of dose calculation algorithms in heterogeneous media: a state of the art

The effect of heterogeneities on dose distributions mentioned in section 1.4.1 is an issue that has concerned the medical physics community for almost three decades and it is still a topic of major concern. In the literature one can find different algorithms for dose calculation used in radiotherapy treatment planning, and their fundamentals are described in great detail by Ahnesjö and Aspradakis[52], and by Papanikolaou and Stathakis[53] in a more recent study. These algorithms are based on calculations of primary photon beam attenuation and dose-deposition kernels[3] in water[52]. When using these algorithms in media other than water, a heterogeneity correction is used. Heterogeneity corrections performed to non-water materials have evolved with (i) computing speed and (ii) the understanding and modeling of the radiation transport through regions of varying density. All the algorithms have a heterogeneity pathlength correction based on the mass-density of the medium. This correction is known as the equivalent pathlength (EPL). The EPL method scales the beam dose distribution to take into account changes with depth of the primary fluence in a medium different than water.

Broadly speaking, dose calculation algorithms implemented in commercial TPS can be classified into two main groups:

- Group 1. Models primarily based on EPL for inhomogeneity corrections where (i) the electron transport is not separately modeled, and (ii) the density changes are sampled along the 1D primary rays. Pencil-beam convolution (PB) algorithms and the fast Fourier convolution algorithm (FFTC) belong to this group.

- Group 2. Models capable of treating the electron transport in an approximate

[3] A dose kernels a matrix that represents dose deposition by scattered photons and electrons generated by the initial interactions of primary photons. The kernel can be generated by measurement or by a modeling system.

way and the secondary photon transport in the medium accounting for density changes, sampled along the full three dimensions. The collapsed cone (CC) algorithm, the anisotropic analytical algorithm (AAA) and the multigrid superposition/convolution (MGS-XiO) belong to this group of "advanced" models.

A broad discussion on some of the aforementioned algorithms was done by Knöös *et al.*[54].

Up to now, many studies have been published on the dosimetric validation of dose calculation algorithms, both for photon and for proton therapy fields. MC methods and experimental measurements have been applied in the verification procedure. Before going into further details it is known that conventional dose calculation algorithms that convolute invariant kernels derived from measurements in water underpredict/overpredict the dose inside high-density/low-density materials for high-energy x-ray and proton beams. This underprediction/overprediction is due to the fact that the TPS do not model the increase/decrease of the interaction coefficient inside the bone/lung and only account for the decreased/increased transmission caused by the higher/lower density material[55].

1.5.1 On photon dose calculation algorithms

Over the years a large number of groups have explored the ability of different algorithms to manage the presence of materials different from water when computing three-dimensional dose distributions in slab phantoms[53;54;56–61]. The MGS and the FFTC algorithms have been validated against measurement with radiographic films and ion chambers[62]. Concerning CC, it has been extensively tested by several groups in various geometries against MC simulations[55;63]. Fogliata *et al.*[58] investigated the performance of most of the dose calculation algorithms mentioned in section 1.4 in non-homogeneous phantoms. They confirmed the inadequacy of the algorithms belonging to the first group defined in section 1.4, especially for small fields in low density media. For the tested algorithms belonging to the second group, their results depended on the beam energy, field size and density investigated.

Most studies to date have investigated low-density materials equivalent to lung[55;62–67], and some have studied high-Z materials, such as those that compose hip prothesis[68] or bone structures[69;70]. One of the causes of this imbalance is that lung injury appears at doses as low as 20 Gy[71], whereas bone reactions appear at higher doses in standard fractionated radiotherapy. Consequently, the misevaluation of the dose inside the lung has been a cause of concern since the early days of radiotherapy. At the present moment, misevaluation of the dose inside the bone could also be a problem in dose escalation studies, where very high doses are being delivered.

Although most of the effects in bone can be understood to be the opposite of those occurring in lung, the following three do not have a corresponding effect:

1. backscatter at the interface between water and bone,

2. the re-buildup in the interface between bone and water, and

3. the spectral change of the beam after the bone.

The first two are interface effects and they have been studied and reported[72]. The re-buildup after the interface between bone and water is a phenomenon that is less known than backscatter, and it is due to the different characteristics of the electrons generating in bone and those originating from the water close to the interface. In the water-equivalent part of the phantom, the number of electrons originating from bone decreases with depth while the number of electrons originating in water increases. The two effects are not mutually compensating, as electrons generated from bone would undergo wider-angle scattering in a higher Z material and would be ejected from the bone in a more isotropic manner. This difference generates a buildup of dose. The third effect, is observed for certain MV energies as Z increases, because of the increase in the pair production cross section[73]. None of these effects are taken into account by correction-based algorithms yet they might be significant.

Varian Medical Systems developed a non-analytical dose calculation algorithm that directly solves the LBTE iteratively named Acuros XB (AXB). A preclinical version was evaluated by Vassiliev *et al.*[21] in 2010 showing encouraging results in predicting the dose distributions in the presence of high-density and low-density tissue heterogeneities. Since then, a few studies have been published on the verification of this algorithm using either MC simulations or experimental measurements. In general, AXB has been found to be able to provide comparable accuracy to MC in clinically-acceptable computation times. However, there is still room for further investigation on the special features of the algorithm. Further discussion will be made on the state of the art regarding the validation of AXB in chapter 5.

1.5.2 On proton dose calculation algorithms

As it has been shown by several authors, the effect of multiple Coulomb scattering causes the degradation of the Bragg peak when a proton beam traverses complex inhomogeneous media[74–77] as shown in figure 1.9—in the absence of scattering, the inhomogeneities would simply shift the range of protons. This causes substantial changes in the energy spectrum of the proton fluence and therefore, in the distal fall-off width. Some studies have focused on the development of analytical models to estimate range dilution of the Bragg peak in the presence of heterogeneities[78].

PB algorithms commonly use a one-dimensional dose-scaling method of a proton pencil beam in water. Pflugfelder *et al.*[79] highlighted the deficiencies of a pencil beam algorithm for scanned proton beams when these were traversing a highly heterogeneous region in the patient. The suppression of those pencil beams going through highly

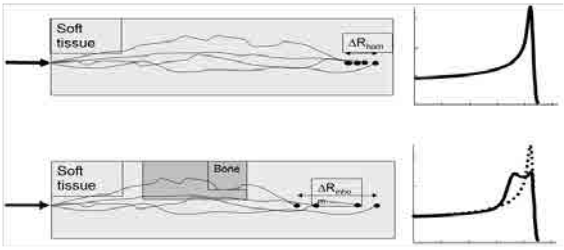

Figure 1.9: Degradation of the Bragg peak due to inhomogeneities. From Lomax [16].

inhomogeneous regions resulted in more robust plans. In a recent study, Yamashita *et al.* [80] reported significant differences between pencil beam dose calculations and MC in the distal fall-off of the SOBP and in the planning target volume coverage for a set of patients and tumor sites, owing to the presence of heterogeneities within the beam path.

Paganetti *et al.* [22] compared the dose distributions predicted by a PB algorithm [81] against MC simulations for a set of patients. In most of the studied cases, they found differences in proton ranges[4]. These differences depended on the range compensator gradient, the amount of bony anatomy in the beam path (large density variations) and the existence of air-bone-tissue interfaces—in particular if those interfaces were tangential to the beam.

Bednarz, Daartz, and Paganetti [82] presented the dosimetric limitations of the same algorithm for predicting hot and cold spots and range degradations in the target due to scattering in heterogeneities. Comparisons were done against MC simulations for small proton fields involved in stereotactic and fractionated radiotherapy treatments. Discrepancies up to 8.6% were found for one of the fields.

1.6 Absorbed dose comparisons

As mentioned in previous sections, a full comparison between dose calculation algorithms, MC simulations and experimental measurements is usually performed for verification purposes. An important feature which has not been addressed yet in this dissertation is that different clinical calculation methods may yield different quantities related to the absorbed dose for a given tissue. While MC simulations yield the dose to the tissue or medium itself, D_{m}, traditional correction-based calculation algorithms give the dose to a small water cavity within the tissue, D_{w}. However, modern convolution/superposition algorithms report D_{m} as they re-scale the interaction kernels in the traversed media. On the other hand, detectors are commonly calibrated to yield D_{w}. The conversion from one another is done by using the stopping power ratios as

[4]The *range* of a particle is known as the distance the particle travels until it has released almost all of its energy to the medium.

expressed in equation 1.4.

Several studies comparing D_m to D_w have been conducted up to now. For soft tissue the differences may be in the order of 1-2% whereas for higher density materials, such as cortical bone, the differences can be as large as 15%[36]. Dogan, Siebers, and Keall[83] retrieved large deviations—up to 8%—between D_m and D_w for head and neck and prostate IMRT plans, especially when bony structures were involved in the target volume. Walters, Kramer, and Kawrakow[84] found clinically significant differences (above 5%) between D_m and D_w in the cranium spongiosa, where the volume fraction of trabecular bone is high. A study on the approach to accurately convert the information of the MC results to D_w for proton beams—to allow comparisons against TPS—has been performed by Paganetti[85].

The question of which quantity should be adopted for comparison purposes is still under debate, as discussed by Liu and Keall[86] or Dogan, Siebers, and Keall[83]. There are strong arguments that support the use of both, D_m or D_w. Arguments in favor of changing to D_m-based protocols include: (i) the conversion from the MC-D_m to D_w adds an additional level of uncertainty due to uncertainties in computed stopping power ratios; (ii) D_m is more likely to provide a better measure of biological response; and (iii) changing to D_m will not have a clinically significant impact on most treatment protocols, since most tissues of interest are similar to water.

On the other hand, those who advocate for the usage of D_w argue that (i) all clinical experience and current dosimetry protocols are D_w-based[85]; (ii) clinical experience in terms of tumor/tissue response is based on D_w; and (iii) radiosensitive structures within cells are water-equivalent and may thus be modeled as a water cavity within the medium. Another reason that favors the latter position is that there is uncertainty in the medium type and composition when converting from CT numbers to media, potentially making the "medium" in D_m unknown[36;86;87]. Schneider, Bortfeld, and Schlegel[88] suggested an accurately method for a stoichiometric calibration of CT numbers with tissue parameters which is used in many MC algorithms for patient dose calculations. However, the calibration curve used in the clinics for converting CT numbers to electron density or relative stopping power, for photon and proton beams respectively, is CT scanner-dependent and therefore it is always a source of discrepancy between the treatment planning and the MC simulation.

Anyhow, what is beyond the shadow of a doubt is that dose distributions to be compared must be consistent with each other.

Chapter 2

Aim and Outline

The presence of tissue heterogeneities within the beam path might question the reliability of dose distributions predicted by treatment planning systems (TPS) based on analytical dose calculations. This issue has concerned the medical physics community for three decades and it is still a matter of concern.

Monte Carlo (MC)-methods can yield highly accurate dose distributions and are commonly considered the benchmark for dose calculations in radiotherapy. However, the large demand in computing time is still currently prohibitive for routine use of MC in treatment plan optimization, especially when considering highly-conformal modern delivery techniques.

In this context, Acuros XB (AXB), a deterministic Boltzmann-solver dose calculation algorithm, was recently presented as a powerful alternative to MC simulations for dose calculations in photon therapy treatments. Some studies on the dosimetric verification of the algorithm have proved the ability of AXB to provide comparable accuracy to MC even in inhomogeneous media. However, there is still room for further investigation on the features of the algorithm. No analogous dose calculation algorithm to AXB is currently available for proton beams, yet dose uncertainties during treatment planning might have detrimental consequences on the tumor coverage and organs-at-risk sparing.

On the other hand, the experimental determination of the absorbed dose is fundamental in the validation of the MC computations in reference conditions and in the verification of TPS in the clinical routine—where MC methods might not be available. It must be taken into account that both MC and TPS dose calculations might be affected by similar sources of uncertainty, such as those arising from the materials' definition (atomic composition, mean excitation energy). In this sense, experimental measurements might be essential to procure real dose estimations provided that a proper detector is available. Current dosimetry protocols for external beam radiother-

apy based on absorbed dose to water standards (ADWS) establish the determination of absorbed dose to water (D_w) in reference conditions using an ionization chamber (IC), but the correction factors for most IC in other media/tissues are unknown.

According to what is mentioned above, the **goal of this thesis** is:

to contribute to solve the current issues on the accurate absorbed dose determination in the presence of tissue heterogeneities for both photon and proton radiotherapy.

To this end, this work tackles the problem of the dose assessment in such conditions by (i) analytical algorithms, (ii) MC methods and (iii) experimental measurements. This thesis has been developed in collaboration with several catalan hospitals and a foreign institution:

Hospital de la Santa Creu i de Sant Pau (HSCSP), Barcelona, Spain.

Hospital Duran i Reynals—Institut Català d'Oncologia (ICOB), Barcelona, Spain.

Hospital Josep Trueta—Institut Català d'Oncologia (ICOG), Girona, Spain.

Massachusetts General Hospital and Harvard Medical School (MGH), Boston, USA (from February 2011 until October 2011).

The outline of this thesis is divided in four sections (objectives) gathered in four chapters in this manuscript (chapters 3-6). The tasks of each section are detailed below:

I: Obtaining of reliable MC simulations for photon and proton beams

- Geometry construction, optimization and beam commissioning in reference conditions of a Varian Clinac 2100 C/D accelerator head for MV photon beams with the PENELOPE code in combination with penEasy as the main program.
- Usage of the TOPAS platform for the simulation of an IBA proton nozzle for dose calculations in patients. Geometry construction and code commissioning had been previously carried out by the TOPAS collaboration group.

These tasks are described in chapter 3. The generated MC beams are a transversal dosimetric tool and were subsequently used for several applications in chapters 4-6.

II: Analysis of the capability of several type of ultra-thin thermoluminescent detectors (TLDs) and radiochromic films to provide reliable absorbed dose measurements for radiotherapy beams in the presence of heterogeneities

- Dosimetric characterization of the detectors for radiotherapy fields: energy dependence and linearity with dose were evaluated for a wide range of beam configurations.
- Experimental measurements in phantoms with bone-equivalent heterogeneities.
- Evaluation of the detectors' perturbation effects using MC.

The evaluation of the responses of TLDs and films is described—together with the obtaining of the MC beams—in chapter 3. This provides the basis for the development of the following mentioned tasks, described in chapter 4.

III: Evaluation of the behavior of AXB in the presence of heterogeneities

- Basic verification of the AXB dose accuracy in water.
- Experimental (TLDs and radiochromic films) and MC validation of the algorithm in phantoms with lung-equivalent and bone-equivalent heterogeneities.
- Analysis of the effect of HU fluctuations and material assignments in the final dose distributions.

This section is developed entirely in chapter 5. The generated MC photon beams and the dosimeters characterized previously were used herein.

IV: Definition of an indicator for the accuracy of dose delivery based on analytical dose calculations to identify those patients for which MC dose calculation is recommended.

- Development of a fast and easy-to-calculate algorithm—named the heterogeneity index (HI)—to quantify the lateral tissue heterogeneities within a patient traversed by a single radiotherapy beam.
- Obtaining of HI-values for several small passively-scattered proton fields involved in the treatment of a set of patients.
- Evaluation of the differences between the dose distributions predicted by an analytical dose calculation algorithm and those calculated by MC using TOPAS.
- Study of the potential correlation between the dose differences and the HI-values for all considered fields in order to be able to determine the cases for which MC should be considered to keep the dose uncertainties below the tolerance levels.

Chapter 6 is devoted to describe these tasks. The generated MC proton beams were used herein to verify the dose derived from the TPS.

Chapter 3

Multipurpose dosimetric tools

This chapter gathers the development and start-up of the dosimetric tools—Monte Carlo (MC) beams and detectors' characterization, described in chapter 2—in order to carry out the following tasks involved in this thesis work. Unless explicitly stated, the work has been done by the author of this thesis work.

3.1 Generation of MC beams

3.1.1 Obtaining of the megavoltage photon source

3.1.1.1 The photon MC code

The code PENELOPE[89;90], an acronym of PENetration and Energy LOss of Positrons and Electrons in matter, was used for the MC photon dose calculations. PENELOPE was developed at the Universitat de Barcelona and it is distributed by the Nuclear Energy Agency (NEA). It is coded in Fortran90 and it is free and open source. PENELOPE simulates the coupled transport of photons, electrons and positrons in the energy range from 50 eV to 1 GeV, and in arbitrary material.

The simulation of photon transport follows the usual analogue procedure, *i.e.* all the interaction events in a photon history are simulated in chronological succession until the photon reaches an energy lower than a user-defined threshold (the absorption energy, E_{abs}). Many-body and aggregation effects are ignored and atoms are regarded as independent. The simulation of electron and positron tracks is performed by means of a mixed algorithm. Individual "hard" elastic collisions (deflections larger than a given cut-off angle), "hard" inelastic interactions (energy loss larger than a given cut-off, $\texttt{W}_{\texttt{CC}}$) and "hard" bremsstrahlung emission (energy loss larger than a given cut-off, $\texttt{W}_{\texttt{CR}}$) are simulated by random sampling from the corresponding restricted differential cross sections. Energy straggling for inelastic and bremsstrahlung interactions is accounted for in a consistent manner. Thus, electron step size is selectable by means of user-defined parameters: $\texttt{W}_{\texttt{CC}}$, $\texttt{W}_{\texttt{CR}}$ are mentioned above; $\texttt{C}_1$ is the average angular

deflection; C_2 is the maximum average energy loss; and `dsmax` is the maximum allowed step length. Analogue collision-by-collision electron/positron simulation is performed by setting $C_1 = C_2 = W_{CC} = 0$.

The track of a particle between successive hard interactions or between a hard interaction and the crossing of an interface (*i.e.* a surface that separates two media with different compositions) is generated as a series of steps of limited length. The combined effect of all (usually many) soft interactions that occur along a step is simulated as a single "artificial" soft event (a random hinge) where the particle loses energy and changes its direction of motion. The energy loss and angular deflection at the hinge are generated according to a multiple scattering approach that yields energy loss distributions and angular distributions with the correct mean and variance (first and second moments). Secondary particles emitted with initial energy larger than the absorption energy (Monte Carlo transport cut-off) are stored, and simulated after completion of each primary track. Secondary particles are produced in direct interactions (hard inelastic collisions, hard bremsstrahlung emission, positron annihilation, Compton scattering, photoelectric absorption and pair production) and as fluorescent radiation (characteristic x-rays and Auger electrons).

PENELOPE users can adapt a steering main program in order to define the radiation source, the simulation parameters, the quantities of interest to be scored, variance-reduction (VR) techniques to be applied and report the final results. The modular general-purpose main program for PENELOPE named penEasy[91] has been employed in this thesis. It was developed at the Institut de Tècniques Energètiques (Universitat Politècnica de Catalunya) and it is both free and open source. The input file for the executable is a simple text.

3.1.1.2 Geometry construction

In PENELOPE, the geometry construction consists of a number of homogeneous bodies defined by their composition (material) and limiting quadric surfaces. In the context of this thesis a Varian Clinac 2100 C/D was simulated for two photon beam energies: 6 and 18 MV. This work is a refinement of older modelizations of the accelerator head performed by the group and includes the last updates on the dimensions of the primary collimator given by Chibani and Ma[92] for the 18 MV configuration. The elements of the accelerator head (schematized in figure 1.4) were built according to manufacturer specifications.

The geometry for the 6 MV beam consisted of 48 modules and 74 quadric surfaces. For the 18 MV, a total number of 149 modules and 198 surfaces were used. The difference in number lies basically on the flattening filter construction, which has a much complicated shape in the case of the 18 MV source.

Beam Energy (MV)	Mean e^- energy (MeV)	Energy (E) spread (MeV) (FWHM of Gaussian E distribution)	Radial intensity (cm) (FWHM of Gaussian x, y distribution)
6	6.20	0	0.15, 0.15
18	18.0	1	0.20, 0.20

Table 3.1: Electron (e^-) beam parameters for the commissioning of 6 and 18 MV photon beams.

3.1.1.3 Photon beam commissioning

Small variations of the initial electron beam parameters might strongly influence the dose distributions in the patients. There are many studies in the bibliography [93–98] that have reported the influence of: (i) the mean energy of the electron beam hitting the target, (ii) its energy spread (which is usually taken as a Gaussian distribution), (ii) its radial intensity and (iii) its angle of incidence, and they are summarized by the AAPM Task Group 105 [23].

From this publications, several conclusions can be reached. First, the radial intensity of the electron beam does not affect the depth-dose curves for the depth past maximum; variations of this parameter from 0.0 cm (pencil beam) up to 0.4 cm produce local differences on the depth-dose curves below 1% (see for example Tzedakis *et al.* [94]). On the contrary, the radial intensity of the electron beam affects the dose-profile curves considerably for large field sizes—for smaller fields, its influence is negligible. The mean energy affects both dose-profiles and depth-dose curves. Nevertheless, the effect is more visible in dose-profiles for large field sizes. Finally, the energy spread is found to have no influence either on depth-dose or on dose-profile curves.

The electron beam parameters were adjusted with a trial and error method, to match the measured data. Percent depth-dose (PDD) curves and lateral dose profiles at the depth of dose maximum were measured in a water phantom of $50 \times 50 \times 50\,\mathrm{cm}^3$ using $0.35\,\mathrm{cm}^3$ Roos ionization chamber (IC) (PTW, Freiburg, Germany) and Scanditronix PFD-3G diode, respectively, for both beam energies (6 and 18 MV) and a field size of $10 \times 10\,\mathrm{cm}^2$. The final beam parameters are listed in table 3.1.

After adjusting the field of reference, PDDs and lateral profiles were validated against experimental measurements for field sizes between $2 \times 2\,\mathrm{cm}^2$ to $20 \times 20\,\mathrm{cm}^2$. PDDs were measured in water using $0.35\,\mathrm{cm}^3$ Roos IC for the largest fields ($10 \times 10\,\mathrm{cm}^2$ and $20 \times 20\,\mathrm{cm}^2$), and $0.016\,\mathrm{cm}^3$ PinPoint 31016 IC (PTW Freiburg, Germany) for the smallest fields ($2 \times 2\,\mathrm{cm}^2$ and $5 \times 5\,\mathrm{cm}^2$). Dose profiles were measured in water with Scanditronix PFD-3G diode. The results are depicted in figures 3.1-3.2 and 3.3-3.4 for 6 and 18 MV, respectively.

Deviations between simulated PDD curves and measurements for the set of studied energies and field sizes were below 1.2% in all cases. Discrepancies in beam penumbrae—defined as the distance between the 80% and the 20% of the central axis

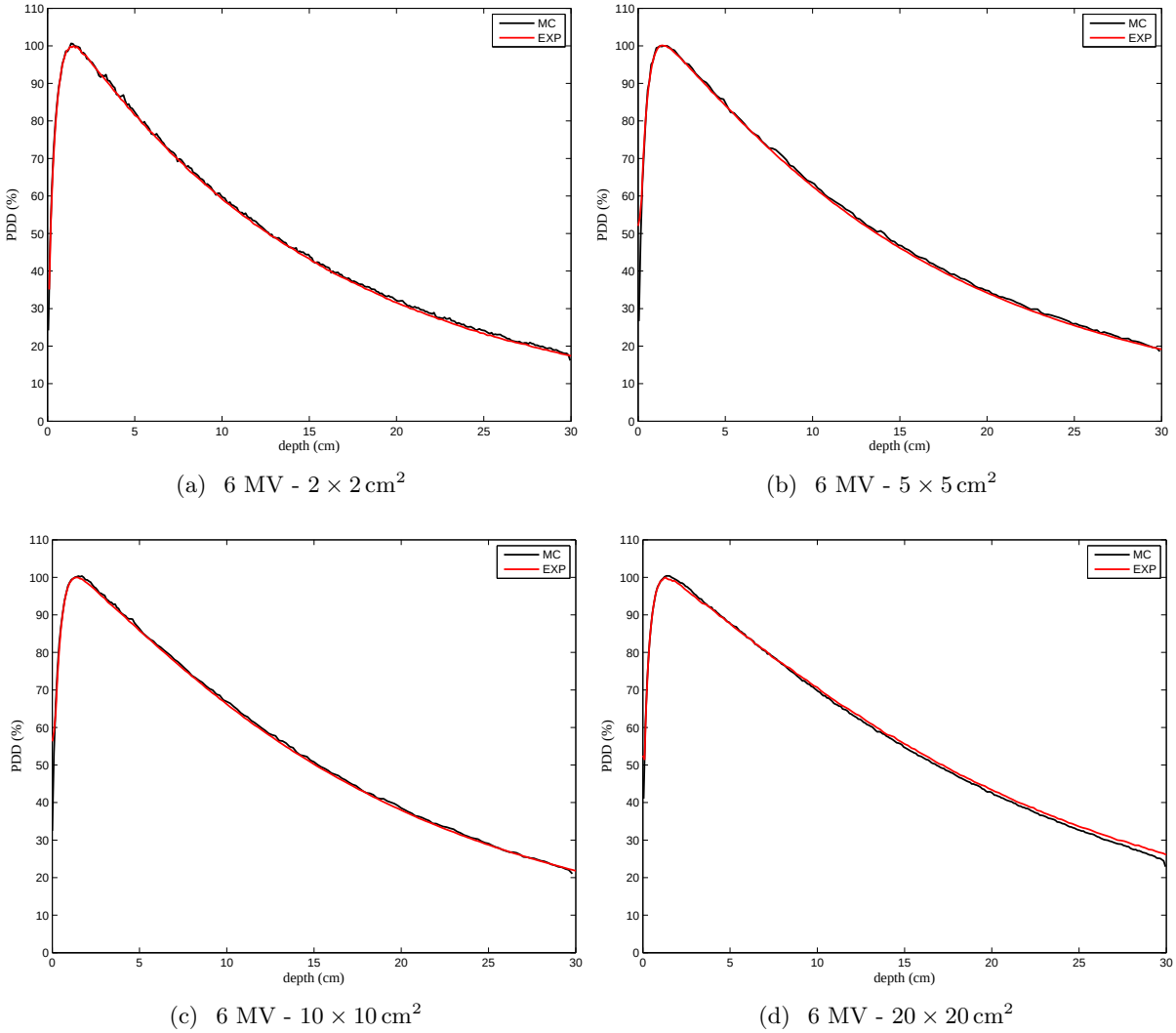

(a) 6 MV - $2 \times 2\,\mathrm{cm}^2$

(b) 6 MV - $5 \times 5\,\mathrm{cm}^2$

(c) 6 MV - $10 \times 10\,\mathrm{cm}^2$

(d) 6 MV - $20 \times 20\,\mathrm{cm}^2$

Figure 3.1: PDD curves normalized to the depth of dose maximum (1.5 cm) (i) calculated with Monte Carlo (MC) and (ii) measured experimentally (EXP) in water for the 6 MV photon beam.

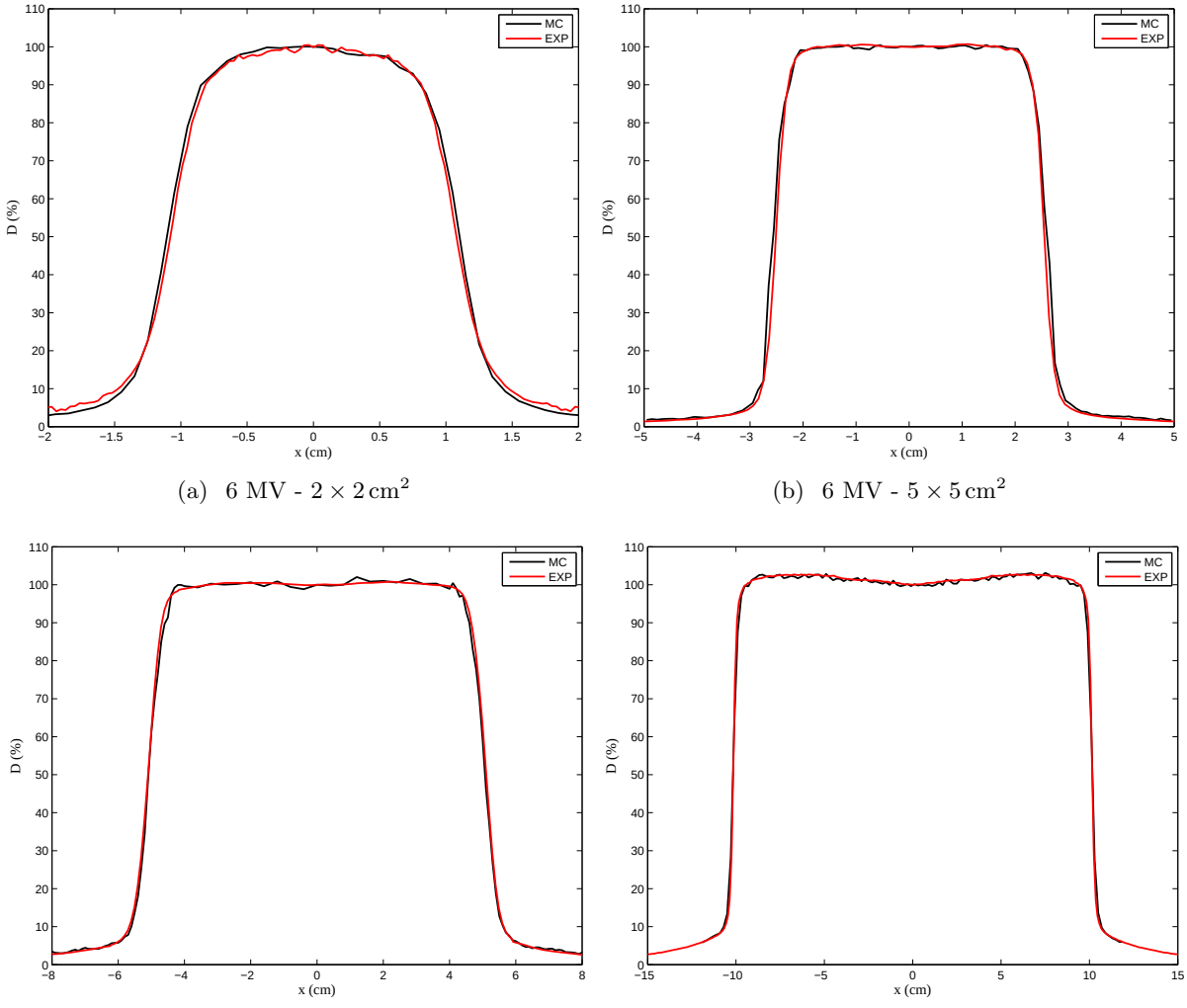

(a) 6 MV - $2 \times 2\,\mathrm{cm}^2$

(b) 6 MV - $5 \times 5\,\mathrm{cm}^2$

(c) 6 MV - $10 \times 10\,\mathrm{cm}^2$

(d) 6 MV - $20 \times 20\,\mathrm{cm}^2$

Figure 3.2: Lateral dose profiles at the depth of dose maximum (1.5 cm) (i) calculated with Monte Carlo (MC) and (ii) measured experimentally (EXP) in water for the 6 MV photon beam, normalized to the central axis value.

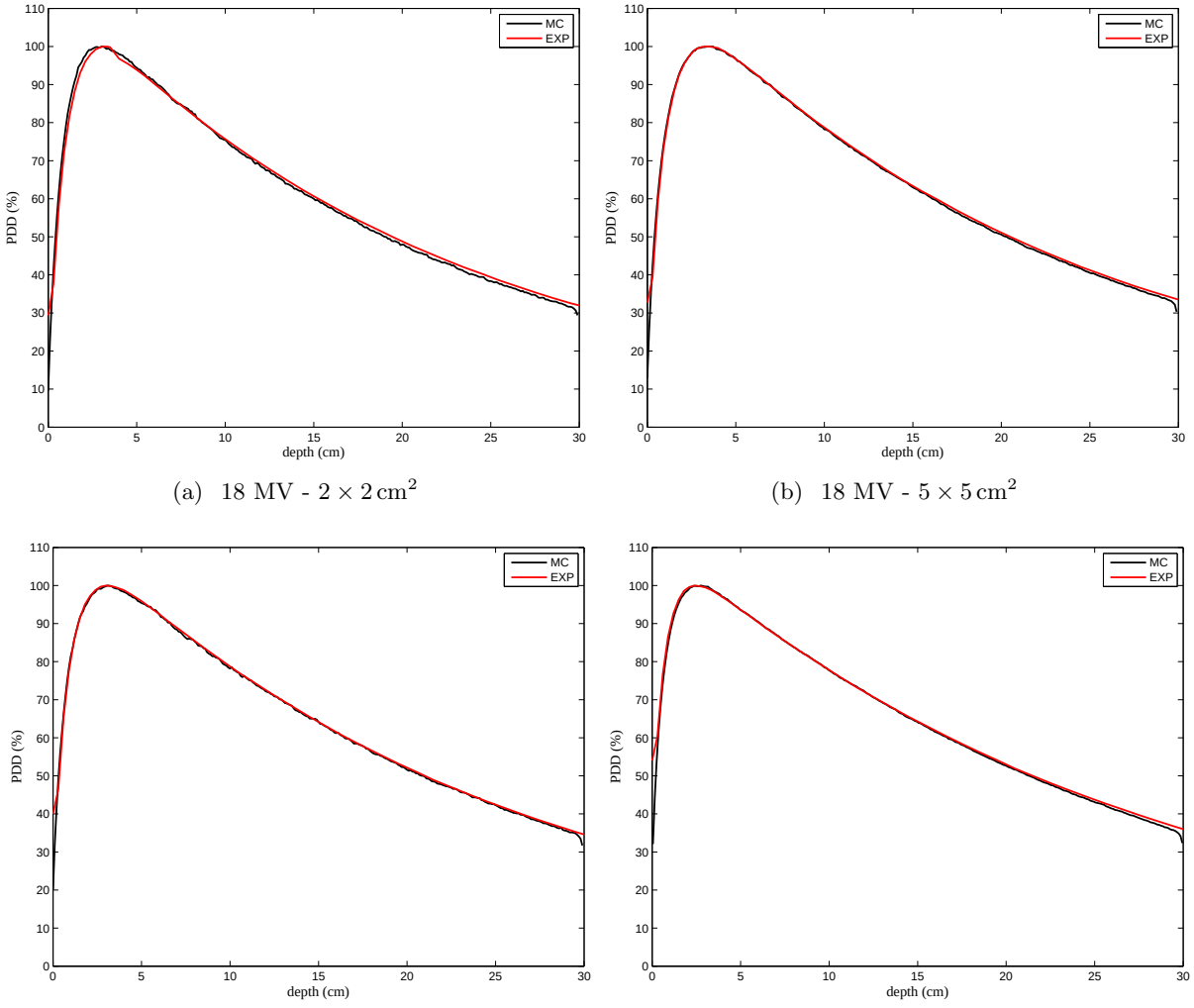

(a) 18 MV - $2 \times 2\,\mathrm{cm}^2$

(b) 18 MV - $5 \times 5\,\mathrm{cm}^2$

(c) 18 MV - $10 \times 10\,\mathrm{cm}^2$

(d) 18 MV - $20 \times 20\,\mathrm{cm}^2$

Figure 3.3: PDD curves normalized to the depth of dose maximum (3.3 cm) (i) calculated with Monte Carlo (MC) and (ii) measured experimentally (EXP) in water for the 18 MV photon beam.

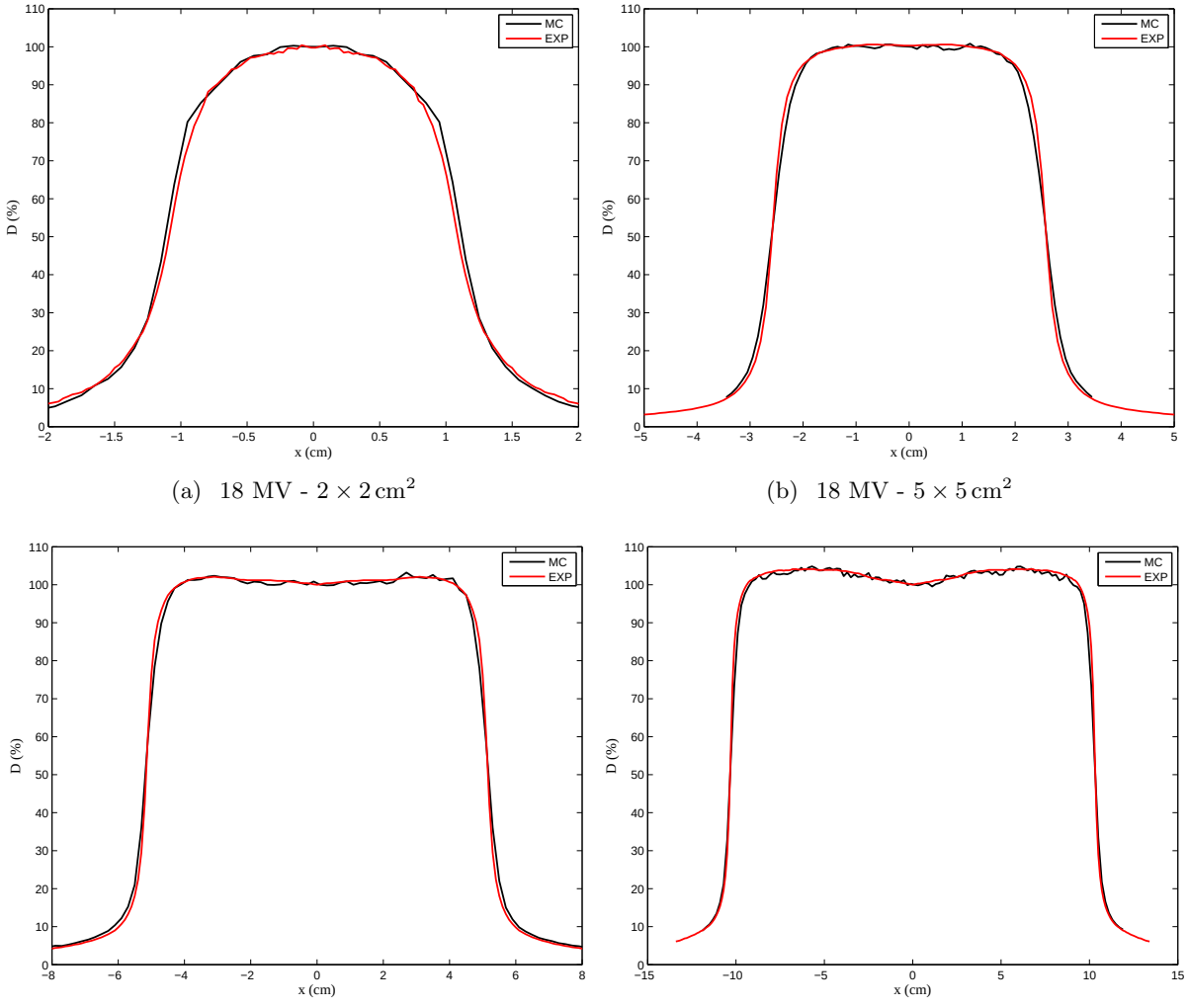

(a) 18 MV - $2 \times 2\,\mathrm{cm}^2$

(b) 18 MV - $5 \times 5\,\mathrm{cm}^2$

(c) 18 MV - $10 \times 10\,\mathrm{cm}^2$

(d) 18 MV - $20 \times 20\,\mathrm{cm}^2$

Figure 3.4: Lateral dose profiles at the depth of dose maximum (3.3 cm) (i) calculated with Monte Carlo (MC) and (ii) measured experimentally (EXP) in water for the 18 MV photon beam, normalized to the central axis value.

dose—were within 0.4 mm for all beam configurations.

3.1.1.4 Simulation in two steps

Simulations were done in two steps: first particles were tracked through the accelerator head and stopped on a plane after the secondary collimators or jaws (see figure 1.4); the particle type, energy, position and momentum are stored in a phase-space file (PSF). Then, the PSF was used as the particle source for the dose distribution calculation on the patient/phantom[99]. This enables the re-usage of the same PSF in order to improve the statistical uncertainty of the final dose computation.

3.1.2 Variance reduction techniques

A very important concept in MC simulations that will be referred throughout this manuscript is the efficiency (ϵ) of the simulation. It can be defined as follows:

$$\epsilon = \frac{1}{t\Delta^2} \tag{3.1}$$

where t is the execution time and Δ is a measurement of the uncertainty of the magnitude of interest.

An intrinsic efficiency would be defined as:

$$\epsilon_N = \frac{1}{N\Delta^2} \tag{3.2}$$

where N is the number of histories[1]. This magnitude depends on the algorithm exclusively. Combining both expressions 3.1 and 3.2, the total efficiency can be expressed as:

$$\epsilon = \epsilon_N \frac{N}{t} \tag{3.3}$$

which depends on the simulation speed (N/t, histories per second), which at the same time depends on the CPU/GPU and the compiler.

In order to speed-up the simulations and therefore improve the efficiency, the application of variance reduction (VR) techniques is strongly recommended[100]. The most popular techniques are (i) interaction forcing, (ii) Russian Roulette and (iii) particle Splitting. These techniques have been applied by many authors for the MC simulation of accelerator heads[101–103]. Their main features can be summarized as follows:

3.1.2.0.1 Interaction forcing. Sometimes, high uncertainties result from an extremely low interaction probability. In such cases, an efficient variance-reduction method is to artificially increase the interaction probability of the process A of interest, *i.e.* to

[1] A history is defined in this context as the process that involves the simulation of a primary particle and all secondary particles derived from it.

force interactions of type A to occur more frequently than for the real process. The practical implementation of interaction forcing consists of replacing the mean free path λ_A of the real process by a shorter one, $\lambda_{A,f}$. This is equivalent to increasing the interaction probability per unit path length of the process A by a factor

$$F = \frac{\lambda_A}{\lambda_{A,f}} > 1. \tag{3.4}$$

To keep the simulation unbiased, we must correct for the introduced distortion as follows: a weight $\omega = 1$ is associated with each primary particle. Secondary particles produced in forced interactions of a particle with weight ω, are given a weight $\omega_s = \omega/F$. Secondary particles generated in non-forced interactions (*i.e.* of types other than A) are given a weight equal to that of their parent particle.

Interaction forcing was applied in the target of the accelerator head to enhance the production of bremsstrahlung x-rays. Factors F=30 and F=100 were found to be the most efficient for 6 and 18 MV, respectively, in terms of number of particles stored in the phase-space plane per second. An F-value too large might slow down the simulation speed by generating particles that will never contribute to the PSF. This technique was used in combination with others, as detailed below.

3.1.2.0.2 Russian roulette and Splitting. These two techniques, which are normally used in conjunction, are effective in problems where interest is focused on a localized spatial region. The basic idea of splitting and Russian roulette methods is to favor the flux of radiation towards the region of interest and inhibit the radiation that leaves that region. As in the case of interaction forcing, variance reduction is accomplished by modifying the weights of the particles. In a normal situation, it is assumed that primary particles start moving with unit weight and each secondary particle produced by a primary one is assigned an initial weight equal to that of the primary. Splitting consists of transforming a particle, with weight ω_0 and in a certain state, into a number $S > 1$ of identical particles with weights $\omega = \omega_0/S$ in the same state. Splitting should be applied when the particle "approaches" the region of interest. The Russian roulette technique is, in a way, the reverse process: when a particle tends to move away from the region of interest it is "killed" with a certain probability, $K < 1$, and, if it survives, its weight is increased by a factor $1/(1-K)$. Here, killing means that the particle is just discarded (and does not contribute to the scores anymore). Evidently, splitting and killing leave the simulation unbiased. The effectiveness of these methods relies on the adopted values of the parameters S and K, and on the strategy used to decide when splitting and killing are to be applied. These details can only be dictated by the user's experience.

Rotational splitting[101] was carried on in a plane right before the accelerator's jaws. Other geometry-related techniques, such as the use of "skins", were used as described

elsewhere[102;103].

3.1.3 Obtaining of the proton source

3.1.3.1 The proton MC code

TOPAS[30;31], a TOol for PArticle Simulations, was used for the MC proton dose calculations. TOPAS has been developed under a collaborative project between the Massachusetts General Hospital (MGH) (Harvard Medical School, Boston, US) together with the SLAC National Laboratory (Stanford University, California, US). TOPAS incorporates the already-proven Geant4[104] simulation toolkit into a comprehensive architecture for treatment delivery system simulations and patient calculations. Treatment head geometry, patient handling, imaging and scoring are both flexible and easy to use. It is a user-friendly framework based on simple text control files. Users import DICOM, perform automatic HU conversion, use pre-defined components (range modifier wheels, propellers, steering magnets, jaws, etc.), adjust components or add new components. TOPAS handles time-dependence such as component motion and beam current modulation.

3.1.3.2 Geometry construction

The MC simulation of the treatment head (also named nozzle) was based on the information provided by the manufacturer (Ion Beam Applications SA (IBA) Louvain-la-Neuve, Belgium). Figure 3.5 shows a schematic view of the geometry of the nozzle at MGH generated by TOPAS.

The physics settings are extensively discussed and described elsewhere[22;105].

3.1.3.3 Proton beam commissioning

Paganetti *et al.*[106] in 2004 used Geant4 to shape the proton beam at MGH and it was subsequently included in the recently-developed TOPAS. The authors tested the influence of the incident proton energy, energy spread, beam spot size and beam angular distribution. The commissioning was based on a set of measured pristine Bragg curves. The most critical parameter was found to be the energy spread, since it influenced the width of the Bragg peak, the slope of the distal fall-off and the peak-to-plateau ratio.

The accuracy of TOPAS has been previously validated at MGH against experimental measurements in a variety of homogeneous and inhomogeneous phantoms[107]. TOPAS depth-dose curves were found to be within clinical required accuracy, the range being within $+1/-1.5$ mm and the modulation width within ± 3 mm of the clinical specifications. The field flatness of simulated proton dose distributions was within $\pm 2\%$ of the average dose measured in a plane transverse to the beam axis.

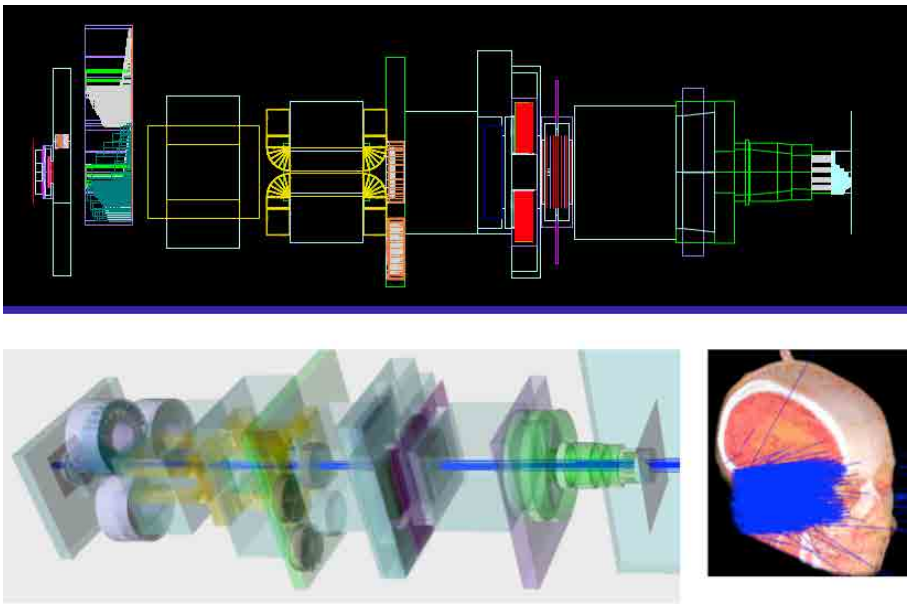

Figure 3.5: Nozzle at MGH in TOPAS.

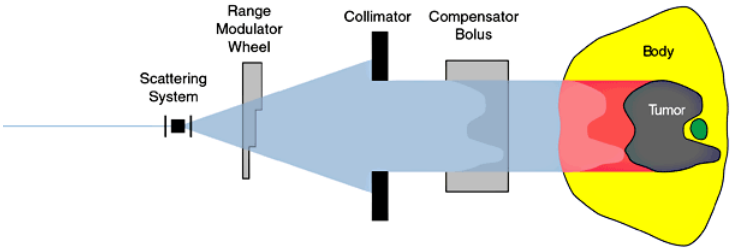

Figure 3.6: Main components of a passive-scattering proton nozzle.

3.1.3.4 Simulation in two steps

Unlike for photons, in proton therapy it is more difficult to split the calculation into a patient-independent part and a patient-specific part. The main components of a passive-scattering nozzle are schematized in figure 3.6.

The range-modulator wheel—that determines the shape of the SOBP (see figure 1.6)—, the aperture—that provides lateral conformality—, and the range compensator—that provides distal conformality (see section 1.2.2 for more information), are beam-specific. Then, the number of treatment options, and therefore the number of phase-spaces which would have to be precalculated, make the generation of a look-up database impractical. Nevertheless, the simulation is still usually split in two to allow the possibility to re-use the phase-space file several times to reduce statistical uncertainties in the final dose calculation.

3.1.3.5 Variance reduction techniques

VR techniques were implemented in TOPAS to reduce computation time and statistical uncertainties. Detailed information can be found in Ramos-Méndez *et al.*[108].

3.2 Characterization of detectors

3.2.1 Ultra-thin thermoluminescent detectors (TLD)

The most popular lithium fluoride-based (LiF) TLDs are LiF:Mg,Cu,P and LiF:Mg,Ti, also termed as MCP and MT, respectively. Three different ultra-thin TLDs were considered: two MCP-based TL detectors (MCP-Ns[48], TLD Poland and TLD-2000F[109], Conqueror Electronics Technology Co. Ltd., Beijing, China) and a ^{7}Li-enriched MT-based dosimeter (MTS-7s, TLD Poland).

MCP-Ns and MTS-7s are in the form of circular pellets of diameter 4.5 mm. Each pellet consists of two layers: a thin radiation sensitive part bonded to a thick base made of not activated LiF to which 2% of graphite was added in order to suppress any spurious luminescence. The thickness of the sensitive layer is about $8.5\,\mathrm{mg}\cdot\mathrm{cm}^2$ ($\approx 50\,\mu$m), as shown in figure 3.7. The overall thickness of the pellets is 0.933 ± 0.008 mm and 0.877 ± 0.003 mm (1 SD) for MCP-Ns and MTS-7s, respectively. The density is $\rho_{MCP} = 2.34 \pm 0.02\,\mathrm{g/cm}^3$ and $\rho_{MT} = 2.41 \pm 0.01\mathrm{g/cm}^3$ (1 SD) for MCP-Ns and MTS-7s, respectively.

TLD-2000F are $5\,\mathrm{mg/cm}^2$-thick circular films of phosphor powder (approximately $20\,\mu$m) fixed on a polyamide tape with silicon adhesive (approximately $25\,\mu$m) with a diameter of 4.5 mm[110].

MCP-Ns and TLD-2000F were microscopically analyzed on a focusing ion beam-scanning electron microscope (FIB-SEM) (Crossbeam® Neon40 Carl Zeiss) in combination with the software analySIS 5.0 (Olympus Soft Imaging Solutions GmbH). The images are depicted in figure 3.7.

The thermoluminescence was measured in a semiautomatic Harshaw 5500 reader (Thermo-Electron) and the annealing was performed in a PTW TLDO oven, for all types of TL dosimeters. The readout was always performed within 24 hours after the irradiation.

The MCP-Ns anneal cycle was set at a nominal peak temperature of 240°C for 10 min followed by a fast quench on an aluminium block. The readout was carried out in a two-step heating cycle: a preheat process at a temperature of 160°C for 10 s, and a reading phase of 20 s up to 250°C with a linear heating rate of $8^{\circ}\mathrm{C}\cdot\mathrm{s}^{-1}$.

The MTS-7s dosimeters were annealed for 1 h at 400°C followed by 2 h at 100°C. In this case, readout cycle was as follows: 10 s of preheat at a constant temperature of 135°C and 16 s of light acquisition at a heating rate of $15^{\circ}\mathrm{C}\cdot\mathrm{s}^{-1}$ to a maximum temperature of 310°C.

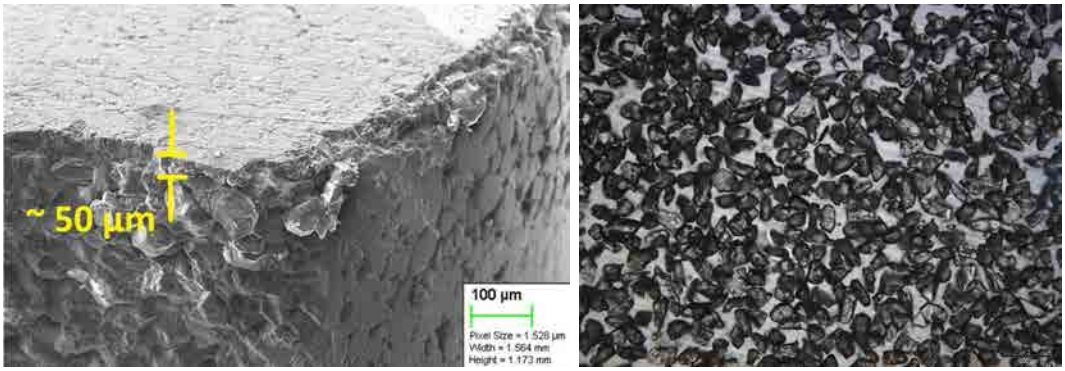

(a) (b)

Figure 3.7: Microscopical view of MCP-Ns and TLD-2000F thermoluminescent detectors.

As for MCP-Ns, anneal cycle for TLD-2000F was set at a nominal temperature of 240°C during 10 min followed by a quench on an aluminium block. The readout consisted of a preheat process at a temperature of 160°C during 10 s followed by a reading phase where detectors were heated up to 250°C at $4°C \cdot s^{-1}$.

3.2.1.1 Individual calibration factors

Detectors were calibrated in a ^{137}Cs beta source at the secondary standard laboratory of the Institute of Energy Technologies (Barcelona, Spain) to obtain individual calibration factors (CF_i): $CF_i = \bar{X}/X_i$, where X_i is the light output from dosimeter i and $\bar{X}$ is the mean light output of all the dosimeters in the batch. Detectors were subjected to several cycles of annealing, irradiation and readout in a preliminary study of stability and repeatability of the batch. Only the dosimeters that kept their CF_i between 0.9 and 1.1 (variations of $\pm 10\%$ over the mean) were considered; the others were disregarded from this study. After selecting the final group, detectors were calibrated several times in different days to ensure the stability of the batch.

MTS-7s exhibited the lowest sensitivity, which is in good agreement with other studies[111–113].

3.2.1.2 Characterization

Characterization of TLDs is required for accurate dosimetry, *i.e.* the sensitivity of the thermoluminescent (TL) material, the energy and dose responses, the stability and reproducibility of results, and thermal fading[114–116] of the detector must be evaluated for a given kind of ionizing radiation. MCP and MT dosimeters of standard thicknesses from different manufacturers have been tested along the past years to low-energy x and gamma rays[117–119], conventional megavoltage (MV) photon[47;120–122] and electron[47;123–126] beams, neutrons[127;128], alpha particles[129], beta electrons, mixed

fields[127;130–134] and high-energy particle beams (*i.e.* protons and ions)[135]. Up to now, no studies on the characterization of ultra-thin TLDs for therapeutic beams have been published. In this work we analyze the ultra-thin MCP- and MT-based TLDs behavior for MV photon and electron beams.

MCP-Ns, MTS-7s and TLD-2000F were evaluated for x-ray and electron beams from a Varian linac 2100 C/D and a Varian TrueBeam with Flattening-Filter-Free (FFF) mode (Varian, Palo Alto) at ICOB. The nominal energies selected were 6, 6FFF, 10, 10FFF 15 and 18 MV for the x-ray beams, and 6, 9, 12, 16 and 20 MeV for the electrons. We tested (i) the energy response for the specified beams and (ii) the linearity within the absorbed dose range from 0.2 up to 20 Gy for the photon beams. The response of the detectors was compared to the dose measured with a trazable 0.35 cm^3 Roos ionization chamber (IC) (PTW, Freiburg, Germany) connected to a UNIDOS electrometer (Freiburg, Germany)International Atomic Energy Agency[40] placed at the same depth than the TL dosimeter. The dose range widely covers the values typically used for patient treatments, both in conventional radiotherapy—where the dose per fraction ranges between 1.8-3 Gy—and in stereotactic treatments—where dose per fraction may be of several tens of Grays. A 10 cm by 10 cm field size was set and the TLDs were irradiated in a Plastic Water^{TM} phantom of $30 \times 30 \times 20\,cm^3$, at a depth of 10 cm for the x-ray beams and at the depth of maximum dose when irradiating with the electron beams[40]. We applied the CF_i to each dosimeter readout. In order to decrease the standard deviation (σ) of the results, nine detectors were used simultaneously in each irradiation.

Figure 3.8 shows the energy response of TLD-2000F, MCP- Ns and MTS-7s for the photon and electron beams selected. The results are relative (in percentage) to the 6 MV x-ray beam for photons and 6 MeV for electrons. Measurements were obtained within a 2.2% statistical uncertainty in all cases.

All detectors showed no significant energy dependence for the filtered MV photon and electron beams selected (variations within 2.5%), which is in good agreement with other publications on MCP- and MT-based TLDs[121]. The energy dependence of the detectors was also kept within the tolerance (2.5%) for the non-filtered photon beams. This is the first study to show the behavior of TLDs for such beams; therefore, no references are currently available on the characterization of such detectors for FFF beams.

The detectors response in terms of light output as a function of the absorbed dose is displayed in figure 3.9 for 6 and 15 MV photon beams. Standard deviations of the measurements were below 3% (1 SD) in all cases and below 2% in more than 80% of the measuring points. A linear function using the proportional-weighted least squares approach was fitted to the measured data.

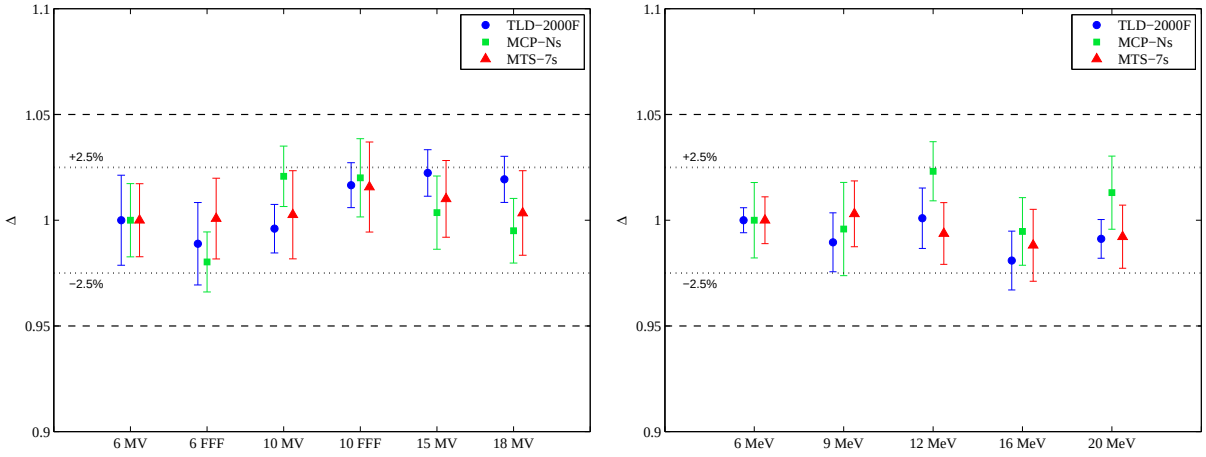

(a) photon (b) electron

Figure 3.8: Energy dependence of TLD-2000F, MCP-Ns and MTS-7s for the photon and electron beams selected.

TLD-2000F and MCP-Ns exhibited a linear response to the absorbed dose within the range [0.2-20] Gy, which widely covers the typical doses involved in radiotherapy treatments. Ginjaume *et al.*[121] found that standard-thickness ^{7}LiF:Mg,Cu,P (TLD-700H) detectors exhibited a linear response (within 3%), up to a dose of 9 Gy. For higher doses a slight sub-linearity was observed. Sub-linear dose response can be described simply as exponential saturation of the available trapping centers in the TL material and therefore, it depends on the concentration of dopants. On the other hand, the higher the TL mass, the higher the light output (signal) captured by the photomultiplier of the TLD reader—for equivalent dose exposure. For standard-thickness TLDs and high dose exposures (above 10 Gy), the sub-linear response observed might be more likely a consequence of the light output saturation of the reader rather than derived from the physical properties of the TL material. Hence, the difference in mass between TLD-2000F and TLD-700H (20 μm *vs.* 0.7 mm might be the cause of such disagreement of results.

On the contrary, MTS-7s showed a two-step supra-linear behavior, one at around 2-2.5 Gy and one at around 8-9 Gy, both for 6 and 15 MV photon beams. Supra-linearity of MT-based TLDs had been previously shown[112;121]. The most widely accepted model of supra-linearity in MT TLDs is based on "competition during heating", *i.e.* on the presence of non-TL-producing competing traps and on the presence of a spatial correlation between some fraction of electron traps and recombination centers[136;137]. The dose prescribed to the tumor is typically delivered in 2 Gy per fraction in conventional treatments. Therefore, the supra-linearity of MTS-7s might not be a constraint on its use for treatment plan verification since detectors might be kept within their linear response region. For hypofractionated treatments involving higher doses per fraction, the varia-

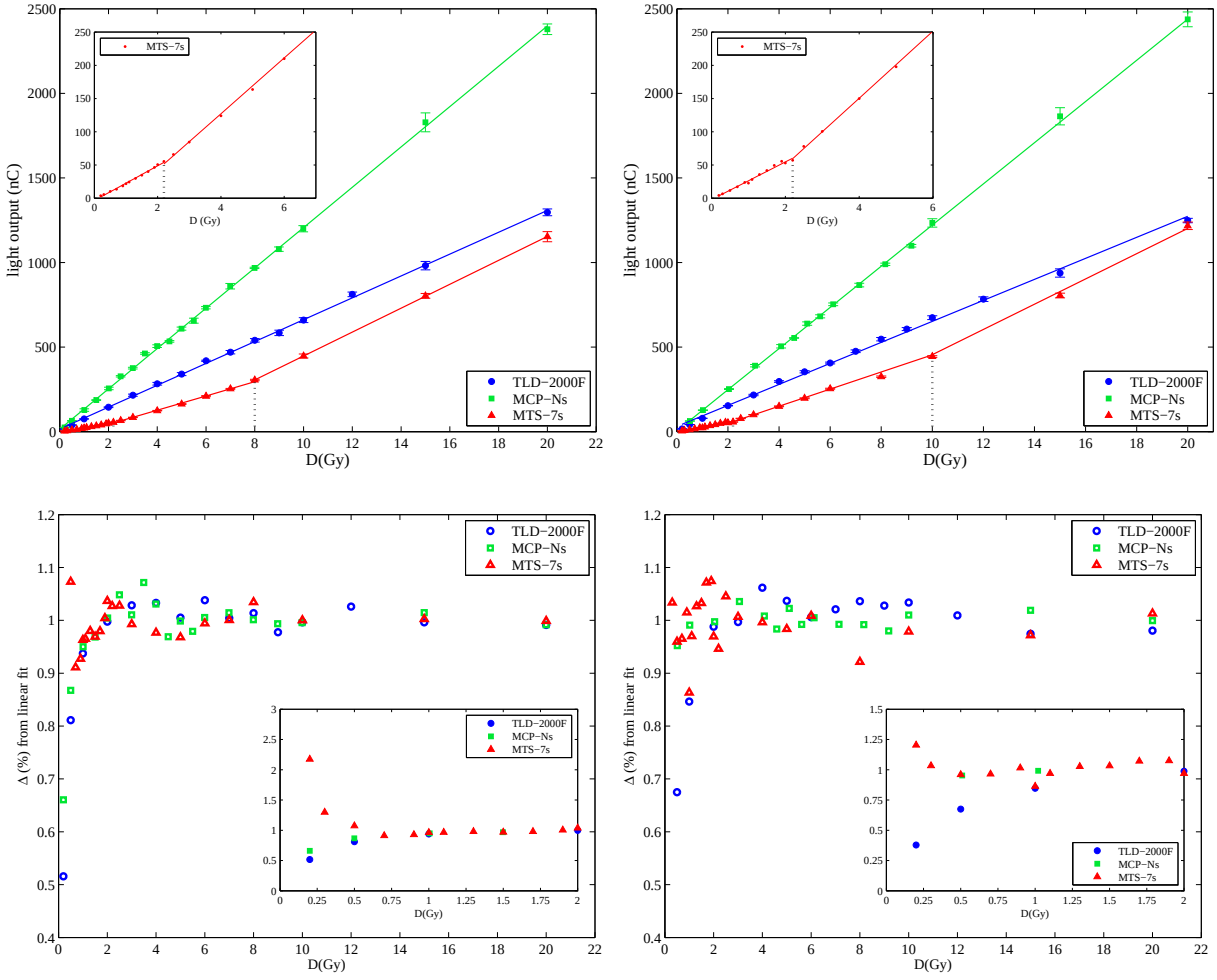

(c) 6 MV (d) 15 MV

Figure 3.9: Detectors response to dose for 6 and 15 MV photon beams and percentage difference of experimental measurements and linear fit.

tion of the dose response at 8 Gy approximately should be born in mind. TLD-2000F, MCP-Ns and MTS-7s are suitable for absorbed dose measurements in radiotherapy, although the use of MTS-7s deserves a word of caution according to their supra-linear behavior; MTS-7s must be calibrated within the appropriate linearity range.

TLD-2000F and MCP-Ns offered a higher sensitivity than MTS-7s, which is in good agreement with other publications[112;117]. Due to the absence of Ti, the increased concentration of Mg is transformed into an increased number of trapping centers, resulting in a further growth of TL signal being observed. MTS is a good example of the occurrence of only the first of these effects: an unknown reason allows competitors to be avoided, but the presence of Ti hampers the growth of the number of trapping centers. Nevertheless, this is not a limitation for the use of MT-based dosimeters in

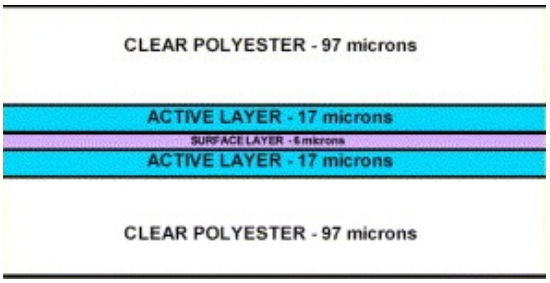

Figure 3.10: Structure of EBT Gafchromic® films used in this study.

Layer	ρ (g/cm^3)	Composition (weight %)					
		C	H	O	N	Li	Cl
Active	1.10	57.4	9.4	16.4	13.2	0.8	2.9
Surface	1.20	32.3	6.5	20.5	21.6	2.3	16.8
Clear polyester	1.35	65.2	4.2	33.3	-	-	-

Table 3.2: Density (ρ) and atomic composition (fraction by weight (%)) of the EBT components.

radiotherapy since the typical dose values are high enough to generate significant light outputs.

3.2.2 Radiochromic films

EBT and EBT2 Gafchromic® films (International Specialty Products, Wayne, NJ) were considered in this study. EBT consist of two active layers, sandwiched between polyester[138]. The film responds to radiation exposure by forming a blue colored polymer with an absorption peak at 636 nm. It can be used with doses from 10 cGy to 10 Gy. The film is composed principally of elements with atomic number less than 10, but contains a small amount of chlorine making the effective atomic number similar to that of water (Z_{eff}^{EBT}=6.98; Z_{eff}^{water}=7.3). The structure of the film model is described in figure 3.10. It is made by laminating two film coatings with an active layer approximately 17 μm thick and a surface layer approximately 3 μm thick. The coatings are applied to clear, transparent 97μm polyester. The overall atomic composition of EBT Gafchromic® film is H (39.7%), C (42.3%), O (16.2%), N(1.1%), Li (0.3%) and Cl (0.3%)—as quoted by the manufacturer. The composition of each layer is listed in table 3.2.

In 2009, International Specialty Products stopped sales of EBT film and now offers a similar radiochromic film product under the name Gafchromic® EBT2. The active component of EBT2 is the same as EBT. The most obvious difference between EBT2 and its predecessor is the yellow color of the film. This arises from the presence of a dye incorporated in the active layer. The principal purpose of this dye, referred to as a marker dye, is to establish a reference against which the response of the film can be measured; resulting in a net response that is independent of small differences

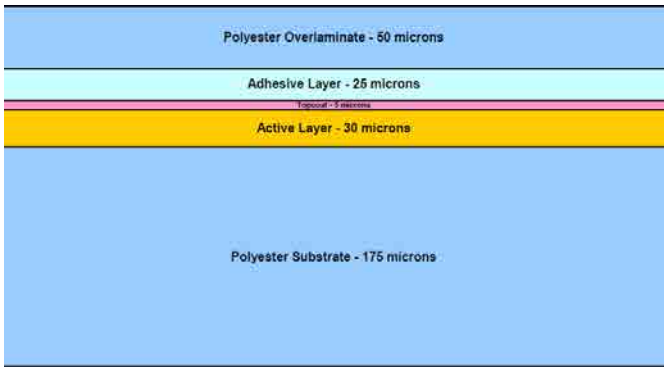

Figure 3.11: Structure of EBT2 Gafchromic® films used in this study.

Layer	ρ (g/cm^3)	Composition (weight %)							
		H	Li	C	N	O	Cl	K	Br
Polyester	1.35	4.20	-	62.5	-	33.3	-	-	-
Adhesive	1.20	9.55	0.90	57.8	0.23	27.8	1.73	0.64	1.30
Active	1.20	4.44	-	65.6	-	24.9	-	-	-

Table 3.3: Density (ρ) and atomic composition (fraction by weight (%)) of the EBT2 components.

in the thickness of the active layer. Similar to EBT, EBT2 has high atomic number components (chlorine, bromine, and potassium) that increase its Z_{eff}. EBT2 have Z_{eff}^{EBT2}=6.84. The structure of the film model is described in figure 3.11. The active layer is 30μm-thick and has a density of 1.20 g/cm^3. The atomic composition of each layer is listed in table 3.3 according to manufacturer specifications. It must be born in mind that the composition of these layers is a good faith estimate based on the proportion of the chemical constituents but it should not be used as a specification, as quoted by the manufacturer.

EBT films were scanned by means of an Epson Perfection 4990 Photo scanner (Seiko Epson Corporation, Nagano, Japan) and EBT2 by means of an Epson Expression 10000 XL Color Flatbed scanner (Seiko Epson Corporation, Nagano, Japan) 24 hours after irradiation on a film area guide. Films were scanned at 72 ppm resolution in transmission mode without any correction. Images were stored as TIFF files (RGB, 48 bits). Background and the three RGB scanning channels were taken into account for dose conversion by means of a 3-order polynomial calibration curve.

All the international recommendations for radiochromic film dosimetry were followed[43].

Films characterization was performed at the Hospital de la Santa Creu i de Sant Pau (HSCSP) in Barcelona and at the Hospital Duran i Reynals—Institut Català d'Oncologia Barcelona (ICOB). EBT[139;140] and EBT2[141;142] characterization have been previously reported. Energy dependence was found to be reasonably constant (±2%) within the range [Co60-RX 18 MV], which is in good agreement with other publica-

tions[143].

Chapter 4

On the suitability of ultra-thin detectors for the absorbed dose determination in the presence of high-density heterogeneities

Considering the issue brought up in section 1.4.3, in this section we investigated the potential suitability of several detectors for the absorbed dose measurements in the presence of high-density media. Ultra-thin thermoluminescent dosimeters (TLDs) and radiochromic films (EBT2) were considered. The choice of these detectors lies on their small size, which presumably brings a small electron fluence perturbation factor p (see section 1.4.3). Monte Carlo (MC) dose calculations were used to validate and explain the experimental results and to investigate the perturbation effects of the detectors.

4.1 Experimental setup

The detectors were utilized to measure percentage depth-dose (PDD) curves in a slab water phantom (Plastic Water^{TM} (PW), Computerized Imaging Reference Systems (CIRS), Norfolk (VA), electronic density relative to water ρ_e^w=1.03) with a bone-equivalent heterogeneity (cortical, CIRS, ρ_e^w=1.78). The phantom consisted of 30 × 30 cm^2 slabs with thicknesses ranging from 0.1 to 5 cm. The studied experimental configuration was 5 cm of PW followed by 5 cm of bone and 10 cm of PW (see figure 4.1).

PDD curves were measured for 6 and 18 MV x-ray beams from the Varian Clinac 2100 C/D linac described in section 3.1.1.2. The previously characterized MCP-Ns, MTS-7s and TLD-2000F TLDs as well as EBT2 Gafchromic® films (see section 3.2) were used to measure the PDDs. Up to 9 TLDs were used at each depth to reduce statistical uncertainty. 2-10 film pieces have been used at each depth and each piece

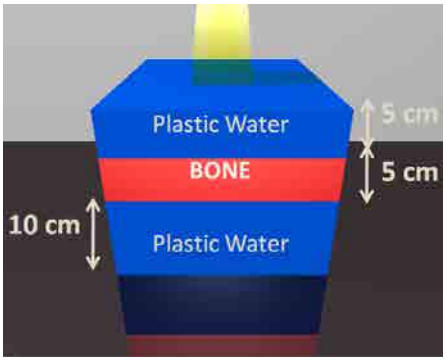

Figure 4.1: The experimental configuration.

has been read 3 times.

As a first approximation, perturbation factors (p) of the detectors (see section 1.4.3) were assumed to be negligible, *i.e.* the detector was assumed not to be perturbing the charged particle fluence (including its distribution in energy) existing in the medium in the absence of the cavity.

Detectors were calibrated to yield D_w regardless of the medium they are embedded in.

4.2 MC dose calculations

4.2.1 MC dose distributions

Monte Carlo (MC) simulations were used as the reference data for the evaluation of the TLDs and EBT2. Simulations were done with the PENELOPE code[144] and penEasy[145] was used as the main program. More details regarding the code were given in section 3.1.1.3.

Cutoff energies within the phantoms were fixed at 50 and 10 keV for electrons and photons, respectively. For the PDD curves, the spatial resolution in depth was set to 0.05 cm.

MC simulations give dose to medium (D_m). For comparison purposes, MC dose results were expressed in terms of D_w within the bone region by applying the corresponding Bragg-Gray stopping power ratio water-bone ($S_{w,b}$)[33] as described in Fernández-Varea *et al.*[37].

4.2.2 MC simulation of the detectors (cavities)

Aiming to understand the experimental results and the physics behind them, the detectors were simulated with MC. MTS-7s and MCP-Ns were simulated as cylindrical cavities of 4.5 mm with a sensitive LiF layer of 50 μm plus a 0.87 mm LiF substrate. TLD-2000F were simulated as cylindrical cavities of 20 μm. The polyimide tape on

	6 MV		18 MV	
$S_{\text{det,med}}$	This work	Others	This work	Others
$S_{\text{w,air}}$	1.114	1.115[37]	1.088	1.087[37]
$S_{\text{w,bone}}$	1.138	1.138[37]	1.131	1.131[37]
$S_{\text{w,LiF}}$	1.247	1.244[47]	1.248	1.246[47]
$S_{\text{w,EBT2}}$	1.008	-	1.007	-
$S_{\text{bone,LiF}}$	1.042	-	1.043	-
$S_{\text{bone,EBT2}}$	0.890	-	0.890	-

Table 4.1: Stopping-power ratios calculated at a depth of 10 cm for the 6 and 18 MV beams.

which the powder is fixed (see section 3.2.1) was dismissed as a first approximation due to its reduced thickness (approximately $< 25\,\mu$m). EBT2 were simulated according to manufacturers' specifications as displayed in figure 3.11 and the absorbed dose was scored in the active layer.

To further investigate the origin of potential perturbation effects of detectors, two more cavities were studied: (i) a $50\,\mu$m-thick LiF cavity, to evaluate the effect of the inert substrate of MCP-Ns and MTS-7s, and (ii) a $20\,\mu$m-thick LiF sensitive volume plus a $25\,\mu$m-thick Kapton substrate as quoted by manufacturers of TLD-2000F.

In order to reduce computation times and improve the statistics of the results, the calculations were split into 8 separate—statistically independent—simulations that ran in parallel on 8 separate CPUs.

The dose was expressed in terms of D_{w} using the corresponding stopping power ratios which were obtained using the methodology described by Fernández-Varea *et al.*[37]. The corresponding stopping power ratios were calculated: $S_{\text{w,LiF}}$ and $S_{\text{w,EBT2}}$, which were used to convert the dose inside the water (w) region; and $S_{\text{bone,LiF}}$ and $S_{\text{bone,EBT2}}$ together with $S_{\text{w,bone}}$, which were used to convert the dose inside the bone region. The values are shown in table 4.1 and compared (when possible) to other publications. $S_{\text{w,air}}$ was included for comparison purposes.

4.2.3 MC fluence calculation

Particle energy fluences inside the detectors (cavities) were computed and compared to the fluence in the medium (bone) in the absence of the detector in order to evaluate the potential correction factor p[33]. The comparison was made for the detectors placed at 7 cm in depth of the studied phantom (*i.e.* inside the bone region).

As for the simulation of the detectors, calculations were split into 8 separate—statistically independent—simulations that ran in parallel on 8 separate CPUs.

4.2.4 Simulation parameters and variance reduction techniques

Several variance reduction techniques were used to speed up the calculations.

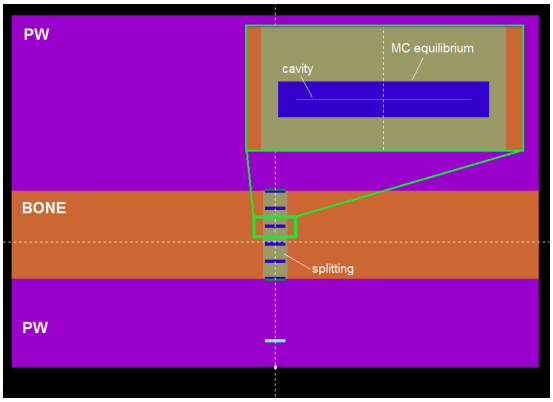

(a) MC cavities (PDD)

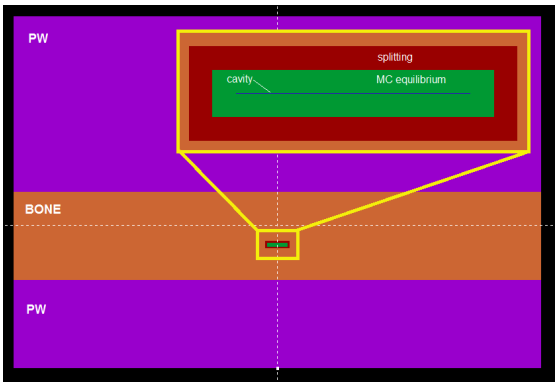

(b) MC energy fluence

Figure 4.2: MC geometry construction for the dose (a) and fluence (b) computations inside the cavities for TLD-2000F.

Absorption energy for electrons and photons ($E_{\text{abs}}^{e^-,\text{ph}}$)—defined in section 3.1.1.1—was set to 1.5 keV inside the cavities. A preliminary study of electron ranges with energy found this value appropriate to avoid bias in the MC calculation. As for the rest of simulation parameters we set: $\texttt{C}_1 = \texttt{C}_2 = 0.02$, $\texttt{W}_{\texttt{CC}} = 0.1\,\text{keV}$ and $\texttt{W}_{\texttt{CR}} = E_{\text{abs}}$.

Outside the cavities the simulation criteria were more generous. The absorption energies were set as $E_{\text{abs}}^{e^-} = 100\,\text{keV}$ and $E_{\text{abs}}^{\text{ph}} = 7.5\,\text{keV}$. The other parameters were set as follows: $\texttt{C}_1 = \texttt{C}_2 = 0.1$, $\texttt{W}_{\texttt{CC}} = 1\,\text{keV}$ and $\texttt{W}_{\texttt{CR}} = E_{\text{abs}}^{\text{ph}}$.

In order to avoid dose computation discontinuities, cavities were embedded in a region where the simulation parameters values were identical to those inside the cavities. Further, an outer volume was used to apply splitting and therefore, score more energy depositions inside the region of interest. Figure 4.2 shows the geometry for the MC scoring of the dose and fluence inside the detectors.

4.3 Results

4.3.1 PDD curves on the heterogeneous phantom

Measured PDD curves and the discrepancies with respect to MC are displayed in figure 4.3. Relative dose measurements were obtained within 2% statistical uncertainty.

Inside the bone region, MTS-7s, MCP-Ns provided comparable results for both beam energies and different field sizes. For this reason, only MTS-7s measurements are included in the 18 MV plots (figure 4.3 (d)-4.3(f)). Both detectors tended to underestimate the absorbed dose in bone by 4-5%. EBT2 exhibited comparable accuracy to MTS-7s and MCP-Ns. On the contrary, TLD-2000F were able to determine the dose inside the bone-equivalent heterogeneity with reasonable accuracy—differences with respect to MC were within 2% in most cases. This behavior was observed regardless of the beam energy and field size.

4.3.2 Cavities simulation

The results from the MC simulations of the different detectors (cavities) are shown in figure 4.4 for the 6 and 18 MV photon beams. The MC statistical uncertainties were below 1% in all cases. Error bars both for the MC results and the experimental measurements have been omitted in this graph for clarity.

We found excellent agreement (within statistical uncertainties) between the MC simulations and the experimental results for both beam energies and field sizes. The TLD-2000F measurements were in good agreement with the MC simulations of a 20 μm LiF cavity. The MC dose computations of a 50 μm-thick LiF volume plus a 0.83 mm-thick substrate matched the experimental measurements with MCP-Ns and MTS-7s. Finally, the MC dose scoring on EBT2 was consistent with the corresponding experimental data.

As for the MC investigation of the presence/absence of substrates we found that the simulation of the cavity of 50 μm (representing the MCP-Ns and MTS-7s without the substrate) was in good agreement with that of 20 μm (TLD-2000F) within statistical uncertainties, exhibiting a tendency to underestimate the absorbed dose in bone an extra 1%. The results regarding the cavity of 20 μm-thick LiF sensitive volume plus a 25 μm-thick Kapton substrate were comparable to those of the simulation of the cavity of 50 μm (MCP-Ns and MTS-7s without the substrate) and therefore were omitted from the figures for clarity.

4.3.3 Evaluation of electron energy fluence perturbation

Photon, electron and positron fluence distributions in energy in the different cavities were computed and compared to those in bone in the absence of the cavities. Results are shown in figure 4.5 for 6 and 18 MV.

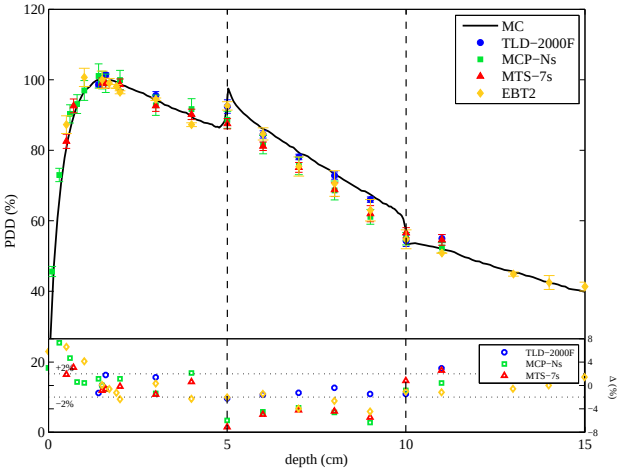

(a) 6 MV - $5 \times 5\,\mathrm{cm}^2$

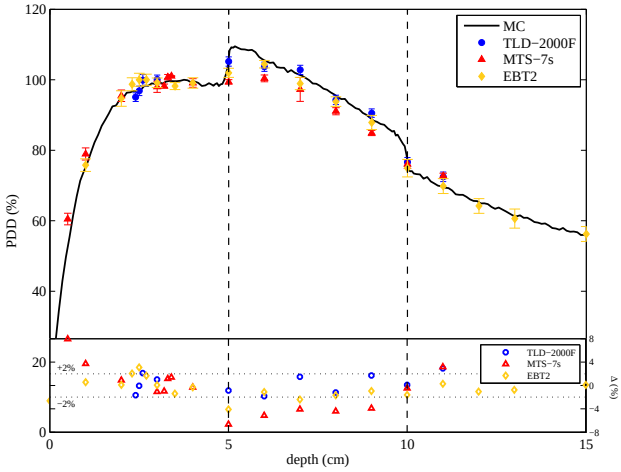

(b) 18 MV - $5 \times 5\,\mathrm{cm}^2$

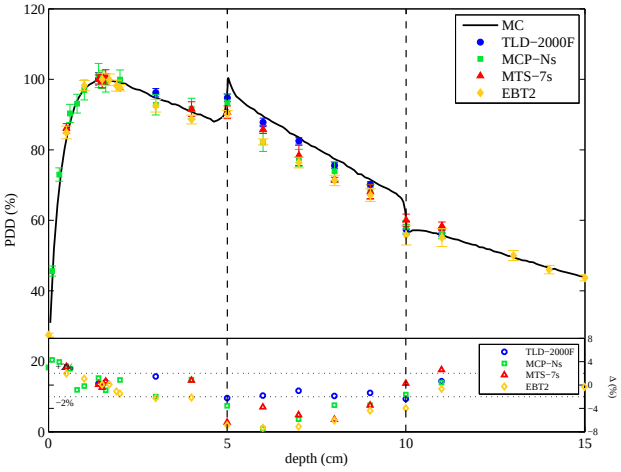

(c) 6 MV - $10 \times 10\,\mathrm{cm}^2$

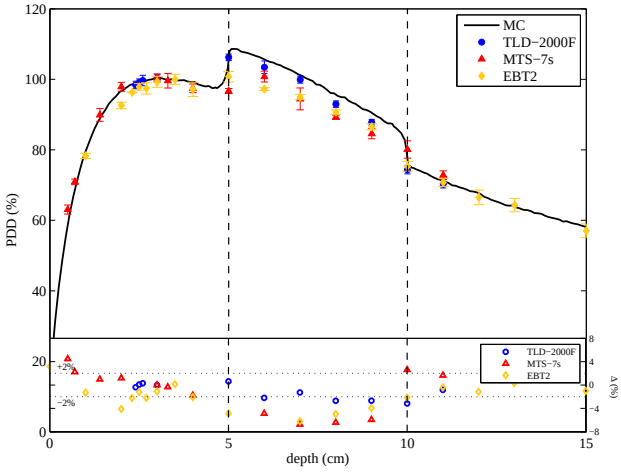

(d) 18 MV - $10 \times 10\,\mathrm{cm}^2$

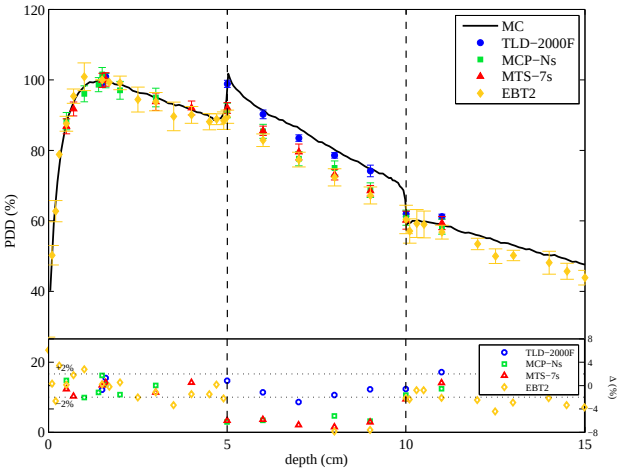

(e) 6 MV - $20 \times 20\,\mathrm{cm}^2$

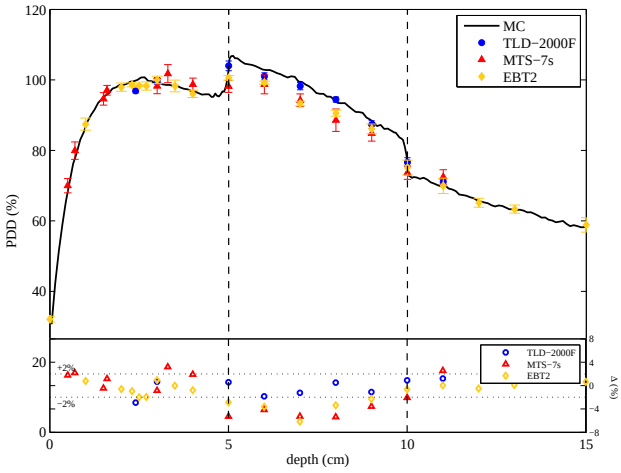

(f) 18 MV - $20 \times 20\,\mathrm{cm}^2$

Figure 4.3: PDD curves on the slab phantom with the bone-equivalent heterogeneity.

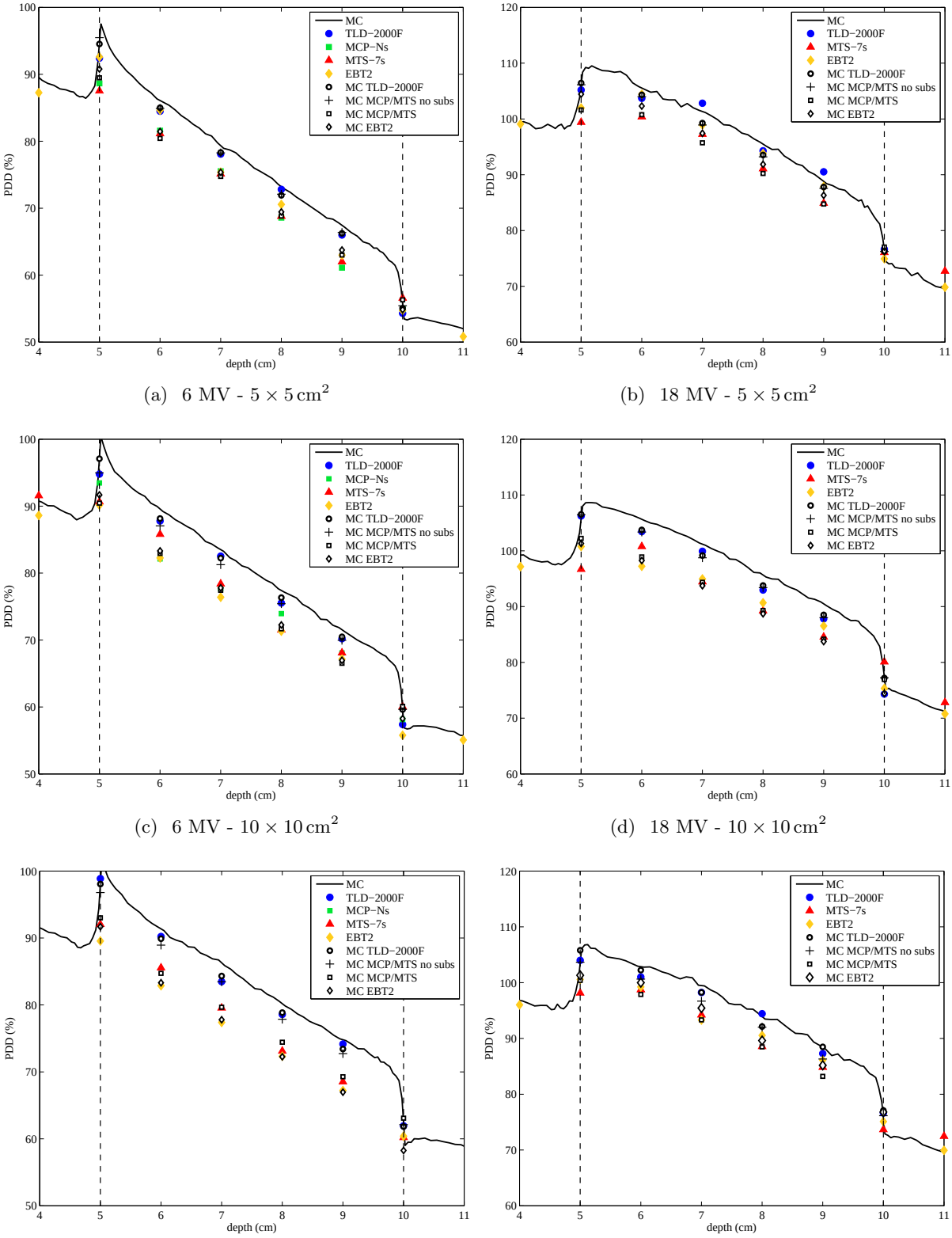

(a) 6 MV - $5 \times 5\,\mathrm{cm}^2$ (b) 18 MV - $5 \times 5\,\mathrm{cm}^2$

(c) 6 MV - $10 \times 10\,\mathrm{cm}^2$ (d) 18 MV - $10 \times 10\,\mathrm{cm}^2$

(e) 6 MV - $20 \times 20\,\mathrm{cm}^2$ (f) 18 MV - $20 \times 20\,\mathrm{cm}^2$

Figure 4.4: MC simulations of the detectors and experimental measurements.

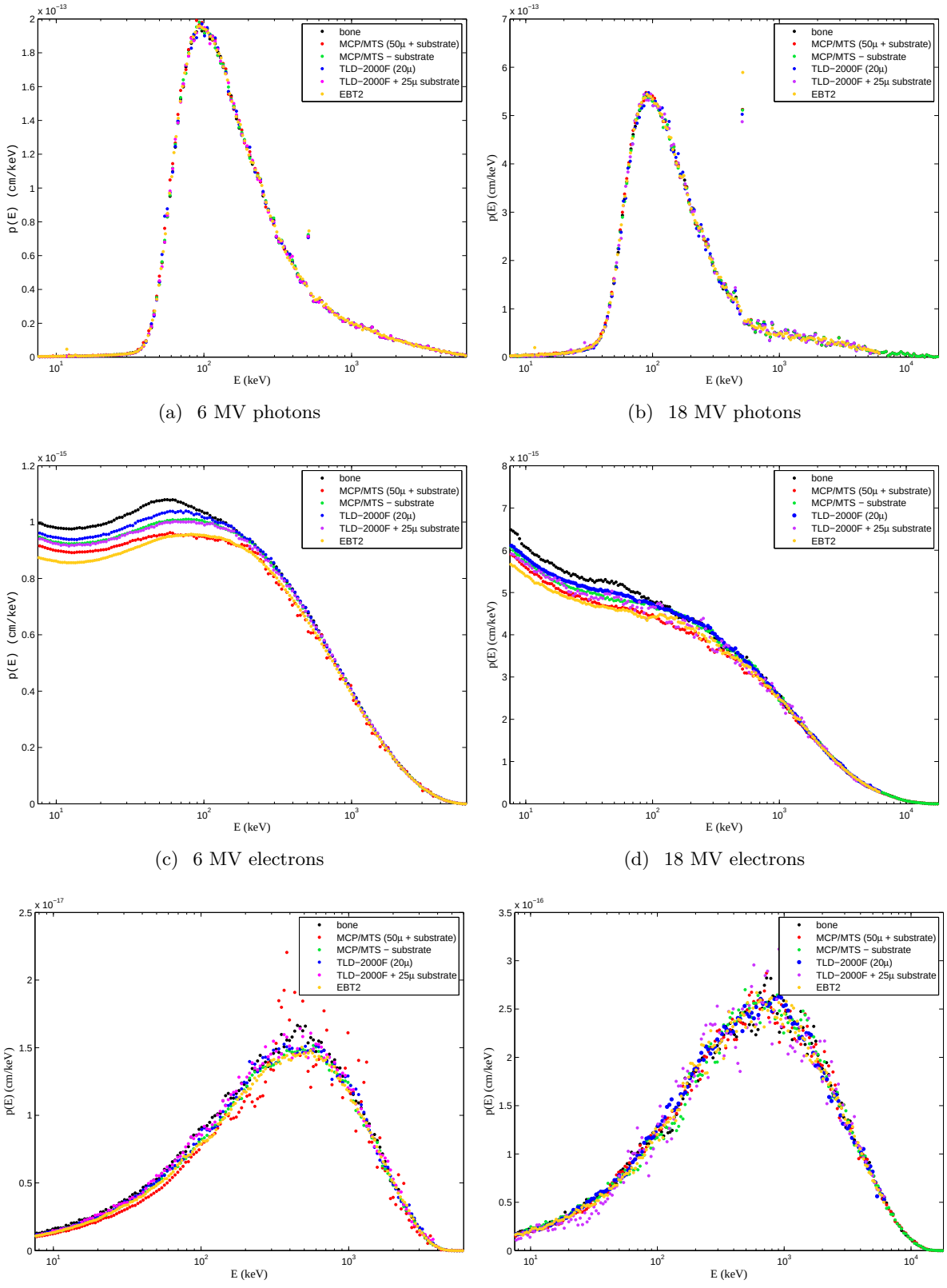

(a) 6 MV photons

(b) 18 MV photons

(c) 6 MV electrons

(d) 18 MV electrons

(e) 6 MV positrons

(f) 18 MV positrons

Figure 4.5: Particle fluence distributions in energy in the different detectors simulated compared to the particle fluences in bone in the absence of the detectors.

Photon fluences were identical in all cases whereas some perturbations of the electron and positron fluences were observed for the different cavities. As for the simulation of the detectors, the results are consistent with the experimental measurements: TLD-2000F had the lowest electron fluence perturbation effect among the detectors evaluated in this study—small yet not negligible. MCP-Ns, MTS-7s and EBT2 brought comparable fluence perturbation effects and therefore offered similar accuracy in the dose assessment in bone, although EBT2 have the smallest active volume among the detectors studied.

As for the investigation of the effect of the presence/absence of substrates, two main statements can be made. Firstly, a slight decrease in the electron fluence (increase of perturbation effect) can be noticed for the cavity of 50 μm (representing the MCP-Ns and MTS-7s without the substrate) compared to that of 20 μm (TLD-2000F). Nevertheless, this slight though perceptible change in fluence becomes only a 1% underestimation when comparing in terms of absorbed dose, according to the findings in the previous section 4.3.3. This indicates that the presence of the $\approx$ 0.8 mm-thick substrate added behind the 50 μm-thick active layer of MCP-Ns and MTS-7s decreases the number of backscattered electrons generated in bone reaching the sensitive volume, hence reducing the electron energy fluence in the cavity. Otherwise a LiF 50 μm-thick cavity might be small enough to ensure dose determination within 2% accuracy. Secondly, the results for cavity of 20 μm (TLD-2000F) plus a 25 μm-thick polyimide (kapton) substrate were comparable to those for the cavity of 50 μm (MCP-Ns and MTS-7s without the substrate). This reveals that the presence of a polyimide substrate behind the sensitive volume of TLD-2000F leads to an observable decrease of the electron energy fluence which turns into a 1% difference in terms of absorbed dose, as for a cavity 2.5 times larger (from 20 μm to 50 μm).

We have found that a LiF cavity of 50 μm might be small enough to ensure dose assessment in bone within 2% accuracy. To further develop the discussion of results, we evaluated the influence of the material of the cavity on the results. To this aim, we computed the fluences in a 50 μm-thick cavity made of (i) water and (ii) EBT active layer material (film), and compared them to that made of LiF. Energy fluences are depicted in figure 4.6. No significant differences were found among the different materials. Hence, the material composition of the sensitive volume (LiF, water or EBT's active layer film) does not alter the particle fluence (neither its distribution in energy) perturbation in bone.

4.4 Conclusions

The suitability of several detectors to accurately determine the absorbed dose in bone was evaluated. Ultra-thin TLDs and Gafchromic EBT2 radiochromic films were considered assuming that their reduced size might bring negligible/low perturbation effects

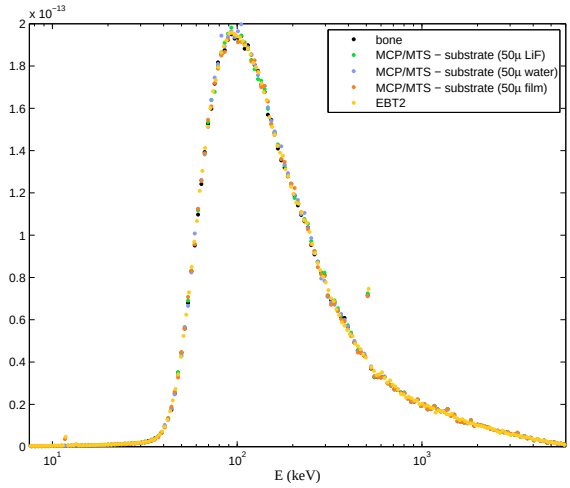

(a) 6 MV photons

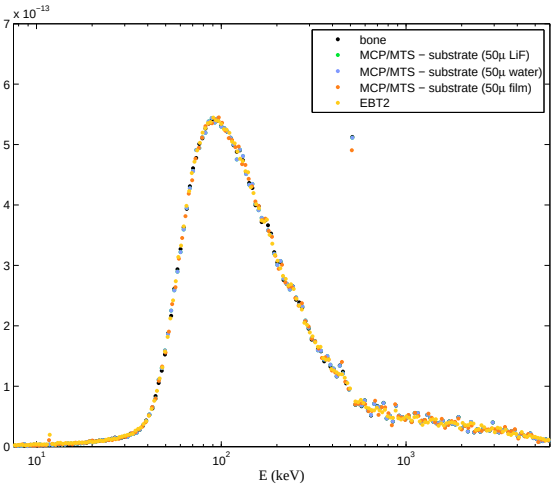

(b) 18 MV photons

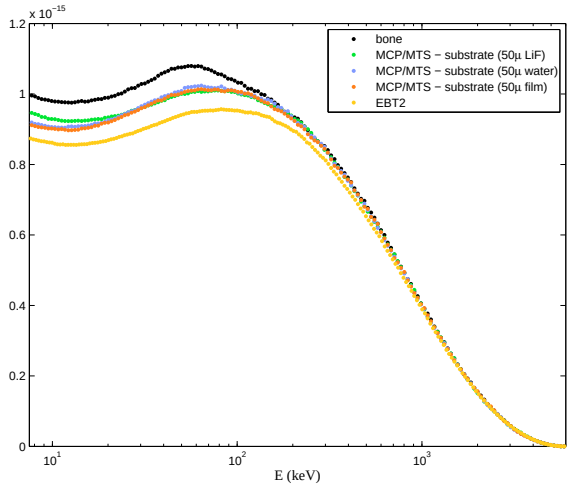

(c) 6 MV electrons

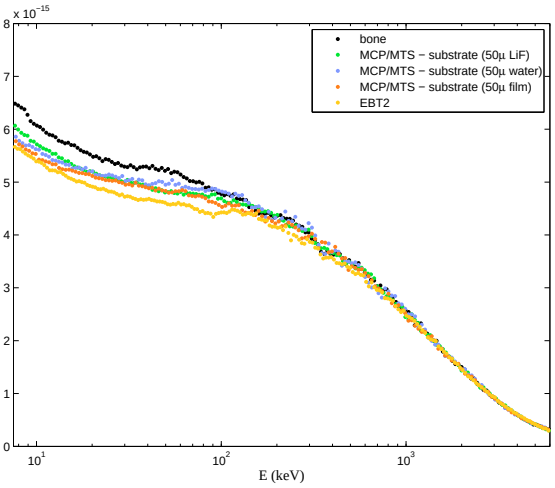

(d) 18 MV electrons

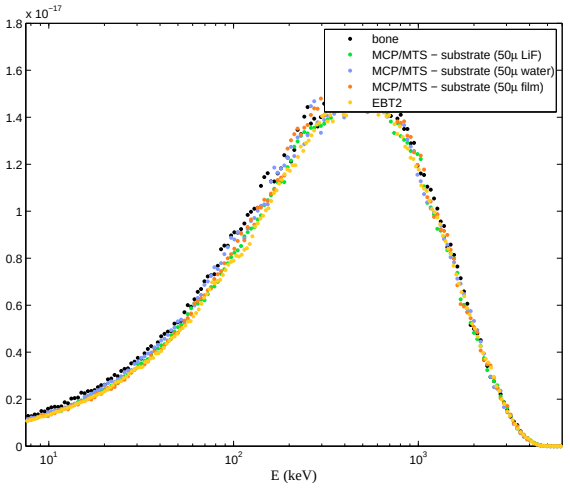

(e) 6 MV positrons

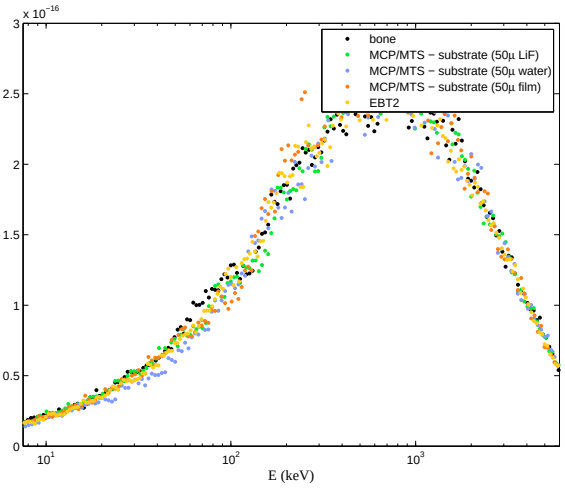

(f) 18 MV positrons

Figure 4.6: Particle fluence distributions in energy for a 50 μm cavity made of different materials compared to those in bone in the absence of the cavity and in EBT2.

in the medium.

Experimental measurements have been carried out in a water phantom with a bone-equivalent heterogeneity. MC simulations have been done to better understand the experimental results.

The results revealed that all detectors that were considered for this study bring a certain perturbation of the electron fluence and its distribution in energy inside bone. This perturbation leads to a systematic underestimation of the absorbed dose in bone, which arises from the difference between the effective atomic number of the detectors ($\approx$ 7 in all cases) and the bone-equivalent material ($\approx$ 11). TLD-2000F (cylindrical 20 μm-thick cavities) exhibited the lowest perturbation effects, providing reasonably accurate results in bone with only 2% underestimation of the dose. MCP-Ns and MTS-7s underestimated the dose within the bone region by 4-5%; despite the sensitive volume of the detectors might be small enough to avoid significant perturbation (cylindrical cavities with a thickness of 50 μm), the presence of the substrate added below the TL material is responsible for an extra 2-3% of dose underestimation due to a diminishing of backscattered electrons from bone reaching the active volume. Further, EBT2 provided comparable accuracy to MCP-Ns and MTS-7s in bone; the upper and lower polyester layers embedding the active material add a non-negligible perturbation of the fluence in bone in the absence of the detectors. Hence, TLD-2000F were found to be the detector of choice for absorbed dose measurements in bone yet a 2% dose underestimation should be born in mind.

The MC simulations show that a 50 μm-thick detector might be small enough to provide the dose assessment in bone within a 2% accuracy, regardless of the tested material composition—LiF, water or EBT's active layer film.

Chapter 5

On the dosimetric validation of Acuros XB in heterogeneities

In November 2010, Varian Medical Systems received clearance form the US Food and Drug Administration to market their new dose calculation algorithm, Acuros® XB (AXB). Based on the general-purpose radiation transport modeling system, Attila®, first developed at Los Alamos National Laboratory in Los Alamos, New Mexico, AXB has been modified and optimized for radiation therapy planning calculations.

The AXB advanced dose calculation algorithm has been developed to address two strategic needs of external photon beam treatment planning: accuracy and speed. This algorithm implemented in the Eclipse™ treatment planning system (TPS) uses a sophisticated technique to deterministically solve the linear Boltzmann transport equation (LBTE) (see equation 1.2 and 1.1 in chapter 1) using an iterative approach.

AXB directly accounts for the effects of heterogeneities in patient dose calculations. Hence, the algorithm can provide comparable accuracy to Monte Carlo simulations (MC). The impetus behind the development of explicit LBTE solution methods is to provide a rapid alternative to MC simulations, which are known to be time-consuming. With sufficient refinement, both MC and AXB are expected to converge to the same dose predictions[146]. The achievable accuracy of both methods is potentially equivalent and only constrained by the available computational resources. For practical reasons, a limited number of histories are possible for a MC simulation, and a limited finite sampling of the energy groups, beam angles and beam geometries is possible for AXB. Based on other publications, AXB achieved a comparable computation time with the clinically used Collapsed-Cone Convolution (CCC) algorithm[147;148].

The main features of the algorithm are described below. Further details on the algorithm can be found elsewhere[146].

This study was developed in collaboration with the Hospital Josep Trueta, Institut Català d'Oncologia Girona (ICOG), Girona, Spain.

5.1 AXB background

The Boltzman transport equation describes the macroscopic behavior of radiation as it travels through and interacts with matter. The LBTE assumes that particles only interact with the matter they are passing through and not with each other. This assumption is valid for conditions without external magnetic fields. In this case, the solution to the LBTE would give an "exact" description of the absorbed dose within a given volume. Since analytic solutions (closed forms solutions) to the LBTE can only be obtained for a few simplified problems, the LBTE must be solved in an open form or non-analytic manner.

There are two general approaches to obtaining open form solutions to the LBTE. The first approach is the widely known MC method, which do not explicitly solve the LBTE but obtains the solution indirectly. The second approach is to explicitly solve it using "convergent" numerical methods, like AXB does. In the explicit LBTE solution methods, errors are primarily systematic and result from discretization of the variables in space, angle, and energy. Larger steps in the discretization process result in a faster solution, but less accuracy.

5.1.1 Source model in AXB

AXB source model consists of four components[149]:

- Primary source: it is a user-defined circular or elliptical source located at the target plane which models the bremsstrahlung photons created in the target that do not interact in the treatment head.
- Extra-focal source: it consists of a Gaussian plane source located at the bottom of the flattening filter, which models the photons that result from interactions in the accelerator head outside the target (primary in the flattening filter, primary collimators, and secondary jaws).
- Electron contamination: it represents the dose deposited in the build-up region, not accounted for by the primary and extra-focal source components.
- Photons scattered from wedge: it represents the scatter from hard wedges. It is implemented with a dual Gaussian model, where the width of the Gaussian kernel increases with distance from the wedge.

5.1.2 Dose calculation

The AXB patients' transport consists of four discrete steps, which are performed in the following order:

1. Transport of source model fluence into the patient.

2. Calculation of scattered photon fluence in the patient.

3. Calculation of scattered electron fluence in the patient.

4. Dose calculation.

In Step 1, the machine sources are modeled as external sources and ray tracing is performed to calculate the uncollided photon and electron fluence distributions in the patient. In Step 2 and 3, AXB discretizes in space, angle, and energy, and iteratively solves the LBTE. In Step 4, the dose in any voxel is obtained by applying an energy-dependent fluence-to-dose response function to the local energy-dependent electron fluence in that voxel. When dose-to-medium (D_{m}) is calculated, the energy-dependent response function is based on the material properties of that voxel. On the contrary, when dose-to-water (D_{w}) is calculated, the energy-dependent fluence-to-dose response function is based on water.

Unlike convolution/superposition algorithms, where heterogeneities are generally handled as density-based corrections applied to dose kernels calculated in water, AXB explicitly models the physical interactions of radiation with matter. To do this, AXB requires the chemical composition of each material in which particles are transported through, not only the density. Eclipse$^{\mathrm{TM}}$ provides AXB with a mass density and material type in each voxel of the image grid—computed tomography (CT). Its material library includes five biological materials (lung, adipose tissue, muscle, cartilage, and bone) and 16 non-biologic materials. The material composition is specified in tables 5.1 and 5.2.

5.1.3 Material specification

Material determination is done in two ways for AXB. The default method used to determine the material composition of a given voxel in a 3D image is based on the Hounsfield Unit (HU) value. The HU value in the voxel in converted to mass density using the CT calibration curve. The curve can be configured by the users for their specific CT scanner. Once mass density is known in a voxel, the material is determined based on a hard coded look-up table stored in the Varian system database. This automatic conversion is used for all voxels with mass density below $3\,\mathrm{g/cm^3}$. Any voxel with density higher than $3\,\mathrm{g/cm^3}$ requires user assignment. Furthermore, the automatic material assignment only assigns biological materials to voxels. Based on their mass density, voxels will be assigned lung, adipose tissue, muscle, cartilage, or bone.

Any noise present in the CT image is transformed directly into a noise in the mass-density map of the image. In the regions of the CT image where the mass density is very close to a minimum/maximum value of two materials. The discrete nature of the material assignment and the noise in the CT image may lead to a rapid alternation between two different material assignments. Depending on the strength of the noise

Material	Z_{eff}	Element	Weight Fraction
Lung (ICRP 1974)	8.14	H	0.101278
		C	0.102310
		N	0.028650
		O	0.757072
		Na	0.001840
		Mg	0.000730
		P	0.000800
		S	0.002250
		Cl	0.002660
		K	0.001940
		Ca	0.000090
		Fe	0.000370
		Zn	0.000010
Adipose tissue (ICRP 1975)	5.91	H	0.119477
		C	0.637240
		N	0.007970
		O	0.232333
		Na	0.000500
		Mg	0.000020
		P	0.000160
		S	0.000730
		Cl	0.001190
		K	0.000320
		Ca	0.000020
		Fe	0.000020
		Zn	0.000020
Muscle, Skeletal (ICRP 1975)	7.13	H	0.100637
		C	0.107830
		N	0.027680
		O	0.754773
		Na	0.000750
		Mg	0.000190
		P	0.001800
		S	0.002410
		Cl	0.000790
		K	0.003020
		Ca	0.000030
		Fe	0.000040
		Zn	0.000050

Table 5.1: Material composition in AXB (v.10.0.28). From Failla *et al.*[146].

Material	Z_{eff}	Element	Weight Fraction
Cartilage (ICRP 1975)	7.38	H	0.096
		C	0.099
		N	0.022
		O	0.744
		Na	0.005
		Mg	NA
		P	0.022
		S	0.009
		Cl	0.003
		K	NA
		Ca	NA
Bone (ICRP 1975)	8.14	H	0.047234
		C	0.14433
		N	0.04199
		O	0.446096
		Mg	0.0022
		P	0.10497
		S	0.00315
		Ca	0.20993
		Zn	0.0001
Aluminum	13	Al	1

Table 5.2: Material composition in AXB (v.10.0.28). From Failla *et al.*[146].

and on the calculation grid size this effect may be seen in these regions as a slight noise in the dose distribution[146].

The list of supported materials with associated density ranges is provided in table 5.3.

Material	Density (g/cm^3)		
	Low	Nominal	High
Lung (ICRP 1975)	0.000	0.260	0.590
Adipose tissue (ICRP 1975)	0.590	0.920	0.985
Muscle, skeletal (ICRP 1975)	0.985	1.050	1.075
Cartilage (ICRP 1975)	1.075	1.100	1.475
Bone (ICRP 1975)	1.475	1.850	3.000

Table 5.3: Material mass densities in AXB (v.10.0.28) (automatic CT-to-material conversion). From Failla *et al.*[146].

5.1.4 D_w and D_m in AXB

Both AXB and MC methods calculate D_m based on energy deposition. However, when calculating D_w in non-water materials, AXB and MC methods employ different approaches.

MC methods will generally calculate D_{m} and employ stopping power ratios to convert D_{m} into D_{w}, as it has been previously mentioned in this manuscript.

On the contrary, AXB calculates the energy-dependent electron fluence using the material composition of the patient, regardless of whether D_{w} or D_{m} is selected, as stated above. When D_{w} is selected, in non-water materials this is analogous to calculation the dose received by a volume of water which is small enough to not significantly perturb the energy-dependent electron fluence. Due to the very short range of low-energy electrons, this volume may be much smaller than either the dose grid voxel size or detectors used to experimentally measure D_{w}. This effect is most significant for bone and non-biologic, high-density materials such as aluminum, titanium and steel.

Hence, whereas MC methods use collisional stopping power ratios to determine the ratio $D_{\mathrm{w}}/D_{\mathrm{m}}$, it is reflected in the energy-deposition ratios in AXB.

5.1.5 On the AXB validation

Vassiliev *et al.*[21] validated in 2010 a pre-clinical version of the algorithm against Monte Carlo (MC) (EGSnrc)[150] in an extensive variety of materials and reported excellent agreement between both dose calculation methods. They used an heterogeneous slab phantom whose configuration was: water-bone-lung-water. Depth-dose distributions were evaluated for different field sizes. Maximum relative differences between AXB and MC were encountered in the lung region. These were found to be less than 1.5% and 2.3% (local dose differences) for 6 and 18 MV, respectively. Encouraging results were also found for an anthropomorphic phantom.

Since then, several studies have been published on the evaluation of the released AXB in water and heterogeneous phantoms. Most of these studies also included superposition/convolution algorithms as the current standard, such as AAA or the CCC method. AXB has been compared in simple geometries using virtual phantoms for single photon beams either against MC simulations[147;151–153] or against experimental measurements[154]. In general, the dose accuracy yielded by AXB has been reported to be comparable to that of MC simulations and AXB has been presented as a significant improvement over the current algorithms in the presence of high-density and low-density media. Few studies have validated the algorithm experimentally for more complex treatments, such as IMRT or VMAT[148;155–158].

Han *et al.*[148;156] used films and TLD measurements to verify IMRT and VMAT plans mainly in water-equivalent regions and Kan, Leung, and Yu[157] validated experimentally the dose at/near the heterogeneity interfaces. Hence, the effects from heterogeneities could not be fully investigated. Only Kan *et al.*[158] reported, in a recent publication, film measurements within the heterogeneous medium of the nasopharygeal region of an anthropomorphic phantom. Thus, experimental measurements inside the heterogeneities have not been reported yet. The validation of a treatment planning system requires the comparison against both experimental measurements and MC results.

Both MC and AXB dose calculations might be affected by similar sources of uncertainty, such as those arising from the radiation source modeling or from the materials definition (atomic composition, mean excitation energy). In this sense, experimental measurements might be essential to procure real dose estimations provided a proper detector is available.

These studies also investigated both dose-reporting methods available in AXB, *i.e.* D_w and D_m, but did not include the MC for a fair comparison in terms of D_m—detectors are calibrated to yield D_w and they are placed in water-equivalent regions. Apart from these, only the work of Han *et al.*[147] compared D_w and D_m in AXB against MC, but quantitative comparisons where reported only in terms of D_m and the study did not include measurements. For the mentioned reasons, there is still room for further investigation of the behavior of AXB in heterogeneities.

In this study, we examined the accuracy of the AXB dose calculation algorithm in phantoms with lung-equivalent and bone-equivalent heterogeneities using both MC simulations and experimental measurements for different photon beam energies and field sizes. AAA was also included in the comparison. The two dose-reporting methods in AXB (D_w and D_m) were analyzed and the potential influence of the use of virtual phantoms or CT images on the dose calculations was also evaluated. All AXB and AAA dose calculations were performed by the radiophysicists at ICOG.

5.2 Experimental setup for the AXB verification

Two photon beam energies, 6 and 18 MV, from a Varian Clinac 2100 C/D (Varian, Palo Alto, CA) linear accelerator and four field sizes ranging from 2×2 to $20 \times 20\,\text{cm}^2$ were considered.

Percentage depth-dose (PDD) curves and dose profiles normalized to central axis were evaluated on a water-equivalent slab phantom (PTW RW3, electron density relative to water ρ_e^w=1.012) with (i) a lung-equivalent heterogeneity (Computerized Imaging Reference Systems (CIRS), Norfolk (VA), ρ_e^w=0.195) and (ii) a bone-equivalent heterogeneity (cortical bone CIRS, ρ_e^w=1.779). The phantom consisted of $30 \times 30\,\text{cm}^2$ slabs with thicknesses ranging from 0.1 to 5 cm. PDDs and lateral profiles were normalized to the maximum dose.

The studied experimental configurations were (i) 5 cm of RW3 followed by 13 cm of lung and then by 10 cm of RW3, and (ii) 5 cm of RW3 followed by 5 cm of bone and 10 cm of RW3 (see figure 5.1). Although the second configuration was unrealistic from a clinical perspective—therapy fields would rarely traverse such thickness of cortical bone—it provided a wider region to evaluate the behavior of the algorithm.

Dose profiles were evaluated (i) in the slab phantom with the lung-equivalent heterogeneity at a depth of 10 cm, and (ii) in the slab phantom with the bone-equivalent heterogeneity at a depth of 7 cm; both were compared against their corresponding dose

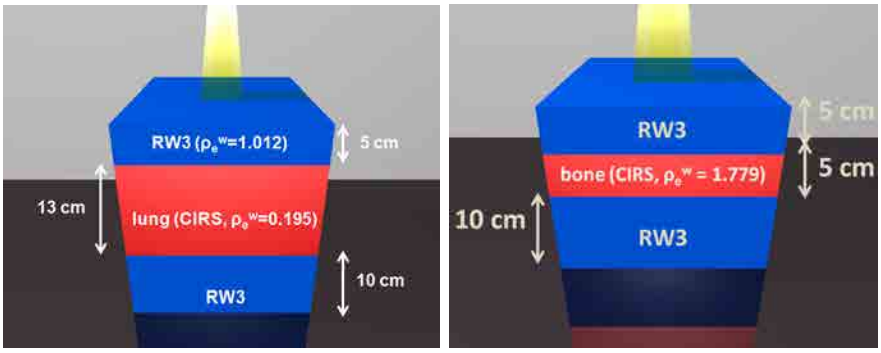

(a) (b)

Figure 5.1: The experimental configurations.

profiles in water to quantify the change in beam penumbrae.

Virtual phantoms were generated for AXB, AAA and MC calculations. The material in each region of the phantom (water, lung or bone) was selected from the materials available in ECLIPSE^{TM} (see tables 5.1-5.3) and the electron density was set equal to the nominal value specified by manufacturers by adjusting the CT number. One should bear in mind that, as stated above, the materials available in AXB are biological materials whereas the experimental setup consists of plastic materials—and therefore the elemental composition might differ. This may be a source of discrepancy in the dose comparisons to experimental measurements, and it must be taken into account when discussing the results. As a first step, we computed the dose distributions on the heterogeneous phantoms using the materials in AXB (ICRP) and the plastic materials (CIRS) available at our facility for the heterogeneous regions. The comparison is shown in figure 5.2 for one of the beam configurations both in terms of D_m and D_w for lung and bone. When comparing in terms of D_w, we found excellent agreement between both types of bone whereas differences of about 2% were observed in lung.

Dose distributions were also obtained using the CT images of the phantoms to evaluate the effects of artifacts arisen from the image acquisition and the material assignment procedure on the final dose computations. Identical HU-to-mass density and HU-to-material conversion curves (see figure 5.3) were used in AXB and MC to avoid a potential source of discrepancy on material assignment. This offers a fair comparison between both calculation methods. The experimental measurements are essential in this approach, allowing the evaluation of the potential effect of the automatic material assignment procedure on dose distributions. Images were generated on an Optima CT580RT CT scanner (General Electric Healthcare, Fairfield, CT). The field-of-view was set to 65 cm and the voxel size was fixed to $1.27 \times 1.27 \times 5\,\text{mm}^3$.

The three source model used in AXB (v.10.0.28) and AAA (v.10.0.28) was automatically configured using the default focal spot size of 1 mm in x and y directions[159].

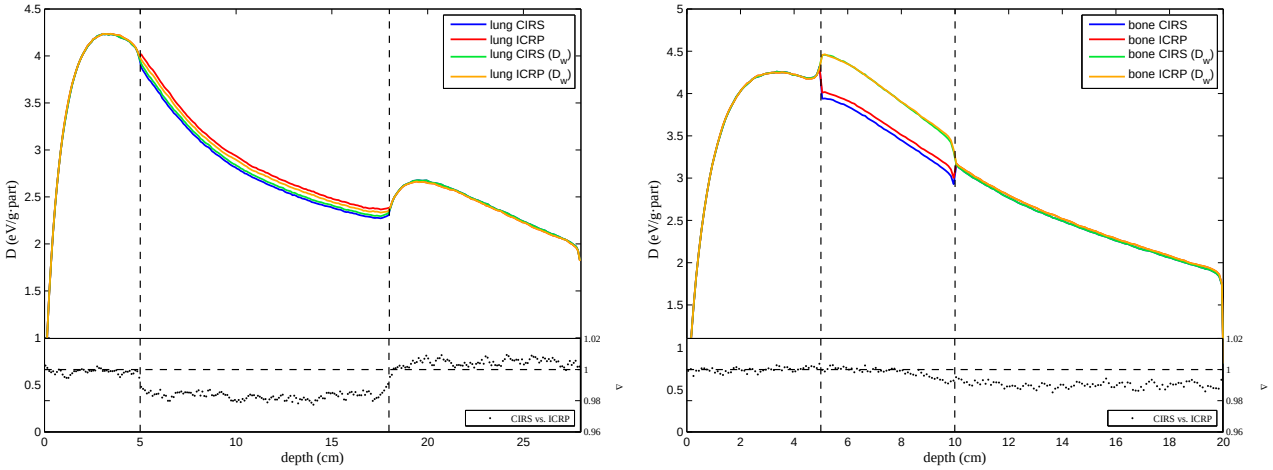

(a) (b)

Figure 5.2: MC dose distributions on the heterogeneous phantoms for 18 MV and a $5 \times 5\,\mathrm{cm}^2$ field comparing the biological materials (ICRP) against the plastic materials (CIRS) in terms of D_m and D_w.

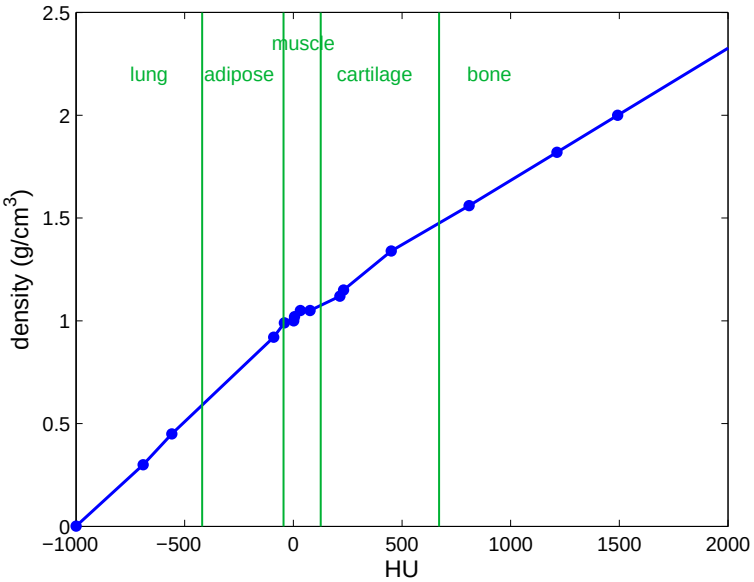

Figure 5.3: HU-to-density calibration curve integrated in the TPS. The density-to-material conversion is also specified.

The output calculation grid was set to $0.2 \times 0.2 \times 0.2\,\mathrm{mm}^3$.

Comparisons were made in terms of D_w since detectors were calibrated to yield D_w. A comparison between AXB and MC in terms of D_m was also performed for the phantom with the bone equivalent heterogeneity.

AXB, AAA and MC were initially validated in water for 6 and 18 MV photon beams against experimental measurements. Output factors, PDD and dose profiles for open and enhanced dynamic wedge (EDW) fields (ranging from 2×2 to $40 \times 40\,\mathrm{cm}^2$) were measured in water using PTW semiflex ionization chamber (IC) (Freiburg, Germany), PTW Roos IC, Scanditronix PFD-3G diode and PTW-LA48 linear array detectors, respectively.

5.2.1 Photon MC dose calculations

Simulations were done with the PENELOPE code[144] and penEasy[145] was used as the main program (see chapter 3 for more details).

As the authors have reported elsewhere[63], simulations were done in two steps, as stated in section 3.1.1.4 of this manuscript. Phase-space files stored about $3 \cdot 10^8$ particles to ensure the statistical uncertainty to be below 2% for dose distributions.

Cutoff energies within the phantoms were fixed at 50 and 10 keV for electrons and photons, respectively. For the PDD curves, the spatial resolution in depth was set to 0.1 cm, although it was reduced to 0.05 cm at the interfaces to accurately account for the steep dose gradient when switching from one medium to another, especially in bone. Dose profiles were obtained with a spatial resolution of 0.1 cm at a particular depth.

MC simulations give D_m. For comparison purposes, MC dose results were expressed in terms of D_w when required by applying the corresponding Bragg-Gray stopping power ratio water-medium ($S_\mathrm{w,med}$) as described in Fernández-Varea *et al.*[37].

5.2.2 Experimental measurements

All detectors were calibrated to yield D_w regardless of the media they were embedded in.

5.2.2.1 Ionization chambers

Two types of IC were used to measure PDD curves: $0.35\,\mathrm{cm}^3$ Roos (PTW, Freiburg, Germany) and $0.016\,\mathrm{cm}^3$ PinPoint 31016 (PTW, Freiburg, Germany). Both were connected to the UNIDOS electrometer (PTW, Freiburg, Germany). Due to their physical dimensions, the Roos IC was used for the largest fields ($10 \times 10\,\mathrm{cm}^2$ and $20 \times 20\,\mathrm{cm}^2$), whereas the PinPoint 31016 IC was preferred for the smallest fields measurements ($2 \times 2\,\mathrm{cm}^2$ and $5 \times 5\,\mathrm{cm}^2$). IC measurements were carried out by the radiophysicists at ICOG.

Dosimetry protocols provide a set of correction factors for converting ionization into dose, but only for water-equivalent materials and at a reference depth [40;41] (as detailed in section 1.4.3). The AAPM Report No. 85 [20] clearly states that ionization measurements from parallel ionization chambers cannot be used inside tissues other than water without applying a correction factor from the fluence perturbation caused by the presence of the chamber in the medium. Since such factors are unknown for our IC, only TLDs were used in lung and bone in this study. In particular, ultra-thin dosimeters (< 0.01 cm-thick) were chosen to avoid perturbation effects in bone.

5.2.2.2 Thermoluminescent dosimeters

Two types of TLD were used: ^{7}LiF:Mg,Ti (TLD-700, Thermo Fisher Scientific Inc., Erlangen, Germany) and LiF:Cu,Mg,P (TLD-2000F, Conqueror Electronics Technology Co. Ltd., Beijing, China). The main features of TLD-2000F are described in section 3.2.1.

The thermoluminescent materials chosen have an effective atomic number similar to soft tissue, which minimizes potential perturbation effects when measuring in soft tissue or water. However, especial care must be given in the case of bone. Whereas lung is quite similar to water or soft tissue in terms of effective atomic number, bone differs significantly. According to the finding presented in section 4.3, TLD-2000F were the detectors of choice inside the bone-equivalent region. For the dose measurements in lung we used TLD-700, which have been previously shown to be suitable for this kind of measurements [63].

Standard annealing and readout were carried out as described in section 3.2.1.

Several detectors (up to 9, depending on the field size) were used at each depth in order to reduce the statistical uncertainty of the results. Likewise, some measurements were repeated up to three times. This, together with the application of individual correction factors and a sensitivity stability control, allowed to achieve results with statistical uncertainties of $\pm$1-2% in all cases.

5.2.2.3 Films

Film dosimetry was preferred for measuring lateral profiles to avoid the influence of the finite detector size and to improve the spatial resolution. Gafchromic®EBT radiochromic films (International Specialty Products, Wayne, NJ) from a single batch together with an Epson Perfection 4990 Photo scanner (Seiko Epson Corporation, Nagano, Japan) were used. Film measurements were carried out by the radiophysicists at ICOG. Main detectors' features as well as readout procedures are described in section 3.2.2.

5.3 Results

5.3.1 AXB validations in water

AXB validation in water was carried out at ICOG. Output factors for open and EDW fields were within 1% and 1.3%, respectively, compared to experimental measurements. Small systematic differences might be attributable to the beam source modeling. The average deviations for PDD were 0.4% in dose, and distance-to-agreement (DTA) was below 2 mm for all cases, except for the build-up region of the 18 MV $40 \times 40\,\mathrm{cm}^2$ open field. For the profiles, deviations were within 1% for 6 MV and 2% for 18 MV in the inner field region (80% nominal field size). DTA was below 1 mm in the penumbra region—defined as the distance between the 80% and the 20% of the central axis dose—for all cases, including EDW fields. These results were in good agreement with the study of Fogliata *et al.*[151].

The validation of the MC PDD curves and lateral profiles for 6 and 18 MV photon beams in water were presented in chapter 3 in figures 3.1-3.4.

5.3.2 AXB validations in the heterogeneous phantoms

5.3.2.1 Central-axis doses

Figures 5.4-5.6 show the measured and calculated PDD curves for the selected photon energies and field sizes for the two heterogeneous phantoms. Differences relative to MC are also displayed in the figures. AXB *vs.* MC dose comparisons in terms of D_m are also included for the phantom with the bone-equivalent heterogeneity (figure 5.6).

MC results were yielded within 1% statistical uncertainty (2 standard deviations (SD)). IC and TLD measurements were obtained with statistical uncertainties below 1% and 2%, respectively. The agreement with MC was within 2% in 98% of the cases. Exceptionally, differences up to 3% were found at the lung heterogeneity interfaces and up to 4% within the lung region for the $2 \times 2\,\mathrm{cm}^2$ field size of both 6 and 18 MV photon beams. Such remaining slight differences might be attributable to the fact that MC calculations are computing the dose on biological materials, whereas experimental measurements are carried out on plastics.

The agreement of AXB and AAA with MC in terms of D_w was evaluated using gamma index analysis with an acceptability criterion 2% dose difference and 2 mm DTA. The passing rate is presented in table 5.4 for all the studied configurations.

5.3.2.1.1 Lung. AXB dose distributions along the phantom with lung-equivalent material were in excellent agreement with MC (within 2%) beyond the depth of maximum dose in most cases (see figures 5.4 and 5.5). Maximum differences of 4% were found within the first 1 to 3 cm after the interface water/lung for the $2 \times 2\,\mathrm{cm}^2$ field size of both 6 and 18 MV photon beams. In this case, the passing rate was 96.1% and 92.5%

	AXB						AAA			
	lung		bone		bone (D_m)		lung		bone	
Field size (cm^2)	6 MV	18 MV	6 MV	18 MV	6 MV	18 MV	6 MV	18 MV	6 MV	18 MV
2x2	96.6	92.5	-	-	-	-	88.9	54.1	-	-
5x5	99.7	99.8	74.3	75.5	97.3	99.1	82.4	75.8	72.4	71.5
10x10	99.7	99.8	79.9	75.6	99.1	99.5	66.1	71.3	77.1	70.6
20x20	99.5	99.6	87.9	78.0	99.1	97.8	29.6	96.9	68.7	66.8

Table 5.4: Percentage of points with a gamma index above 1 with a dose/distance criterion of 2%/2 mm.

for the 6 MV and 18 MV, respectively. Otherwise, the percentage of points passing the criterion was above 99%. These results are consistent with other publications[147].

AAA provided reasonable accuracy within the lung region except for the smallest field of both photon beam energies, where discrepancies to MC were found to be up to 5.7% and 20.3% for 6 and 18 MV, respectively. The passing rate of AAA central-axis dose distributions was below 80% in most cases, but it increased to 90% when the criteria was raised to 3%-3 mm. In water, AAA systematically overestimated the dose after the lung region by up to 5%.

5.3.2.1.2 Bone. In the phantom with the bone-equivalent heterogeneity we found excellent agreement between AXB and MC when reporting the dose in terms of D_m (see figure 5.6); the passing rate was above 99% in most cases, which is consistent with other publications[147]. However, larger discrepancies—up to 4.5% for the 18 MV photon beam—were found within the bone region when using D_w. The origin of such differences might reside in the conversion procedure. The methods used by AXB and MC to convert the results into D_w are distinct: whereas AXB uses an in-flight method to give the D_w by multiplying the energy-dependent fluence by the dose-response function of water in the output grid voxel, the MC dose distributions are converted once the simulation has finished by using the corresponding $S_{w,med}$. The $S_{w,bone}$ used in this study were 1.117 and 1.111 for 6 and 18 MV photon beams, respectively[37]. However, in AXB the jump from D_m to D_w in this region was about 15%. Differences between AXB and MC in terms of D_w in bone of density $\rho = 1.5\,g/cm^3$ have been found to be slightly smaller (around 3% at most) by other authors[153]. The density of the bone used herein was 22% higher, which could be the reason of such disparity of results. Nevertheless, further investigation on this issue needs to be undertaken.

In water, both before and after the bone heterogeneity, AAA provided reasonable accuracy. However, differences in bone were up to 5.9% and 9.6% for 6 and 18 MV, respectively. In this region and for the 18 MV photon beam, AAA was in good agreement with the AXB and MC results expressed in terms of D_m (discrepancies below 2.5%). This results are in good agreement with other studies[61;147;148].

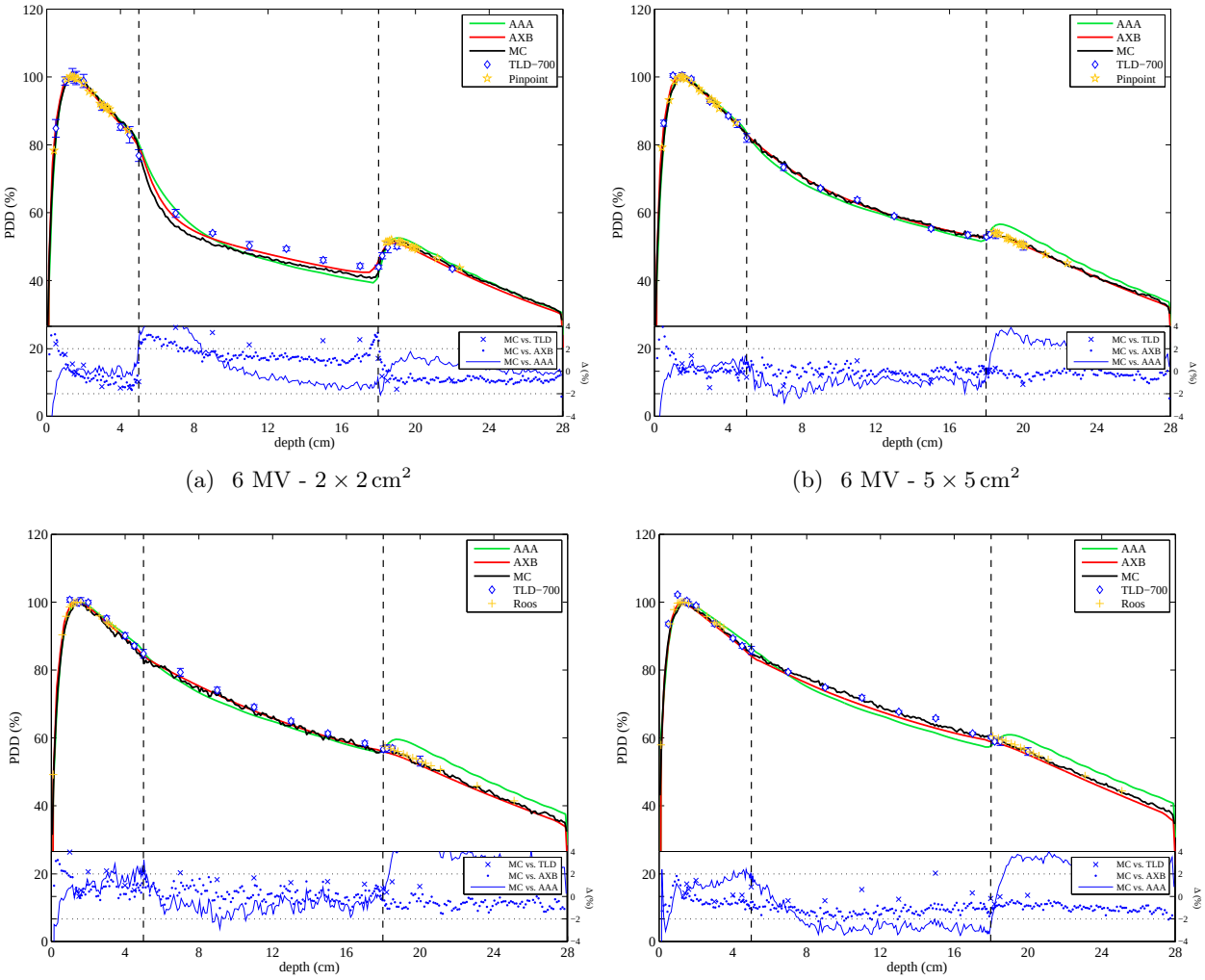

(a) 6 MV - $2 \times 2\,\mathrm{cm}^2$

(b) 6 MV - $5 \times 5\,\mathrm{cm}^2$

(c) 6 MV - $10 \times 10\,\mathrm{cm}^2$

(d) 6 MV - $20 \times 20\,\mathrm{cm}^2$

Figure 5.4: PDD curves for the phantom with the lung-equivalent heterogeneity for 6 MV and different field sizes.

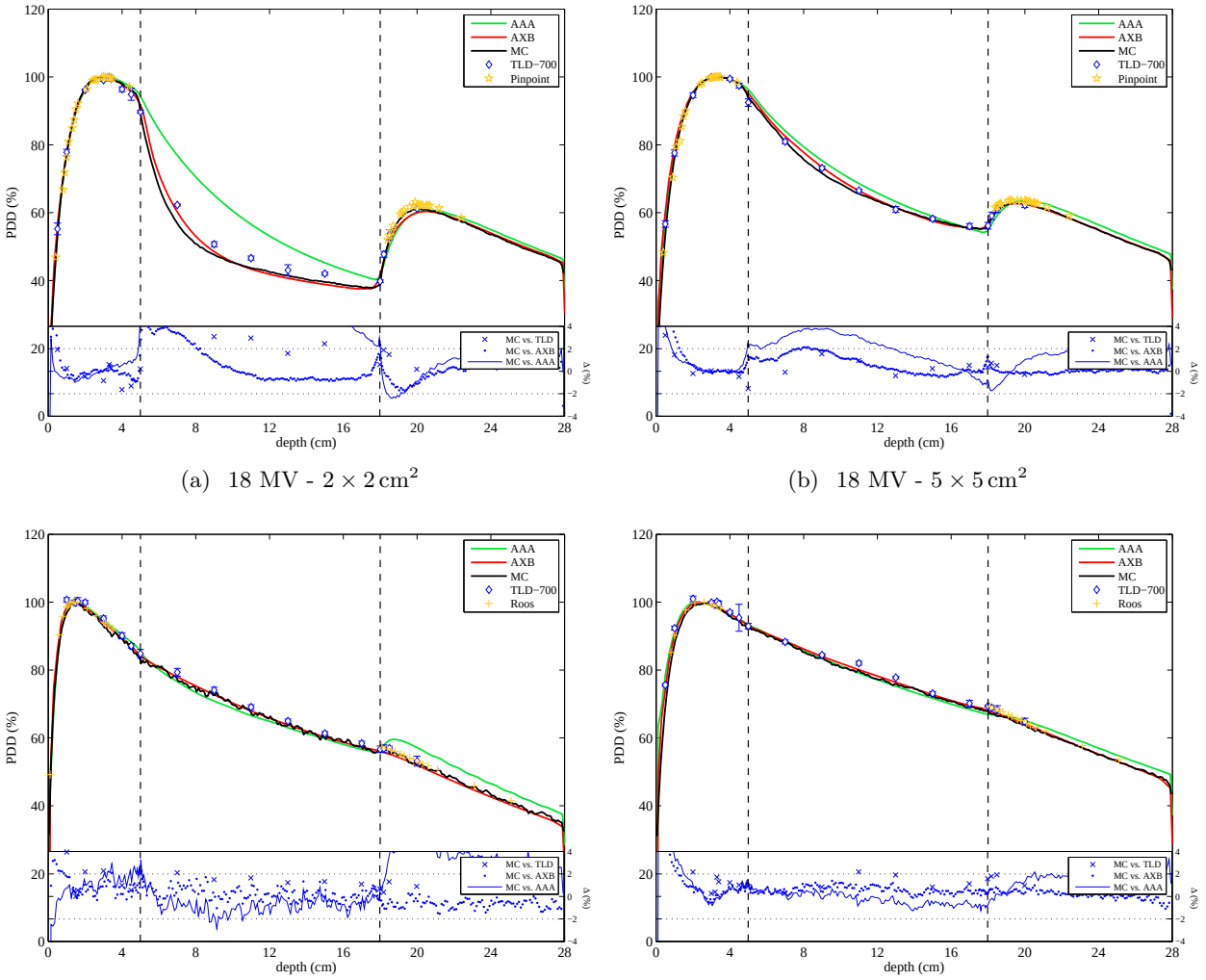

(a) 18 MV - $2 \times 2\,\mathrm{cm}^2$

(b) 18 MV - $5 \times 5\,\mathrm{cm}^2$

(c) 18 MV - $10 \times 10\,\mathrm{cm}^2$

(d) 18 MV - $20 \times 20\,\mathrm{cm}^2$

Figure 5.5: PDD curves for the phantom with the lung-equivalent heterogeneity 18 MV and different field sizes.

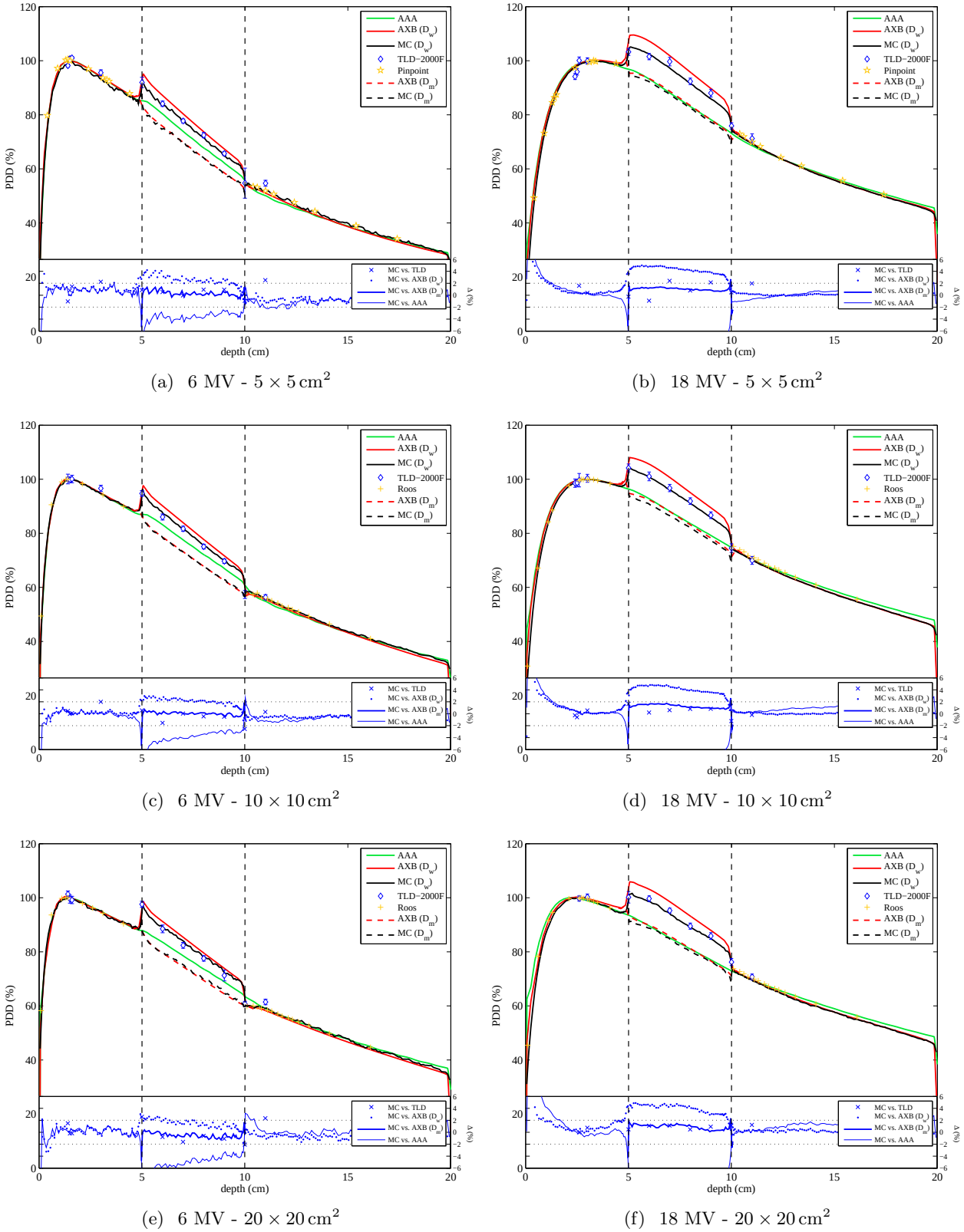

(a) 6 MV - $5 \times 5\,\mathrm{cm}^2$

(b) 18 MV - $5 \times 5\,\mathrm{cm}^2$

(c) 6 MV - $10 \times 10\,\mathrm{cm}^2$

(d) 18 MV - $10 \times 10\,\mathrm{cm}^2$

(e) 6 MV - $20 \times 20\,\mathrm{cm}^2$

(f) 18 MV - $20 \times 20\,\mathrm{cm}^2$

Figure 5.6: PDD curves for the phantom with the bone-equivalent heterogeneity for 6 and 18 MV and different field sizes.

		Lung					
E (MV)	Field size	EBT	MC	AXB	AAA	EBT_w	MC_w
6	$2 \times 2\,cm^2$	7.6	6.6	5.9	6.9	3.6	3.4
	$10 \times 10\,cm^2$	12.6	11.9	11.5	11.4	5.5	5.1
18	$2 \times 2\,cm^2$	10.7	9.7	9.9	6.6	4.9	5.1
	$10 \times 10\,cm^2$	20.9	19.8	20.7	11.6	7.1	6.8
		Bone					
E (MV)	Field size	EBT	MC	AXB	AAA	EBT_w	MC_w
6	$2 \times 2\,cm^2$	3.1	2.9	3.4	3.8	3.6	3.4
	$10 \times 10\,cm^2$	4.3	4.5	4.5	4.7	5.5	5.1
18	$2 \times 2\,cm^2$	3.9	4.1	4.3	4.6	4.9	4.8
	$10 \times 10\,cm^2$	5.2	5.0	5.2	5.3	7.1	6.6

Table 5.5: Beam penumbrae (mm) for 6 and 18 MV photon beams and two different field sizes: $2 \times 2\,cm^2$ and $10 \times 10\,cm^2$. Measured (EBT) and calculated (MC) beam penumbrae in water (w) are also shown.

5.3.2.2 Lateral profiles

Measured and calculated dose profiles are shown in figure 5.7 for two field sizes: $2 \times 2\,cm^2$ and $10 \times 10\,cm^2$. Beam penumbrae are specified in table 5.5 for the two phantoms.

EBT films yielded the relative dose within 2% statistical uncertainty. The statistical uncertainty associated to MC was 2% (2 SD). The agreement was within 3% in all cases. Discrepancies in beam penumbrae were below 1.1 mm and 0.2 mm in lung and in bone, respectively.

5.3.2.2.1 Lung. AXB and MC dose profiles were in good agreement (see figure 5.7 (a) and (b)). Differences in beam penumbrae were below 1.7 mm in all cases.

For the 6 MV photon beam, AAA dose profiles were in good agreement with those calculated by MC—differences in beam penumbra were below 1.7 mm in all cases. However, AAA was unable to correctly predict the penumbra widening effect in lung for 18 MV photon beam regardless of the field size and discrepancies in beam penumbra exceeded 9 mm for the $10 \times 10\,cm^2$ field size compared to MC.

5.3.2.2.2 Bone. AXB and MC dose profiles were in good agreement for all beam configurations. Differences in beam penumbrae were within 0.4 mm in all cases.

Dose profiles were correctly predicted by AAA. Maximum differences in beam penumbrae were 0.7 mm with respect to MC.

5.3.3 On the material assignment in AXB

AXB, AAA and MC PDD curves were calculated on the CT images of the phantoms and compared to those corresponding to the virtual phantoms. Percentage differences are displayed in figures 5.8 and 5.9 for the lung and bone configurations, respectively.

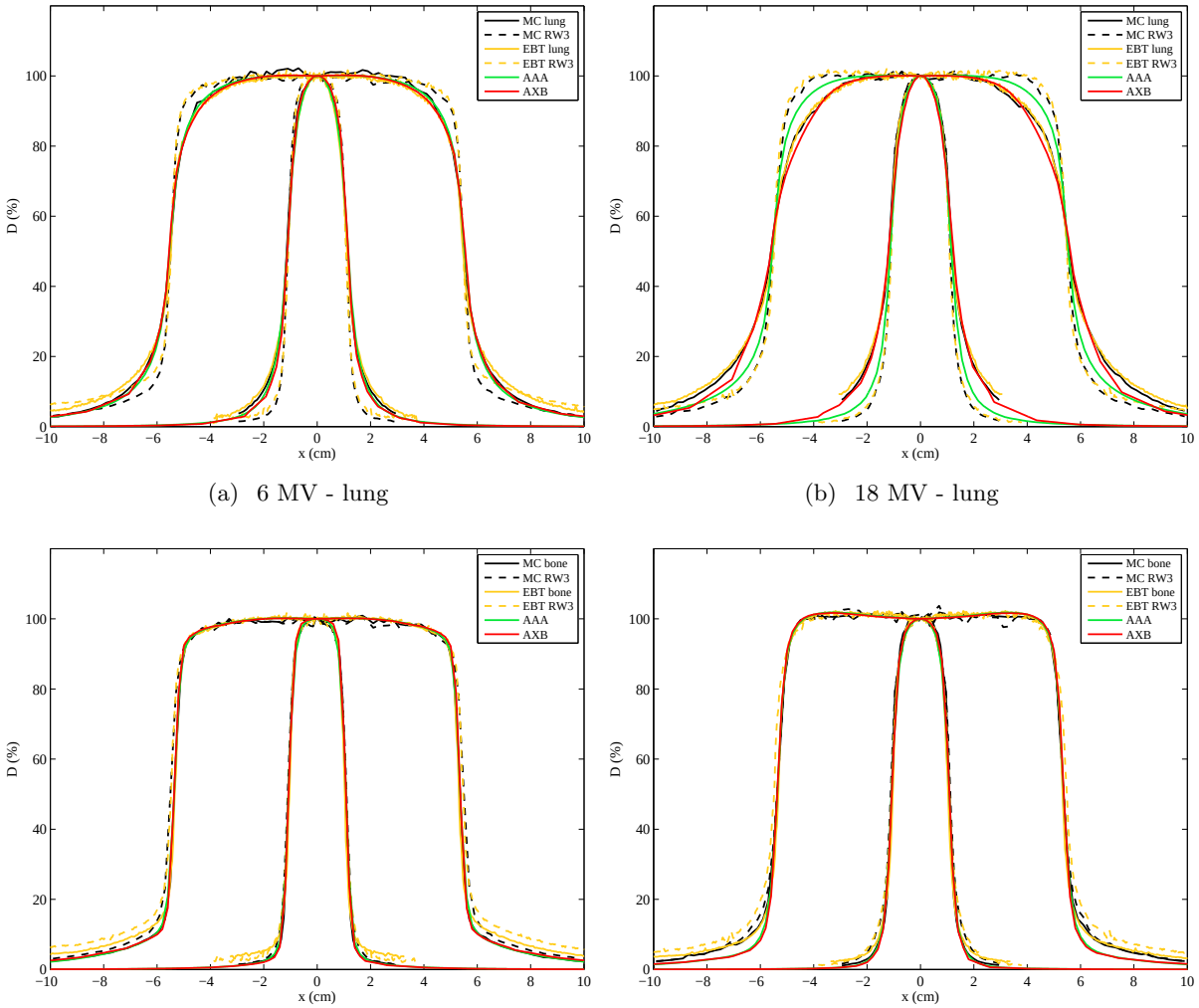

(a) 6 MV - lung

(b) 18 MV - lung

(c) 6 MV - bone

(d) 18 MV - bone

Figure 5.7: Dose profiles for two different field sizes ($2 \times 2\,\mathrm{cm}^2$ and $10 \times 10\,\mathrm{cm}^2$) in lung (figures (a) and (b)) and bone (figures (c) and (d)). Measured (EBT) and calculated (MC) dose profiles in RW3 are included in this plot to evaluate the spectral change of the curve.

In general, differences were found to be below 2% beyond the dose maximum except for the 18 MV photon beam in the phantom with the lung heterogeneity, where discrepancies of 4% were registered both for AXB and MC within the first centimeters of lung and in water after the heterogeneity. On the contrary, no significant differences where found in any case for the phantom with the bone-equivalent material. AAA yielded identical dose distributions both on the generated virtual phantoms or on the CTs (discrepancies below 2% in all cases).

To further investigate the origin of these differences, depth-dose curves were compared in terms of absolute doses for the beam energies and field sizes selected. The comparison for the 18 MV and the $5 \times 5\,\mathrm{cm}^2$ field size is shown in figure 5.10 for the two heterogeneous phantoms. From figure 5.10 (a) it can be stated that the differences observed on the right column (top and bottom) in figure 5.8 on the water region after the heterogeneity arose from the normalization procedure. Differences of about 4% were actually observed in the first centimeters of the phantom with the lung-equivalent heterogeneity. The cause of this change in dose when using the CT instead of the virtual phantom is a combination of factors that can be understood from figure 5.11. First, water is not among the materials that AXB can assign automatically; therefore, AXB (and MC in this case) will assign muscle to those voxels with HU around 0 (see figure 5.3), whose effective atomic number (Z_{eff}) is very close to that of water. However, the HU of the voxels adjacent to the first heterogeneity interface slightly decrease due to the presence of lung as an artifact of the CT scanner, as shown in figure 5.12. As a consequence, the material assigned to that region appears to be adipose tissue (see figure 5.11 (a))—whose Z_{eff} is around 0.9 times that of water. For this reason, the absorbed dose was lower than that reported when calculating on the virtual phantom within the first centimeters of the phantom. This was not the case for the phantom with the bone-equivalent heterogeneity. Whereas HU fluctuations are also observed in the water regions adjacent to the interfaces, in this case the HU are increased owing to the presence of bone in such a way that the material assigned is cartilage (see figure 5.11 (b)). Z_{eff} of cartilage is again very close to that of water and the dose distributions on the virtual phantom and on the CT are in good agreement. To confirm these findings we computed with MC the dose distributions on the virtual phantom with the lung-equivalent material replacing the first 5 cm of water for 5 cm of (i) adipose tissue, (ii) muscle and (iii) cartilage. Results are depicted in figure 5.13 in terms of D_{w} together with the differences with respect to water computed as $D_{\mathrm{tissue}}/D_{\mathrm{water}}$. As expected, the dose around the depth of dose maximum is about 4% lower for adipose than for water. On the contrary, slight differences (1-2%) are observed for muscle and cartilage.

For the sake of completeness, the 18 MV PDD curves on the phantom configuration with lung for the $2 \times 2\,\mathrm{cm}^2$ and $10 \times 10\,\mathrm{cm}^2$ in absolute doses are shown in figure 5.14.

Around the dose maximum, both IC and TLD measurements were in good agree-

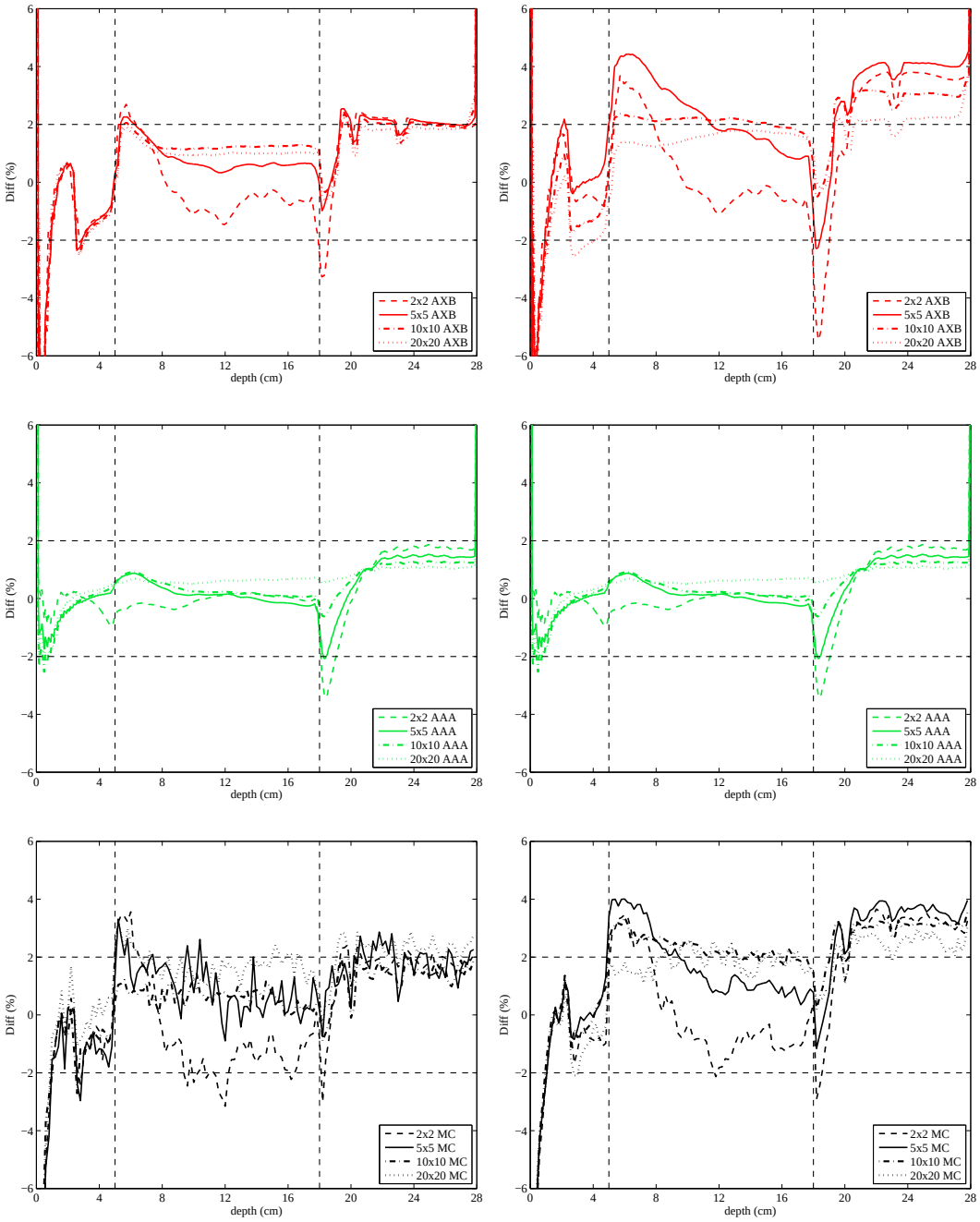

Figure 5.8: Differences between the calculation on the virtual phantom and on the CT for the lung configuration for 6 MV (left column) and 18 MV (right column).

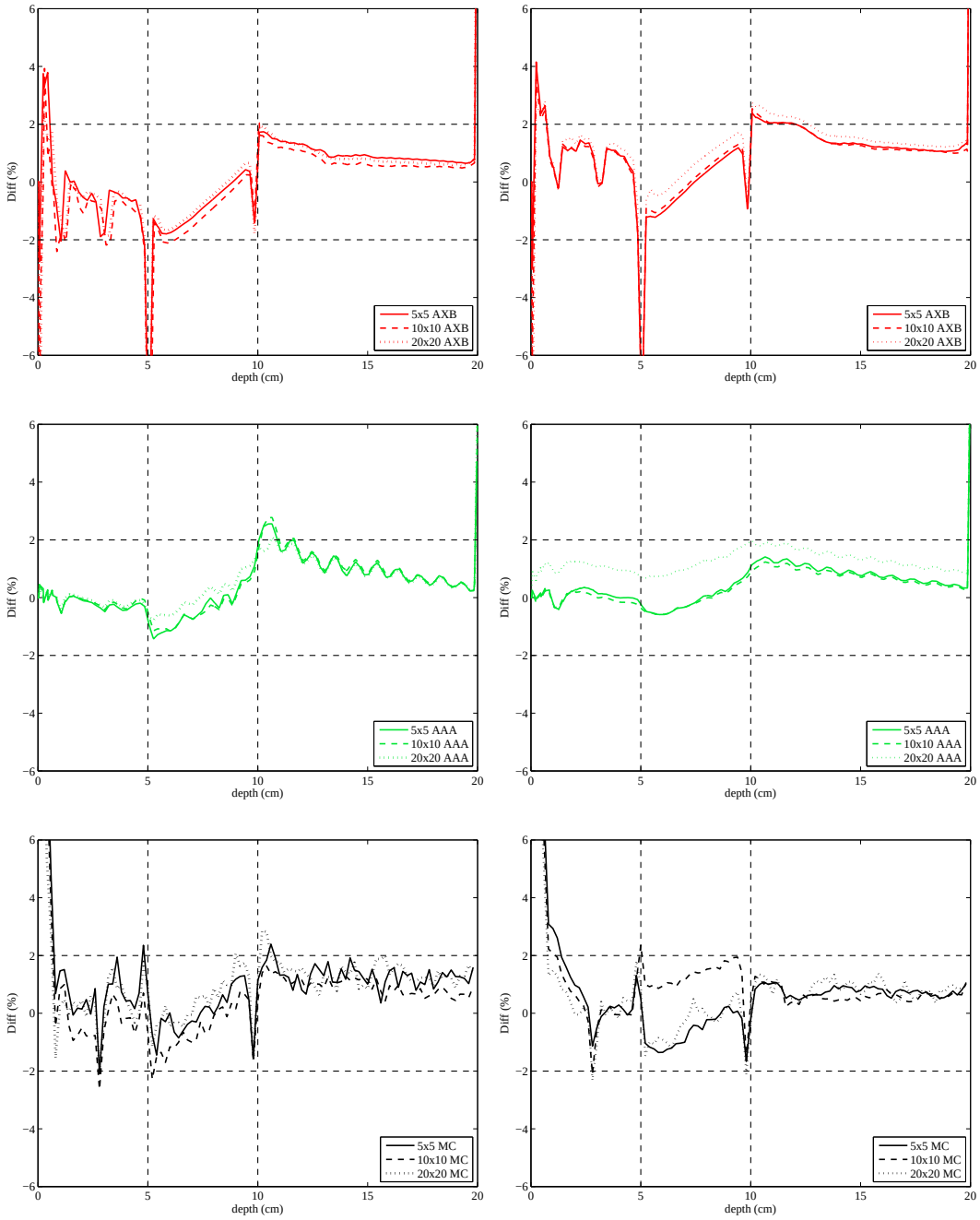

Figure 5.9: Differences between the calculation on the virtual phantom and on the CT for the bone configuration for 6 MV (left column) and 18 MV (right column).

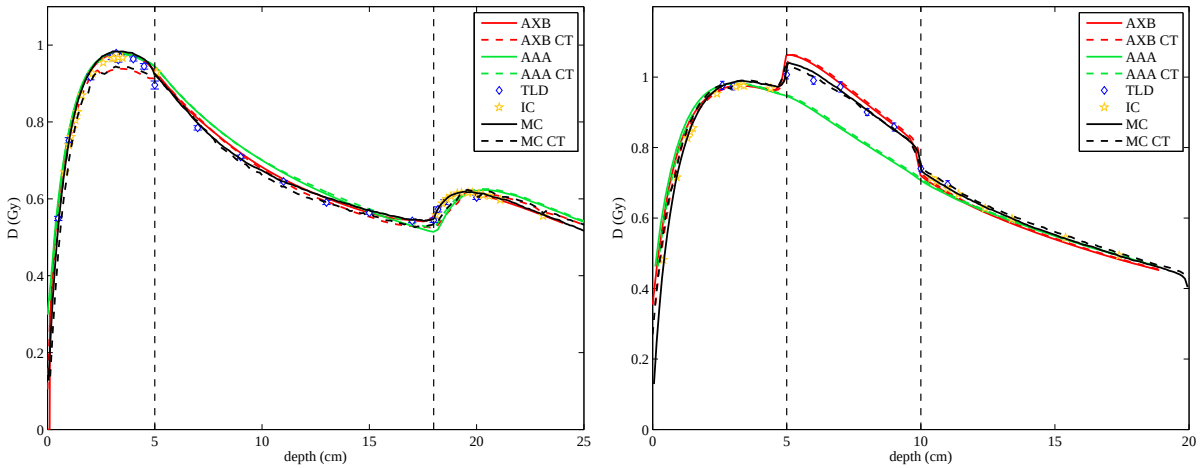

(a) lung configuration (b) bone configuration

Figure 5.10: Central-axis curves on both phantoms in absolute doses for the 18 MV photon beam and the $5 \times 5\,\mathrm{cm}^2$ field size. AXB, MC and AAA calculations on the virtual phantom (continuous lines) and on the CT images (discontinuous lines). Experimental measurements are also depicted.

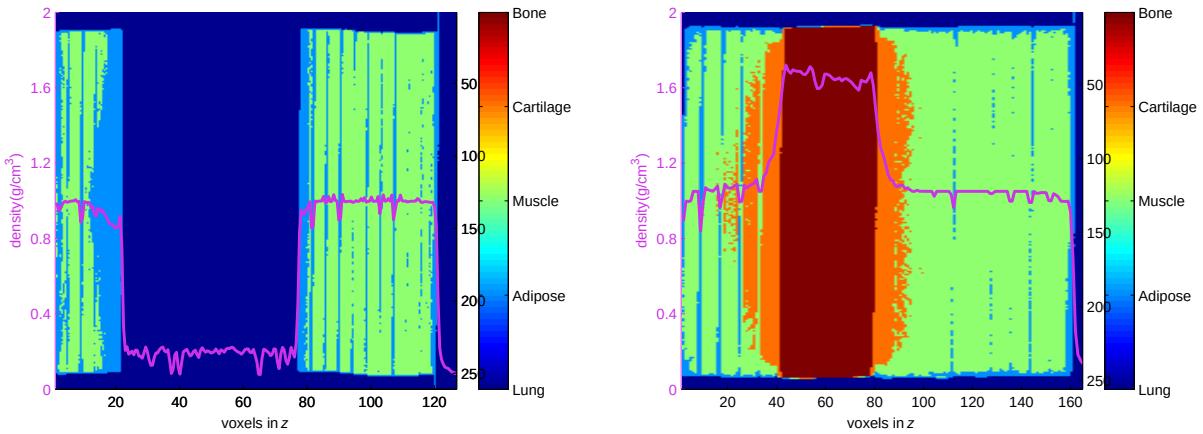

(a) lung configuration (b) bone configuration

Figure 5.11: CT slices of both phantom configurations showing the material assigned to each voxel and the density along the central axis of the phantom based on the conversion in figure 5.3.

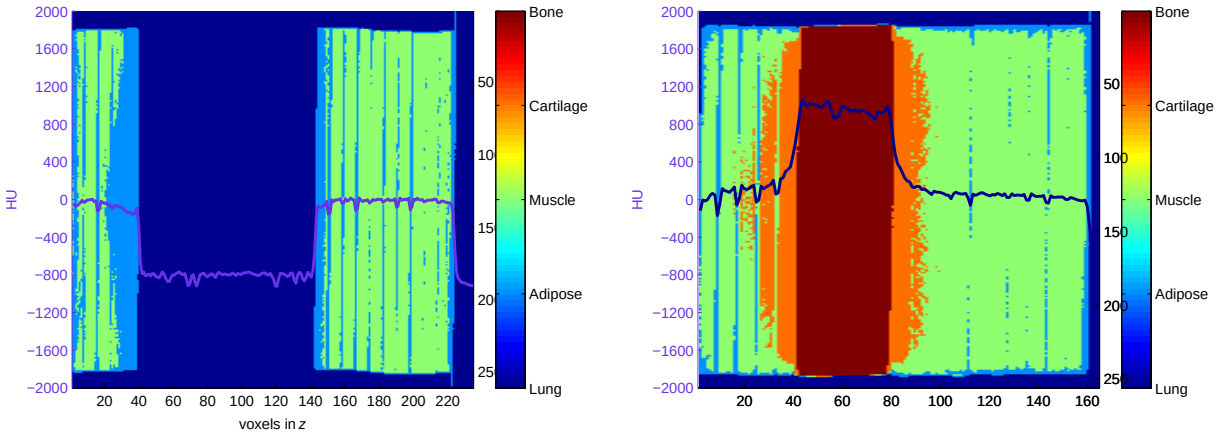

(a) lung configuration

(b) bone configuration

Figure 5.12: CT slices of both phantom configurations showing the material assigned to each voxel and the HU-values along the central axis of the phantom based on the conversion in figure 5.3.

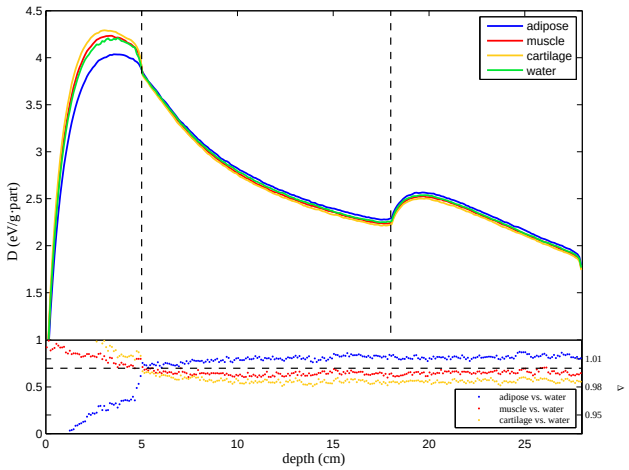

Figure 5.13: MC-computed depth-dose distributions for 18 MV ($5 \times 5\,\mathrm{cm}^2$) on the virtual phantom with the lung-equivalent heterogeneity for adipose tissue, muscle and cartilage (in terms of D_w) on the first 5 cm compared to water.

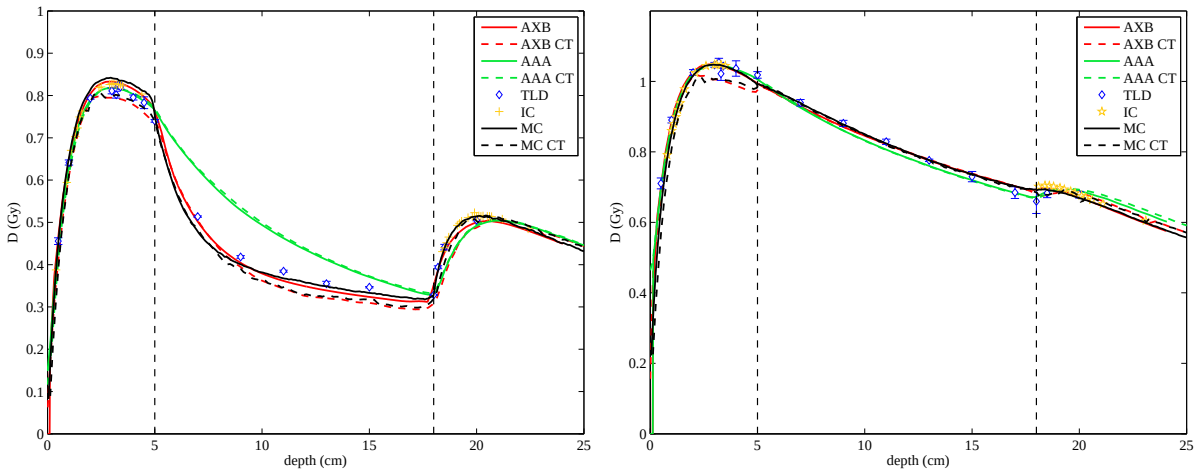

(a) lung configuration - $2 \times 2\,\mathrm{cm}^2$ (b) lung configuration - $10 \times 10\,\mathrm{cm}^2$

Figure 5.14: Absolute central-axis curves in the phantom with lung for the 18 MV photon beam. AXB, MC and AAA calculations on the virtual phantom (continuous lines) and on the CT images (discontinuous lines). Experimental measurements are also depicted.

ment with the AXB and MC doses calculated using virtual phantoms. This should be taken into account when performing experimental validations of this version of the algorithm. From these findings, discrepancies of a few percent might derive from the material assignment procedure rather than being dosimetric limitations of the algorithm. In those regions where the mass density (or HU-value) is very close to a minimum/maximum value of two different materials, the discrete nature of the material assignment procedure and slight fluctuations of HU caused by CT artifacts may lead to an alternation between two different material assignments. This might turn into non-negligible changes (of 4%) in dose distributions, particularly in the boundaries of materials with substantially different atomic number. This issue might be solved in the forthcoming version of AXB. Some authors have given details on AXB version 11.0.02, a pre-clinical engineering release[160;161]. One of the main differences between the two AXB versions (10 and 11) is given by the different strategy in the density-to-media assignment, as shown in table 5.6. With respect to version 10, version 11 includes a refinement related to the issue discussed herein. Apart from including automatic assignment of the Air material to very low density regions inside body, the density range per each material was slightly extended with an overlap of densities between adjacent materials. In the overlapping range, the elemental composition is considered as a proportional mixture of the previous and next material. Note the large overlap between cartilage and bone; for these two tissues, the difference in calcium content plays a fundamental role in the dose calculation phase (to medium and/or water)[160].

Material	Density (g/cm^3)	
	Low	High
Air	0.000	0.020
Lung	0.011	0.624
Adipose tissue	0.554	1.001
Muscle, skeletal	0.970	1.093
Cartilage	1.056	1.600
Bone	1.100	3.000

Table 5.6: Material mass densities in AXB (v.11.0.02). From Fogliata *et al.*[160].

5.4 Conclusions

We evaluated the dose accuracy provided by the AXB (v.10.0.28) advanced dose calculation algorithm inside tissue heterogeneities by means of both experimental measurements (IC, TLD and EBT films) and MC simulations for the first time. For 6 MV and 18 MV and different field sizes, PDD curves and dose profiles were evaluated on two slab water phantoms: one containing lung-equivalent material and another one containing bone-equivalent material. We also included AAA in the comparisons as the current standard in ECLIPSE^{TM}.

The experimental measurements were in good agreement (within statistical uncertainties) with MC in all cases. Remaining differences may originate from the fact that MC simulations used biological materials whereas plastics were used in the experimental setup.

Generally, the accuracy provided by AXB was comparable to that of MC simulations in all situations. Central-axis depth-dose curves predicted by AXB were in good agreement with MC and experimental measurements for the phantom with the lung-equivalent heterogeneity. On the contrary, AAA v.10.0.28 was unable to correctly predict the dose in lung when the beam energy was set to 18 MV and the field size to $2 \times 2\,\mathrm{cm}^2$. Moreover, AAA tended to overestimate the dose in the water region after the lung-equivalent material. In bone, an excellent agreement was found between AXB and MC in terms of D_m. Discrepancies were more significant when comparing in terms of D_w. The question of which quantity—D_w or D_m—should be adopted for comparison purposes is still under debate[83;86] and there are strong arguments both for using one or the other. However, from the results found in this study we suggest that the dose is compared in terms of D_m preferably for the benchmarking of the algorithm with MC. In contrast to AXB, doses reported by AAA were highly inaccurate in bone, where the results were closer to those of AXB and MC in terms of D_m—despite AAA reports D_w.

AXB was able to correctly predict the widening and shrinking effects in beam penumbrae of dose profiles relative to those in water due to the presence of low-density or high-density materials, respectively. These results are in good agreement with recent publications[147;153]. AAA did not properly predict the widening effect of the beam

penumbra in lung, but lateral profiles in bone were obtained with reasonable accuracy since the penumbra shrinking phenomenon in bone is mild. The results are consistent with previous studies[58;147].

CT acquisition yielded slight fluctuations of HU-values in the regions adjacent to the heterogeneities which affected the materials assignment in the different regions of the phantoms. AXB and MC dose distributions were influenced by the material assignment in both phantom configurations. Consequently, dose differences up to 4% were found in the water region before the lung heterogeneity when comparing against the PDD curves calculated on virtual phantoms—where a single HU-value was manually assigned to each region of the phantoms. On the contrary, AAA dose distributions were unaltered by the density change of the voxels when using CT images. One should bear this in mind when comparing AXB version 10 dose distributions against experimental measurements. This issue might be solved in the forthcoming clinical version 11.

In conclusion, AXB provides comparable results to MC simulations under similar conditions. Hence, AXB is a good alternative to MC and undoubtedly represents a significant improvement over the widely-used AAA.

Chapter 6

Quantifying lateral tissue heterogeneities in proton therapy fields

This section was partially developed at the Massachusetts General Hospital (MGH) & Harvard Medical School in Boston, Massachusetts, USA.

6.1 The need for Monte Carlo dose calculation in proton therapy

Proton therapy has become one of the most attractive modalities for the treatment of cancer due to the unique dosimetric features of protons[162–164]. The characteristic depth-dose distributions of proton beams (see figure 1.2 in chapter 1) result in a significantly reduced integral dose compared to photon treatments. These physical attributes, in turn, increase the impact of uncertainties in the delivered dose. As mentioned in chapter 1 section 1.3, these uncertainties arise from the planned dose distributions predicted by dose calculation algorithms[15], imaging or delivery uncertainties and inter- or intra-fractional geometry changes[16;17]. In this study we focus on the uncertainties in dose distributions predicted by the treatment planning system arising from the complexity of the patient geometry.

Modern pencil beam algorithms account for proton energy losses and Coulomb scattering, but the physical models exhibit dosimetric limitations that become noticeable for highly inhomogeneous media. Thus, analytical calculation models can predict dose distributions with an acceptable precision in simple geometries[78;165], but uncertainties still remain in the presence of complex density heterogeneities within the beam path. Although attempts have been made to account for heterogeneities lateral to the beam direction[78;166;167], pencil beam algorithms commonly use a one-dimensional

dose-scaling method of a proton pencil beam in water. Thus, the multiple Coulomb scattering in modeled in the dose kernel but the radial distribution at each depth only accounts for inhomogeneities upstream of the pencil's central axis[81]. The assumption of such slab geometry might induce dose errors in the presence of lateral heterogeneities that result in significant difference between the planned and delivered dose to the target volume.

Special considerations must be taken into account when the target volume is reduced. Firstly, small lesions often require high-dose single-fraction treatments involving a small number of fields, *i.e.* potential errors from one field will not be compensated by other fields. Secondly, the smaller the field size, the lower the number of pencil kernels involved in the calculation and therefore, the higher the effect of dose inaccuracies of single pencil kernels on the final convolution. Further, the dosimetry of small proton beams is challenging from a planning and delivery perspective because of aperture scattering and charged particle disequilibrium—fields with aperture diameters smaller than $\approx 7\,\text{cm}$ require field-specific output factor corrections to compensate for aperture scattering effects[168]. The impact of small proton fields on dose calculations has been previously studied[169;170]. Bednarz, Daartz, and Paganetti[171] evaluated the accuracy of dose distributions predicted by a pencil beam algorithm in the XiO treatment planning system for a set of patients with small lesions. The authors pointed out the dosimetric limitations of the algorithm resulting in hot and cold spots and range degradation in the target volume due to scattering in heterogeneities. Although the reported discrepancies appeared clinically acceptable ($< 3\%$[19]) over the multiple fields conforming the treatment, differences up to 8.6% in the dose covering at least 95% of the target volume (D95) were found for a single field.

As mentioned in chapter 1 section 1.4.2, Monte Carlo (MC) computations are considered the golden standard for dose calculation in radiotherapy and are expected to be especially valuable in those situations where the limitations of dose calculation algorithms appear to be more prominent, *e.g.* for small fields in the presence of heterogeneities[172]. However, MC dose calculations might be time-consuming. On the other hand, for the cases where the expected errors in the planned dose exceed a particular tolerance level, devoting some time to obtain a more reliable dose distribution might be undoubtedly worthwhile.

The aim of this study was to obtain a fast and easy-to-calculate indicator that predicts the reliability of planned dose distributions for small passively scattered proton beams based on the level of tissue inhomogeneities in the patient and evaluates the potential need for Monte Carlo dose calculations. For this purpose, the accuracy of the treatment planning process was assessed by comparing the planned dose distributions to Monte Carlo simulations for a set of small proton therapy fields. The differences in the dose covering at least 50% of the gross tumor volume (D50) between the pencil beam algorithm predictions and the Monte Carlo calculations were evaluated for the

selected fields. A heterogeneity index (HI) was introduced by Pflugfelder *et al.*[79] as a method to quantify lateral tissue heterogeneities of scanned proton beams. Based on this concept, a HI for passively scattered proton beams was proposed in this study. The HI was intended to (i) entail a simple calculation methodology and (ii) require a short computation time. Finally, the correlation between the differences in D50 and the tissue heterogeneities within the beam path as parameterized by the HI was analyzed.

6.2 Methodology

6.2.1 Patient population

Fourteen head and neck patients (A-N) treated at our facility with proton beams were selected. The study was done under IRB approval (IRB protocol 2010-P-002050/1; MGH: "Improving treatment planning and dose prediction in radiation therapy by retrospective data analysis.").

The gross tumour volumes (GTVs) ranged from 0.1 cc to 30 cc.

Eight patients (A-H) were stereotactic patients and six (I-N) required fractionated radiotherapy. A total of 38 fields were analyzed.

The relevant characteristics of the selected clinical cases are summarized in table 6.1.

To define a field size parameter, we computed the diameter of the aperture as that of a circle with the same area as the actual field. Field sizes defined accordingly ranged from 2 cm to 7 cm diameter (ϕ). Field sizes smaller than $\phi = 2$ cm were excluded from this study because they are prone to uncertainties in the output factor correction required to compensate for aperture scattering effects[168]. These effects might alter the prediction of the error made by the analytical algorithm based on the geometrical complexity of the patient exclusively. The analysis of these effects is beyond the scope of this chapter.

6.2.2 Patient dose evaluations

6.2.2.1 Treatment planning system at MGH

The treatment planning system CMS/XiO (XiO, Computerized Medical Systems Inc.) uses an in-house PB algorithm which is based on the physics model developed by Hong *et al.*[81] in terms of modeling device effects and lateral spread. At each point, the dose $D(x, y, z)$ of a single pencil kernel is factorized into a depth-scaled central axis dose $C(z)$ and a lateral fluence distribution $O(x, y, z)$:

$$D(x, y, z) = C(z) \cdot O(x, y, z) \tag{6.1}$$

The off-axis term is approximated by a Gaussian profile:

		ϕ_{field}(cm)									
Patient	GTV (cc)	ϕ_1	ϕ_2	ϕ_3	ϕ_4	ϕ_5	ϕ_6	ϕ_7	ϕ_8	ϕ_9	ϕ_{10}
A	0.90	2.7	2.1	2.1	-	-	-	-	-	-	-
B	0.18	2.2	2.3	-	-	-	-	-	-	-	-
C	0.07	2.7	-	-	-	-	-	-	-	-	-
D	0.75	1.9	1.9	2.3	-	-	-	-	-	-	-
E	7.49	5.0	4.9	3.5	3.5	-	-	-	-	-	-
F	30.1	6.7	6.7	5.9	-	-	-	-	-	-	-
G	11.4	6.5	6.1	-	-	-	-	-	-	-	-
H	1.13	2.2	2.2	2.2	-	-	-	-	-	-	-
I	3.00	3.9	3.7	3.7	3.5	3.7	3.7	2.5	2.5	2.4	2.5
J	2.64	2.9	-	-	-	-	-	-	-	-	-
K	21.5	4.5	-	-	-	-	-	-	-	-	-
L	3.75	4.8	2.5	-	-	-	-	-	-	-	-
M	12.0	5.0	-	-	-	-	-	-	-	-	-
N	27.9	6.8	7.1	-	-	-	-	-	-	-	-

Table 6.1: Tumour volume (GTV) and field size (aperture diameter, ϕ) for the selected patients.

$$O(x,y,z) = \frac{1}{2\pi[\sigma(z)]^2} \exp\left(-\frac{x^2+y^2}{2\pi[\sigma(z)]^2}\right) \tag{6.2}$$

where $\sigma(z)$ is the standard deviation and it is determined by adding the contributions of the virtual source size ($\sigma_{src}(z)$), the scatter in the range compensator ($\sigma_{rc}(z)$) and the scatter in the patient ($\sigma_p(z)$) (please see Hong *et al.*[81] for more details):

$$\sigma(z)^2 = \sigma_{src}(z)^2 + \sigma_{rc}(z)^2 + \sigma_p(z)^2 \tag{6.3}$$

Currently, all treatment plans at MGH are based on this PB. Plans were generated by Brian Winey.

As in other analytical algorithms, the dose calculation is based on the water-equivalent properties of each CT voxel. Thus, a look-up table is used to convert HU into relative stopping power. The dose distribution calculated by XiO is a relative dose distribution to the prescribed dose to the target volume.

The beam output factor is defined at our facility as the dose delivered at the calibration point divided by the required monitor units (MU) given by an ionization chamber located in the treatment head. Since XiO does not model the treatment head to perform the dose computation, output factors—or absolute doses—need to be modeled or measured at our facility. Models to predict such output factors were established for a large set of ranges considering standard machine settings with standard aperture sizes and no range compensator[173]. Daartz *et al.*[168] quantified the effect of the field size on the output factor to validate dose calculations by performing measurements for a set of aperture sizes and ranges. The results revealed a remarkable influence of the aperture size on the output factor. Therefore, a field-size specific correction factor is applied

clinically to correct the measured/modeled output[168].

6.2.2.2 MC simulations for proton dose calculations

All simulations were performed with TOPAS[30;31] (see chapter 3 section 3.1.3.1 for more details).

The dose computation is based on the CT of the patient. The conversion from HU to elemental composition and mass density of each voxel is done according to Schneider, Bortfeld, and Schlegel[88] with an extension to deal with high HU corresponding to high-density materials (*e.g.* titanium)[174]. To account for the CT scanner properties at the MGH, a density correction factor is applied to normalize the density used by MC to match the HU versus relative stopping power table integrated in the planning system.

The simulation was done in two steps, as stated earlier in this manuscript (see section 3.1.3.4). First, protons were tracked through the treatment head (nozzle). The particle type, energy, position and angular momentum for particles that crossed a plane at the exit of the treatment head (after the field-specific devices—aperture and compensator) were stored in a phase space file. For the field sizes considered, the simulation efficiency through the nozzle was only about 3% for the smallest fields, *i.e.* only 3% of the protons at nozzle entrance reached the patient. A total of 10^8 histories were simulated per field to ensure the statistical uncertainty to be $< 1\%$ for doses in the target volume. In order to reduce computation times and improve the statistics of the results, the calculations were split into 20 separate—statistically independent—simulations that ran in parallel on 20 separate CPUs. Each of the 20 separate simulations took ≈ 12 hours to complete on a single node of the computing cluster with a 3 GHz CPU. The second step tracked the particles stored in the phase space plane through the patient geometry. The calculation time for in this step ranged from 1.5 to 5 hours for a single calculation on the same computing nodes. Variance reduction techniques were implemented in the code to reduce computation time and statistical uncertainties[108]. Two particle split planes were defined inside the treatment head and protons reaching these planes were split into 4 protons with their weight adjusted accordingly.

In order to obtain absolute doses, the dose at the center of the SOBP in a water phantom was calculated in a separate simulation. This calibration was performed for an open field without aperture and compensator. The MC was re-normalized by the appropriate field-size correction factor mentioned in section 6.2.2.1. Instead of being taken from Daartz *et al.*[168], output factors were calculated with TOPAS for each selected beam by computing the quotient of the dose at the center of the SOBP simulated with and without the specific aperture. The computed output factors were generally in good agreement with those derived from the table in Daartz *et al.*[168] (differences below 2%).

6.2.2.3 Dose comparisons

The dose grid reported by XiO is coarser than the CT grid. MC simulations were performed on the CT grid with the XiO scoring grid layered on top of the CT grid in a parallel world. Parallel worlds is a Geant4 feature that allows objects—such as scoring grids—to be placed on top of physical volumes without affecting the physics processes and simulations. Whenever a particle deposits energy, this energy is converted to the equivalent dose using the material of the CT voxel in which the energy deposit happened. The dose is then scored in the parallel XiO grid. The final dose distribution on the XiO grid is the sum of all energy deposits from all histories in the simulations. The MC dose was reported on the planning grid for comparison purposes.

The MC computations were tailored to yield dose to water using the methodology described by Paganetti[85].

The discrepancies in the dose that the 50% of the GTV receives, D50, were assessed. Although the mean dose to the target is commonly used, we believe it is not the most appropriate in this case because it can be insensitive to hot and cold spots within the region of interest—the presence of underexposed and over-irradiated regions can compensate each other.

6.2.3 A Heterogeneity Index HI

We aimed at finding a parametrization to quantify the complexity of tissue heterogeneities within the beam path. Pflugfelder *et al.*[79] presented the concept of the HI as a method to assess the lateral tissue heterogeneities for scanned proton beams. From this fundamental idea, we developed a novel technique to obtain a HI for passively scattered proton beams according to the dose calculation approach taken by the PB algorithm used at MGH.

6.2.3.1 Definition

The HI computation was based on the CT of the patient. To evaluate the tissue heterogeneities we assessed the relative stopping power (S_{rel}) of each CT voxel. The conversion from HU to S_{rel} was obtained from the calibration curve of our CT scanner.

For the definition of HI the coordinate system was set so that the central axis of the proton beam coincides with the z axis, its origin is at the surface of the patient and the z axis points towards the isocenter.

An HI-value was defined for each treatment field individually. For passively-scattered proton beams the 3D dose calculation results from the convolution of several pencil kernels. Hence, the HI was defined as of the contribution of a number n of indexes HI_i, one defined for each pencil kernel i.

The index associated to a pencil kernel i, HI_i, whose central axis is located at $P = (x_i, y_i)$, is defined as follows. First, at a depth z_k, HI_{ik} is computed as the sum

of the square differences between S_{rel} of the surrounding points on the $x-y$ plane and S_{rel} of the central axis of the kernel, weighted by the lateral fluence distribution ($\phi(x_j, y_j, z_k)$):

$$HI_{ik}(x_i, y_i) = \frac{\sum_{j \in T_i(z_k)} \phi_i(x_j, y_j, z_k) \cdot [S_{rel}(x_j, y_j, z_k) - S_{rel}(x_i, y_i, z_k)]^2}{\sum_{j \in T_i(z_k)} \phi_i(x_j, y_j, z_k)} \tag{6.4}$$

where $T_i(z_k)$ is the appropriate set of sampling points in the $x-y$ plane at depth z_k. The lateral fluence $\phi(x_j, y_j, z_k)$ is approximated by a Gaussian distribution with standard deviation $\sigma_i(z_k)$, as described in section 6.2.2.1 (equation 6.3). $\sigma_i(z_k)$ determines $T_i(z_k)$; all points closer than $3\sigma_i(z_k)$ to the central axis of the pencil kernel i are considered for the calculation.

Then, lateral tissue heterogeneities computed at each depth as described in equation 6.4 are assessed from the surface of the patient, $z_0 = 0$, up to a depth equal to the prescribed range after the compensator, R_i (in water equivalent distance). The index associated to the pencil kernel i is the addition along the studied length:

$$HI_i(x_i, y_i) = \sum_{k=0}^{k=R_i} HI_{ik} \tag{6.5}$$

The surface of the patient was considered to be the skin contour delineated during the planning process for each patient. No contributions were considered outside this contour. R_i was was defined as the prescribed range in water (R')—distal 90% dose level of the SOBP—minus the maximum thickness of the range compensator expressed in terms of water-equivalent thickness (rc_w): $R_i = R' - rc_w$. Thus, a single R_i, named R, was used regardless of the location of the pencil kernel. In our case, this was a good approximation since for small target volumes the modulation of the range compensator over the target volume area is small—usually below 5 mm. Therefore, the error associated with this assumption is considered to be small.

The computations described in equations 6.4 and 6.5 are performed for each pencil kernel involved in the dose calculation. Finally, the HI associated with the proton beam is defined as the median of the indexes $HI_i(x_i, y_i)$ for all pencil kernels:

$$HI = \left[\widetilde{HI_i}\right]_{i \in A}^{1/2} \tag{6.6}$$

where A represents the beam effective area within which pencil kernels are sampled. Voxels receiving a dose higher than 90% of the maximum dose at the isocenter slice were considered to belong to A. We sampled the pencil kernels within A on the CT so that the spacing between them was 2 mm—the spacing used by the analytical algorithm (set by manufacturers for the optimization). The sampling points were taken from the existing voxels of the CT grid. The size of the selected area determined the number of

pencil kernels.

The median provides a measure that is more robust than the mean in the presence of outliers or extreme values, which can increase the mean of the indexes HI_i considerably without altering the dose to the 50% of the GTV volume substantially.

The aforementioned description of the calculation of the HI is represented schematically in steps in figure 6.1.

With this parametrization, heterogeneities lateral to the central axis of each pencil kernel will increase HI. For a homogeneous phantom HI would be zero. Note that HI as defined in this section is unitless.

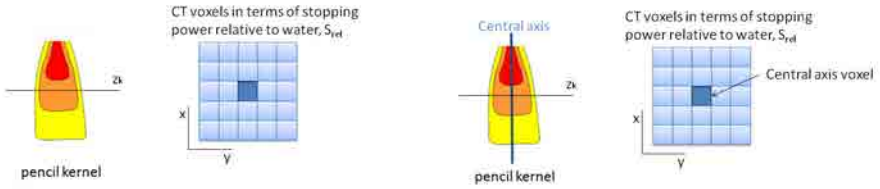

(a) At a particular depth z_k of the pencil central axis.

(b) Selection of the central axis voxel at z_k.

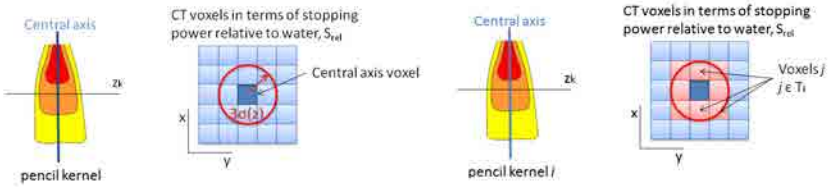

(c) Selection of all surrounding voxels ¡ $3\sigma(z_k)$.

(d) Computation of square differences of S_{rel}-values.

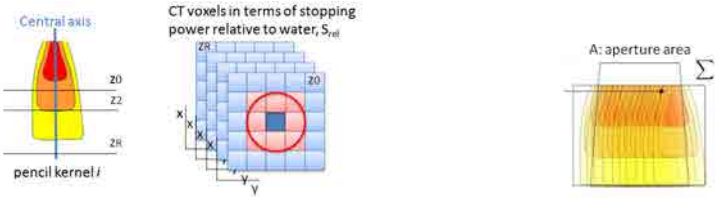

(e) Repetition at all depths.

(f) Integration for all pencil kernels in the field.

Figure 6.1: Schematic representation in steps of the HI calculation.

6.2.3.2 Setup and practical considerations for the HI calculation

All information involved in the HI calculation was available from the treatment planning system.

For a particular patient, plan and treatment field, a user interface was used to generate a text file that contained relevant information. Among others, the following data relevant for this study was gathered in this file: number and dimension of CT

voxels in x, y and z (n_x, n_y, n_z and dx, dy, dz, respectively), dimensions of the CT cube, gantry angle (α_g), couch angle (β_c), isocenter position, prescribed range in water (R'), maximum thickness of the range compensator (rc) and prescribed dose.

The 3D dose distribution from the treatment planning was used to select the CT voxels traversed by the proton beam. The planning system reports the dose on a grid that is coarser than the CT grid. Moreover, it has its own coordinates system whose origin is shifted with respect to the CT origin. The size of the planning grid is stored in the text header of the dose distribution file and the offset between the 3D planned dose and the CT is specified in the aforementioned text file. With this information, the CT and the 3D planned dose were co-registered. In this step the dose distribution was re-sampled on the CT grid to maintain the highest possible resolution regarding S_{rel} assignments.

To simplify the calculation of the HI described in section 6.2.3.1, the CT grid was rotated according to α_g and β_c for each field so that the CT voxels align parallel to the beam axis. Both the CT and planned dose distribution were re-sampled in this new rotated grid by interpolating S_{rel} and dose values—thereby, each z slice of the dose distribution was a 2D representation of the beam lateral dose profile. This interpolation of S_{rel} represents a source of uncertainty regarding material assignments that might be significant when analyzing voxels individually. However, the error added in this step does not affect HI substantially since the index encompasses the global contribution of several hundreds of voxels within the beam path; therefore, voxel-specific differences in S_{rel}-values have a negligible effect in the HI.

Eventually, the HI is intended to be implemented in the clinical routine. Consequently, the HI was designed to entail a fast calculation and be easy to implement if readers intent to use our formalism in their planning environment.

6.3 Results

6.3.1 Comparison between MC and analytical dose calculations

For the set of patients selected the DVHs predicted by the PB algorithm were compared against those derived from MC dose calculation on a field-by-field basis. A maximum difference of 5.4% in D50 was found for one of the fields of patient G (figure 6.2).

Figures 6.2-6.4 show the DVH comparison for one of the fields of patients G, D and I, respectively. Among these three examples the largest difference was found for the field of patient G, with a discrepancy in D50 of 5.4%. The beam delivery based on XiO overestimated the dose to the GTV by 3.4% for the field displayed for patient D. The difference observed for patient I was within MC uncertainties (0.8%).

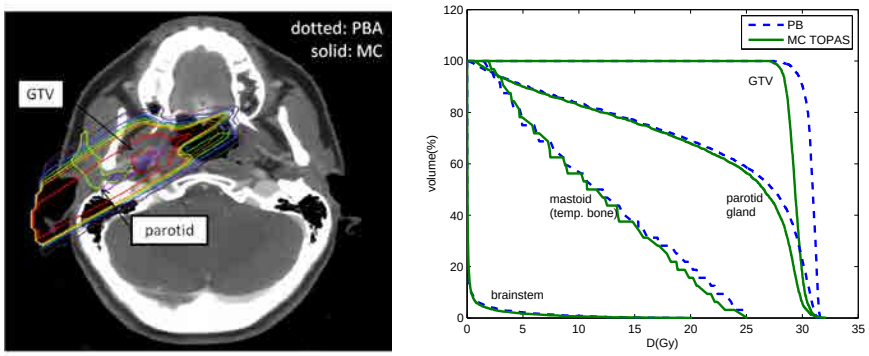

(a) (b)

Figure 6.2: DVHs and comparison of the dose distribution predicted by the treatment planning system (PBA) and the MC dose calculation (MC) for one of the fields of patient G. The GTV and several organs-at-risk were considered.

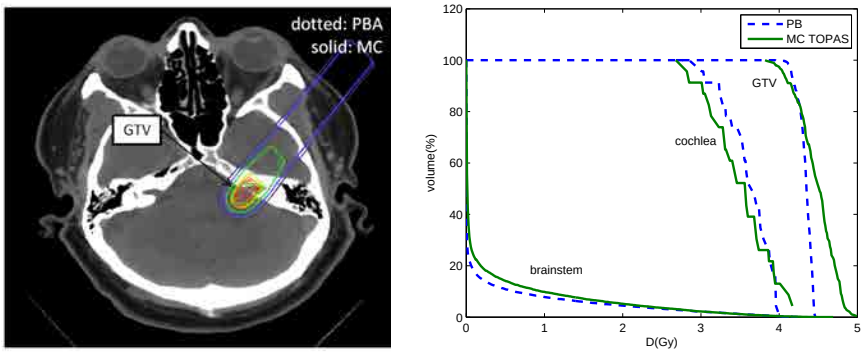

(a) (b)

Figure 6.3: DVHs and comparison of the dose distribution predicted by the treatment planning system (PB) and the MC dose calculation (MC) for one of the fields of patient D. The GTV and several organs-at-risk were considered.

6.3.2 HI-values

The heterogeneities within the proton beam path were analyzed as described in section 6.2.3 for the set of patients selected. The whole process to obtain the HI-values for each field—including the co-registration procedure, the assessment of $\sigma_i(z)$ and the HI calculation—took less than 3 minutes to complete on both, a single Windows computer with an Intel®Core$^{TM}i5$ processor (2.4 GHz) or a single iMac with an Intel®Core$^{TM}2$ Duo processor (2 GHz). The HI values obtained for each studied field ranged from 0.9 for the field with the most homogeneous beam path (patient I, ϕ_4), to 3.4 for the field traversing the greatest level of heterogeneities (patient G, $\phi = 2$).

In figures 6.5-6.7 three of the studied proton beams are depicted. The fields are

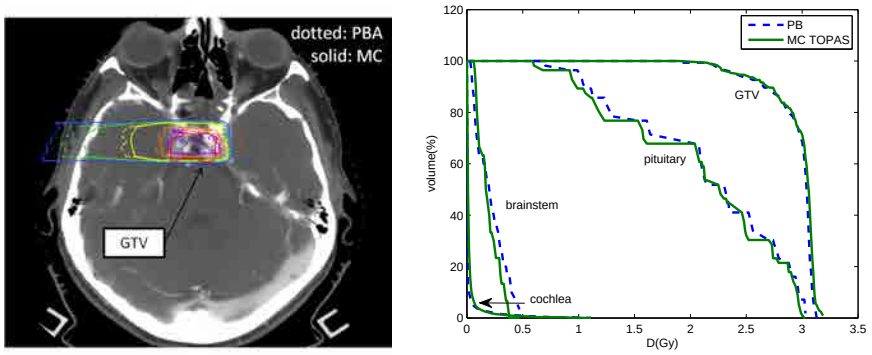

(a) (b)

Figure 6.4: DVHs and comparison of the dose distribution predicted by the treatment planning system (PB) and the MC dose calculation (MC) for one of the fields of patient I. The GTV and several organs-at-risk were considered.

from patients G, D and I, respectively, and correspond to the same fields for which the DVH comparison is shown in the previous section. In each figure, the images correspond to the isocentric slices of the CT and the planned dose distribution after the co-registration—images (a) and (b), respectively—, and the CT voxels traversed by the proton beam—image (c). The field of patient G had an associated HI-value of 3.39 and the index associated to the field of patient I was 1.01. The field belonging to patient D had an intermediate HI-value of 1.73.

The HI-values obtained were well correlated to the level of tissue inhomogeneity as seen in the third-column images of figures 6.5-6.7. The field shown for patient G traversed a complex heterogeneous region with bony structures. In the case of patient D, a small region of high-density tissue was within the beam path. Finally, the complexity of the tissue traversed by the field of patient I was substantially lower than the first two examples, and so was its HI-value.

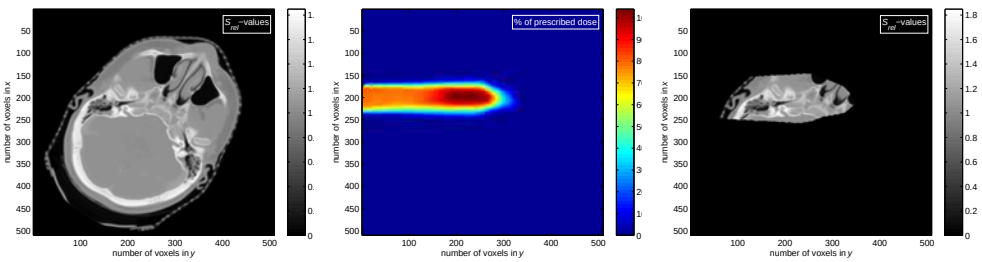

(a) CT isocenter slice (b) Dose cube isocenter slice (c) Beam path

Figure 6.5: Patient G, $\alpha_g = 125^{\circ}$, $\beta_c = 0^{\circ}$. HI-value is 3.39. Difference in D50 is 5.4%.

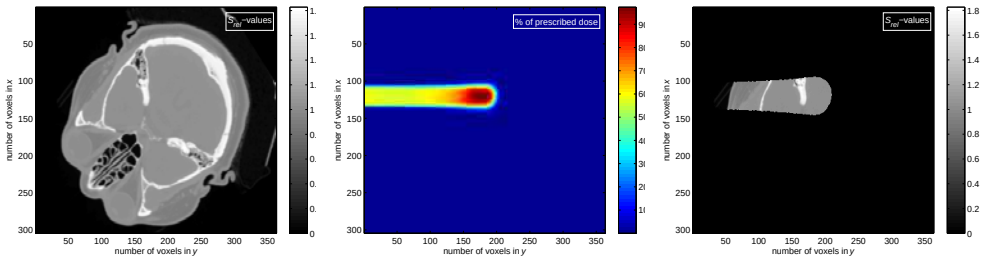

(a) CT isocenter slice (b) Dose cube isocenter slice (c) Sampling voxels

Figure 6.6: Patient D, $\alpha_g = 325^o$, $\beta_c = 0^o$. HI value is 1.73. Difference in D50 is 3.4%.

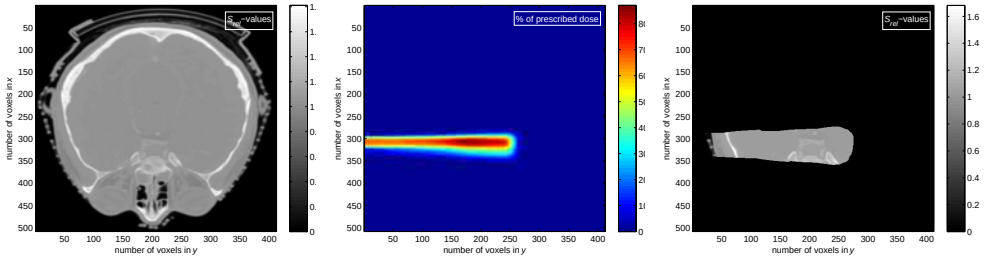

(a) CT isocenter slice (b) Dose cube isocenter slice (c) Sampling voxels

Figure 6.7: Patient I, $\alpha_g = 270^o$, $\beta_c = 0^o$. HI value is 1.01. Difference in D50 is 0.8%.

6.3.3 HI *vs.* dose discrepancies

Figure 6.8 shows the differences in dose to the GTV (in terms of D50) between our PB algorithm predictions and the MC calculations as a function of HI. Each point represents a single field. Statistical uncertainties associated with the MC dose calculations were within 1-2%; error bars are not shown in the graph for clarity.

A strong correlation (Spearman's rank correlation coefficient [175]: ρ=0.8, $p < 0.0001$) was found between our implementation of HI and the discrepancies in dose for the studied fields. Among the analyzed fields only two might be labeled as outliers (located in the lower-right quadrant of figure 6.8. In these two cases, despite the beam path being quite inhomogeneous according to their associated HI-values (1.87 and 2.60) the analytical algorithm agrees well with the MC calculations for the dose to 50% of the GTV (discrepancies with respect to MC are below 0.1% and around 1.4%, respectively). In these cases, under and over-dosage due to multiple Coulomb scattering may have canceled out.

A line was fitted to the data to help the reader see the correlation. A threshold value for HI, HI_T, can be determined from this fit for a given tolerance level.

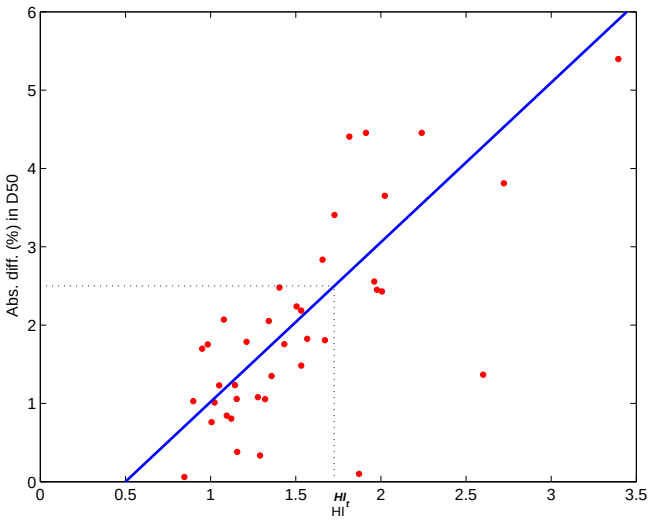

Figure 6.8: Absolute differences (in %) in the dose covering 50% of the GTV volume (D50) (i) derived from our treatment planning system based on analytical dose calculations and (ii) calculated with MC as a function of HI for the studied patients. Each point represents a single field.

6.4 Discussion

We have confirmed that PB algorithms can not properly predict the dose to the target in the presence of complex lateral tissue heterogeneities for small proton beams, as reported previously[171]. The reason lies in the approximation of multiple Coulomb scattering, which breaks down in complex geometries[15]. Some of the differences for single fields found exceeded the tolerance levels commonly accepted in treatment delivery. However, over multiple fields, all treatments were within clinical tolerance levels.

The heterogeneity index, HI, presented in this study parameterizes the inhomogeneity of the tissue traversed by passively scattered proton beams. The HI was formulated according to the calculation approach taken by a PB algorithm that is based on the physics model developed by Hong *et al.*[81] and can thus be applied in general to algorithms based on it. HI-values for each field were obtained in less than 3 minutes fulfilling our primary goal to provide a fast calculation to estimate the necessity for MC simulations.

The HI-approach presented here works best for small proton fields, such as those included in this study. For larger fields, variations in HI within the field might be too large to allow a characterization of the geometry based on an average HI alone. Very small fields were excluded from this study (aperture diameters $<$ 2cm) for the following reasons. For such small fields, the aperture is so small that electronic equilibrium is substantially compromised and experimental investigations might be required in addition to perform dose calculations by the planning system with a field-size dependent output factor correction. Effects from aperture scattering, air gap sizes, compensator scattering and scattering inside the patient (not related to the heterogeneity) contribute

more to dose differences than the scattering caused by the heterogeneity of the patient.

Differences in the delivered dose to the target—in terms of D50—between the predictions by the treatment planning system and the MC calculations were found to be strongly correlated to HI, as shown in figure 6.8. With the established relation, a tolerance level of 2.5% leads to a threshold HI-value of 1.73. Indices below this value indicate that dose delivery errors are very likely to be within the clinical tolerance ($< 3\%$). For those HI-values exceeding the threshold, analytical dose calculations become prone to clinically significant errors. Only two cases—5% of the total fields studied—seemed not to fit this tendency and showed lower discrepancies in D50 than expected based on their associated HI-value.

HI-values close to the established threshold will not be conclusive. Based on the overall impact on the complete treatment, other aspects—such as the total number of fields involved in the treatment—should be taken into account in addition to the HI to finally decide whether or not MC calculations are needed for a particular case.

The definition of HI presented in this study is adjusted to the GTV volume. If the volume of interest was different, such as the PTV, the methodology should be subtly adapted so that the pencils sampling area would cover the whole volume.

6.5 Conclusions

Depending on their distribution relative to the treatment field and on the field size, density heterogeneities are difficult to handle correctly by pencil beam algorithms, mainly due to range degradation effects caused by multiple Coulomb scattering. For small fields, analytical calculations in patients might misevaluate the dose in the target volume by several percent when the proton beam is traversing a highly inhomogeneous region.

In this study we suggested a simple and fast methodology, the heterogeneity index, HI, to estimate the tissue inhomogeneities traversed by a small proton beam. The complexity of tissue heterogeneities quantified in this way was found to be strongly correlated to the dose differences within the target volume between the treatment planning system and the Monte Carlo calculations. The higher the level of inhomogeneities within the beam path, the larger the discrepancies found. Consequently, the HI can be used to predict whether a specific field arrangement is associated to considerable absolute dose uncertainties. In that case, this methodology suggests that either a change in the beam incidence (if feasible) or a Monte Carlo dose calculation of the plan should be considered. Other aspects will influence the final decision based on the particularities of each case.

The HI involves a very short computation time—the whole procedure to obtain the index takes less than 3 minutes to complete on a single Windows or iMac with 2 GHz processor. Therefore, the HI can be implemented in the clinical routine as a potential

indicator of the need for treatment plan verification with Monte Carlo simulations.

Conclusions

This thesis was devoted to solve some of the current concerns on the absorbed dose determination in the presence of tissue heterogeneities in external radiotherapy.

According to the outline presented in section 2, the main achievements and contributions of this thesis are listed below:

I. Two different Monte Carlo (MC) codes have been successfully employed to provide reliable calculations that were used as the reference throughout the development of the tasks involved in this thesis, both for photon and for proton therapy fields.

II. This thesis has provided knowledge of the suitability of several detectors to accurately determine the absorbed dose in bone for megavoltage (MV) photon beams. LiF:Mg,Cu,P (MCP-Ns and TLD-2000F) and LiF:Mg,Ti (MTS-7s) ultra-thin thermoluminescent dosimeters (TLDs), as well as radiochromic films (EBT), were considered assuming that their reduced size might entail low perturbation effects at first approximation.

- MCP-Ns, MTS-7s and TLD-2000F were found to be suitable for absorbed dose measurements in radiotherapy showing no significant energy dependence (variations within 2.5%) neither for megavoltage photon (including flattening-filter-free energies) nor electron beams. MCP-Ns and TLD-2000F exhibited a linear response with the absorbed dose whereas the use of MTS-7s deserves a word of caution due to their two-step supra-linear response—MTS-7s must be calibrated within the appropriate linearity range.

- The use of MCP-Ns, MTS-7s and EBT for the absorbed dose determination in the presence of bone requires the application of a perturbation correction factor of the order of 4-5%.

- Among the detectors studied herein, TLD-2000F (20 μm-thick cylindrical films) would be the detector of choice for accurate absorbed dose measurements in bone providing negligible (<2%)—though observable—electron energy fluence perturbation effects. However, the MC simulations revealed that a detector up to 50 μm-

thick would be small enough to provide reliable dose measurements regardless of its material composition.

III. This thesis has contributed to the thorough examination of the behavior of Acuros XB v.10.0.28 (AXB) in the presence of high-density and low-density heterogeneities.

- The accuracy provided by AXB was comparable to that of MC simulations (agreement within 2%) under similar conditions both in the presence of lung and bone and therefore, AXB represents an undoubtedly improvement over the worldwide-used current standard algorithms based on analytical calculations.

- The discrete nature of the material assignment in AXB in combination with small Hounsfield Units (HU) (*i.e.* density) fluctuations caused by artifacts originated during CT image acquisition especially around the interfaces leaded to significant changes (4%) on the absolute dose calculation. This rapid alternation between two different material assignments must be born in mind when comparing against experimental measurements, which will not be affected by such CT image artifacts. Forthcoming versions of AXB might have solved this issue.

IV. This thesis has released an algorithm—the heterogeneity index (HI)—to easily predict the expected dose uncertainties during treatment planning based on the quantification of patient tissue heterogeneities within the beam path. The HI can be used to assess the potential need for MC dose calculations.

- The HI was a good estimator of the complexity of the tissue inhomogeneities traversed by the particle beam. Its calculation entailed a very short computation time allowing its application in the clinical routine without interfering with the workflow.

- Analytical dose calculation algorithms cannot properly predict the dose to the target volume in the presence of complex density heterogeneities when small proton beams are being delivered and differences to MC dose calculations might exceed the clinical tolerance levels commonly accepted in treatment planning.

- The HI was found to be a good indicator for the accuracy of dose distributions predicted analytical dose calculation algorithms and therefore, it can be used to easily predict whether a MC dose calculation should be considered for a particular patient.

Along this line, the main results of the thesis have been published in scientific journals and presented at professional society meetings.

All in all, it can be concluded that some of the issues on the absorbed dose determination in the presence of tissue heterogeneities addressed in this thesis still deserve further research. As for photons therapy, forthcoming versions of AXB should be studied to test the impact of the material assignment procedure on the dose distributions in more complex geometries to estimate the influence in the patient outcome for a complete treatment. Further, the calculation of perturbation correction factors for ionization chambers in high-density and low-density heterogeneities would be of utmost interest. As for proton therapy, the availability of an algorithm capable of dealing with heterogeneities with high accuracy would be a further step towards dose calculation during treatment planning.

List of Publications

This thesis work has given rise to several oral presentations and posters at scientific conferences, and papers published in (or submitted to) peer-reviewed journals.

Contributions to conferences proceedings

- **M. Bueno**, M. A. Duch, P. Carrasco, N. Jornet, "Caracterización de los dosímetros termoluminiscentes ultra-finos LiF:Mg,Cu,P (MCP-Ns) para su uso en radioterapia y aplicación práctica en la determinación de la dosis absorbida en hueso". National Congress of the Radiation Protection Spanish Society and the Medical Physics Spanish Society (SEFM & SEPR). May 2010, Sevilla, Spain.

- **M. Bueno**, P. Carrasco, M. A. Duch, M. Ginjaume, M. Ribas, "Which are the most suitable detectors for the absorbed dose determination in bone?". European Society for Therapeutic Radiation Oncology (ESTRO) 29th Conference. Young Scientist Session oral presentations. September 2010, Barcelona, Spain.

- **M. Bueno**, M. A. Duch, D. Jurado-Bruggeman, S. Agramunt-Chaler and C. Muñoz-Montplet, Dosimetric verification of Acuros XB in heterogeneities against experimental measurements and Monte Carlo simulation. Radiother. Oncol., **103**, supplement 1, S515 (2012)—oral communication in ESTRO 31st, Barcelona, Spain.

- C. Muñoz-Montplet, S. Agramunt-Chaler, D. Jurado-Bruggeman, **M. Bueno** and M. A. Duch, Dosimetric validation of Acuros XB in water. Radiother. Oncol., **103**, supplement 1, S510 (2012)—ESTRO 31st, Barcelona, Spain.

- **M. Bueno**, J. Schuemann, M. A. Duch and H. Paganetti, A method to assess the need for clinical Monte Carlo dose calculation for proton therapy fields. Med. Phys., **39**, 3874 (2012)—oral communication in the American Association of Physicists in Medicine (AAPM) 54th Annual Meeting, Charlotte, 2012.

- N. Lopez-Vilanova, **M. Bueno**, D. Sevillano, C. Mínguez, M. Ginjaume, A. Sánchez-Reyes, M. A. Duch, Dosimetric verification of helical tomotherapy against

experimental measurements for head&neck treatments. Med. Phys. **39**, 3770 (2012)—AAPM 54th Annual Meeting, Charlotte, 2012.

- **M. Bueno**, J. Schümann, M. A. Duch and H. Paganetti, An algorithm to assess the need for clinical Monte Carlo dose calculation for small proton therapy fields. Radiother. Oncol., **106**, supplement 2, 5168 (2013)—oral communication in ESTRO 2nd Forum, Geneva, Switzerland.

- J. Schümann, M. Testa, C.-H. Min, **M. Bueno**, M. Moteabbed, D. Giantsoudi, S. Dowdell and H. Paganetti, Patient and site-specific assessment of the value of routine Monte Carlo dose calculations in proton therapy, Med. Phys., **40**, 309 (2013)—poster discussion in AAPM 55th, Indianapolis, Indiana.

Articles in peer-reviewed journals

- **M. Bueno**, H. Paganetti, M. A. Duch and J. Schümann, An algorithm to assess the need for clinical Monte Carlo dose calculation for small proton therapy fields based on quantification of tissue heterogeneity, Med. Phys. **40**, 081704 (2013).

- **M. Bueno**, M. A. Duch, D. Jurado-Bruggeman, S. Agramunt-Chaler and C. Muñoz-Montplet, Dosimetric verification of Acuros XB in heterogeneities: a comparison against Monte Carlo simulations and experimental measurements, *to submit* Acta Oncol. .

- **M. Bueno**, M. A. Duch, N. Jornet and P. Carrasco, On the suitability of ultra-thin detectors for the absorbed dose assessment in the presence of high-density heterogeneities, *to submit* Med. Phys. (2013).

- **M. Bueno**, N. Jornet, J. Puxeu and M. A. Duch, Dosimetric characterization of ultra-thin thermoluminescent detectors for radiotherapy beams, *to submit* Radiation Physics and Chemistry (2013).

Bibliography

[1] World Health Organization (WHO), "Globocan," Tech. Rep. (International Agency for Research on Cancer (IARC), 2008).

[2] American Cancer Society (ACS), "Cancer facts and figures 2013," Tech. Rep. (2013) Atlanta, United States.

[3] International Atomic Energy Agency, *Relative biological effectiveness in ion beam therapy*, Technical Reports Series No. 461, IAEA (2008), Vienna.

[4] F. M. Khan, *The Physics of Radiation Therapy*, 3rd ed., edited by J. Pine (Lippincott Williams & Wilkins, Philadelphia, PA, USA., 2003).

[5] E. B. Podgorsak, *Radiation Oncology Physics: a handbook for teachers and students*, edited by E. B. Podgorsak (International Atomic Energy Agency, Viena, Austria, 2005).

[6] J. Y. Chang, X. Xhang, X. Wang, Y. Kang, B. Riley, S. Bilton, R. Mohan, R. Komaki, and J. Cox, "Significant reduction of normal tissue dose by proton radiotherapy compared with three-dimensional conformal or intensity-modulated radiation therapy in stage I or stage III non-small-cell lung cancer," Int. J. Radiat. Oncol. Biol. Phys. **65**, 1087 (2006).

[7] S. E. McGowan, N. G. Burnet, and A. J. Lomax, "Treatment planning optimisation in proton therapy," British Journal of Radiology **86**, 20120288 (2013).

[8] E. J. Hall, "Intensity-modulated radiation therapy, protons, and the risk of second cancers," Int. J. Radiat. Oncol. Biol. Phys. **65**, 1 (2006).

[9] G. Steel, ed., *Basic Clinical Radiobiology* (Oxford University Press Inc., New York, USA, 2012).

[10] O. Jäkel, C. P. Karger, and J. Debus, "The future of heavy ion radiotherapy," Med. Phys. **35**, 5653 (2008).

[11] G. J. Kutcher, L. Coia, M. Gillin, W. F. Hanson, S. Leibel, R. J. Morton, J. R. Palta, J. A. Purdy, L. E. Reinstein, G. K. Svensson, M. Weller, and L. Wing-

field, "Report of the AAPM Radiation Therapy Committee Task Group No. 40: Comprehensive QA for radiation oncology," Med. Phys. **21**, 581 (1994).

[12] E. Heath, J. Unkelbach, and U. Oelfke, "The future of heavy ion radiotherapy," Med. Phys. **36**, 3059 (2009).

[13] R. Mohan and J. Antolak, "Monte Carlo techniques should replace analytical methods for estimating dose distributions in radiotherapy treatment planning," Radiother. Oncol. **28**, 123 (2001).

[14] P. Mavroidis, S. Axelsson, S. Hyödynmaa, J. Rajala, M. A. Pitkänen, B. K. Lind, and A. Brahme, "Effects of positioning uncertainty and breathing on dose delivery and radiation pneumonitis prediction in breast cancer," Acta Oncol. **41**, 471 (2003).

[15] H. Paganetti, "Range uncertainties in proton therapy and the role of Monte Carlo simulations," Phys. Med. Biol. **57**, R99 (2012).

[16] A. J. Lomax, "Intensity modulated proton therapy and its sensitivity to treatment uncertainties 2: the potential effects of inter-fraction and inter-field motions," Phys. Med. Biol. **53**, 1043 (2008).

[17] Z. Hui, X. Zhang, G. Starkschall, Y. Li, R. Mohan, R. Komaki, J. D. Cox, and J. Y. Chang, "Effects of interfractional motion and anatomic changes on proton therapy dose distribution in lung cancer," Int. J. Radiat. Oncol. Biol. Phys. **72**, 1385 (2008).

[18] B. Mijnheer, A. Olszewska, C. Fiorino, G. Hartmann, T. Knöös, J. C. Rosenwarls, and H. Welleweerd, "Quality assurance of treatment planning systems. practical examples for non-IMRT photon beams," Tech. Rep. ISBN 90-804532-7 (European Society for Therapeutic Radiology and Oncology (ESTRO), Mounierlaan 83/12 – 1200 Brussels, Belgium, 2004) first Edition.

[19] International Commission on Radiation Units and Measurements, "Determination of absorbed dose in a patient irradiated by beams of x or gamma rays in radiotherapy procedures," Tech. Rep. 24 (ICRU, Bethesda, MD, 1976).

[20] N. Papanikolaou, J. J. Battista, A. L. Boyer, E. Klein, T. R. Mackie, M. Sharpe, and J. Van Dyck, "Report of the American Association of Physicists in Medicine Task Group No. 65: Tissue inhomogeneity corrections for MV photon beams. report of the AAPM no. 85," Tech. Rep. (AAPM, Medical Physics Publishing, 4513 Vernon Blvd. Madison, WI 53705-4964, USA, 2004).

[21] O. N. Vassiliev, T. A. Wareing, J. McGhee, G. Failla, M. R. Salehpour, and F. Mourtada, "Validation of a new grid-based Boltzmann equation solver for

dose calculation in radiotherapy with photon beams," Phys. Med. Biol. **55**, 581 (2010).

[22] H. Paganetti, H. Jiang, K. Parodi, R. Slopsema, and M. Engelsman, "Clinical implementation of full Monte Carlo dose calculation in proton beam therapy," Phys. Med. Biol. **53**, 4825 (2008).

[23] I. J. Chetty, B. Curran, J. Cygler, J. DeMarco, G. Ezzel, B. A. Faddegon, I. Kawrakow, P. J. Keall, H. Liu, C.-M. C. Ma, D. W. O. Rogers, D. Seuntjens, D. Sheikh-Bagheri, and J. Siebers, "Report of the American Association of Physicists in Medicine Task Group No. 105: Issues associated with clinical implementation of Monte Carlo-based photon and electron external beam treatment planning," Med. Phys. **34**, 4818 (2007).

[24] L. H. Siantar, "Description and dosimetric verification of the PEREGRINE Monte Carlo dose calculation system for photon beams incident on a water phantom," Med. Phys. **28**, 1322 (2001).

[25] I. Kawrakow, "VMC++ , electron and photon Monte Carlo calculations optimized for radiation treatment planning," (Berlin, 2000) pp. 229–236, in Advanced Monte Carlo for Radiation Physics, Particle Transport Simulation and Applications: Proceedings of the Monte Carlo. Meeting Lisbon.

[26] J. Sempau, S. J. Wilderman, and A. F. Bielajew, "DPM, a fast, accurate Monte Carlo code optimized for photon and electron radiotherapy treatment planning dose calculations," Phys. Med. Biol. **45**, 2263 (2000).

[27] M. Rodriguez, J. Sempau, and L. Brualla, "PRIMO: A graphical environment for the Monte Carlo simulation of Varian and Elekta linacs," Strahlenther. Onkol. **65** (2013), dOI 10.1007/s00066-013-0415-1.

[28] M. Fippel and M. Soukup, "A Monte Carlo dose calculation algorithm for proton therapy," Med. Phys. **31**, 2263 (2004).

[29] S. Agostinelli and *et al.*, "Geant4–a simulation toolkit," Nuclear Instruments and Methods in Physics Research Section A: Accelerators, Spectrometers, Detectors and Associated Equipment. **506**, 250 (2003).

[30] J. Perl, J. Schuemann, J. Shin, B. A. Faddegon, and H. Paganetti, *TOPAS: Tool for particle simulation* (2011), (available at http://www.slac.stanford.edu/-perl/topas_ptcog2011.pdf).

[31] J. Perl, J. Shin, J. Schuemann, B. A. Faddegon, and H. Paganetti, "TOPAS: an innovative proton Monte Carlo platform for research and clinical applications," Med. Phys. **39**, 6818 (2012).

[32] A. Nahum, "Water/air mass stopping power ratios for megavoltage photon and electron beams," Phys. Med. Biol. **23**, 24 (1978).

[33] A. E. Nahum, "Perturbation effects in dosimetry: Part I. kilovoltage x-rays and electrons," Phys. Med. Biol. **41**, 1531 (1996).

[34] J. Medin and P. Andreo, "Monte Carlo calculated stopping-power raios, water/air, for clinical proton dosimetry (50-250 MeV)," Phys. Med. Biol. **42**, 89 (2000).

[35] R. F. Laitano and M. Rossetti, "Proton stopping powers averaged over beam energy spectra," Phys. Med. Biol. **45**, 3025 (2000).

[36] J. V. Siebers, P. J. Keall, A. E. Nahum, and R. Mohan, "Converting absorbed dose to medium to absorbed dose to water for Monte Carlo-based photon beam dose calculations," Phys. Med. Biol. **45**, 983 (2000).

[37] J. M. Fernández-Varea, P. Carrasco, V. Panettieri, and L. Brualla, "Monte Carlo based water/medium stopping-power ratios for various ICRP and ICRU tissues," Phys. Med. Biol. **52**, 6476 (2007).

[38] C. Gomà, P. Andreo, and J. Sempau, "Spencer-attix water/medium stopping power ratios for the dosimetry of proton pencil beams," Phys. Med. Biol. **58**, 2509 (2013).

[39] P. Andreo and A. Brahme, "Stopping power data for high energy photon beams," Phys. Med. Biol. **31**, 839 (1986).

[40] International Atomic Energy Agency, *Absorbed dose determination in external beam radiotherapy, an international code of practice for dosimetry based on standards of absorbed dose to water*, Technical Reports Series No. 398, IAEA (2000), Vienna.

[41] P. R. Almond, P. J. Biggs, B. M. Coursey, W. F. Hanson, H. M. Saiful, R. Nath, and D. W. O. Rogers, "Report of the American Association of Physicists in Medicine Task Group No. 51: Protocol for clinical reference dosimetry of high-energy photon and electron beams," Med. Phys. **26**, 1847 (1999).

[42] F. Araki, "Monte Carlo-based correction factors for ion chamber dosimetry in heterogeneous phantoms for megavoltage photon beams," Phys. Med. Biol. **57**, 7615 (2012).

[43] A. Niroomand-Rad, C. R. Blackwell, B. M. Coursey, K. P. Gall, J. M. Galvin, W. L. McLaughlin, A. S. Meigooni, R. Nath, J. E. Rodgers, and C. G. Soares, "Report of the American Association of Physicists in Medicine Task Group No. 55: Radiochromic film dosimetry," Med. Phys. **25**, 2093 (1998).

[44] N. Jornet, P. Carrasco, D. Jurado, A. Ruiz, T. Eudaldo, and M. Ribas, "Comparison study of MOSFET detectors and diodes for entrance in vivo dosimetry in 18 MV x-ray beams," Med. Phys. **31**, 2534 (2004).

[45] A. F. McKinlay, *Thermoluminescent dosimetry. Medical Physics Handbooks*, edited by A. F. McKinlay (Adam Hilger Ltd, The Institute of Physics, Techno House, Redcliffe Way, Bristol BS1 6NX, 1981).

[46] P. N. Mobit, G. A. Sandison, and A. E. Nahum, "Electron fluence perturbation correction factors for solid state detectors irradiated in megavoltage electron beams," Phys. Med. Biol. **45**, 255 (2000).

[47] P. Mobit, "The use of Monte Carlo simulations for accurate dose determination with thermoluminescence dosemeters in radiation therapy beams," Radiat. Prot. Dosim. **101**, 383 (2002), 13th International Conference on Solid State Dosimetry, Athens, Greece, Jul 09-13, 2001.

[48] P. Bilski, P. Olko, B. Burgkhardt, and E. Piesch, "Ultra-thin LiF:Mg,Cu,P detectors for beta-dosimetry," Radiat. Meas. **24**, 439 (1995), international Symposium on Luminescent Detectors and Transformers of Ionizing Radiation, Tallinn, Estonia, Sep 25-29, 1994.

[49] J. P. Lina, T. C. Chua, S. Y. Lina, and M. T. Liub, "Skin dose measurement by using ultra-thin TLDs," Applied Radiation and Isotopes **55**, 383 (2001).

[50] N. Lee, C. Chuang, J. Quivey, T. Phillips, P. Akazawa, L. Verhey, and P. Xia, "Skin toxicity due to intensity-modulated radiotherapy for head-and-neck carcinoma," Int. J. Radiat. Oncol. Biol. Phys. **53**, 630 (2002).

[51] S. Stathakis, J. Li, K. Paskalev, J. Yang, L. Wang, and C. Ma, "Ultra-thin TLDs for skin dose determination in high energy photon beams," Phys. Med. Biol. **51**, 3549 (2006).

[52] A. Ahnesjö and M. M. Aspradakis, "Dose calculations for external photon beams in radiotherapy," Phys. Med. Biol. **44**, R99 (1999).

[53] N. Papanikolaou and S. Stathakis, "Dose-calculation algorithms in the context of inhomogeneity corrections for high energy photon beams," Med. Phys. **36**, 4765 (2009).

[54] T. Knöös, E. Wieslander, L. Cozzi, C. Brink, A. Fogliata, D. Albers, A. Nyström, and S. Lassen, "Comparison of dose calculation algorithms for treatment planning in external photon beam therapy for clinical situations," Phys. Med. Biol. **51**, 5785 (2006).

[55] M. Aspradakis, R. Morrison, N. Richmond, and A. Steele, "Experimental verification of convolution/superposition photon dose calculations for radiotherapy treatment planning," Phys. Med. Biol. **48**, 2873 (2003).

[56] T. Knöös, C. Ceberg, L. Weber, and P. Nilsson, "The dosimetric verification of a pencil-beam based treatment planning system," Phys. Med. Biol. **39**, 1609 (1994).

[57] T. Knöös, A. Ahnesjö, P. Nilsson, and L. Weber, "Limitations of a pencil-beam approach to photon dose calculations in lung tissue," Phys. Med. Biol. **40**, 1411 (1995).

[58] A. Fogliata, G. Nicolini, A. Clivio, E. Vanetti, P. Mancosu, and L. Cozzi, "On the dosimetric behaviour of photon dose calculation algorithms in the presence of simple geometric heterogeneities: comparison with Monte Carlo calculations," Phys. Med. Biol. **52**, 1363 (2007).

[59] M. Fragoso, N. Wen, S. Kumar, D. Liu, S. Ryu, B. Movsas, A. Munther, and I. Chetty, "Dosimetric verification and clinical evaluation of a new commercially available Monte Carlo-based dose algorithm for application in stereotactic body radiation therapy (SBRT) treatment planning," Phys. Med. Biol. **55**, 4445 (2007).

[60] R. M. Arnfield, C. H. Siantar, J. Siebers, P. Garmon, L. Cox, and R. Mohan, "The impact of electron transport on the accuracy of computed dose," Med. Phys. **27**, 1266 (2000).

[61] E. Sterpin, M. Tomsej, B. De Smedt, N. Reynaert, and S. Vynckier, "Monte Carlo evaluation of the AAA treatment planning algorithm in a heterogeneous multilayer phantom and IMRT clinical treatments for an Elekta SL25 linear accelerator," Med. Phys. **34**, 1665 (2007).

[62] F. García-Vicente, A. Miñambres, I. Jerez, I. Modolell, L. Pérez, and J. Torres, "Experimental validation tests of fast fourier transform convolution and multigrid superposition algorithms for dose calculation in low-density media," Radiother. Oncol. **67**, 239 (2003).

[63] P. Carrasco, N. Jornet, M. A. Duch, L. Weber, M. Ginjaume, T. Eudaldo, D. Jurado, A. Ruiz, and M. Ribas, "Comparison of dose calculation algorithms in phantoms with lung equivalent heterogeneities under conditions of lateral electronic disequilibrium," Med. Phys. **31**, 2899 (2004).

[64] M. Engelsman, E. Damen, P. Koken, A. Van't Veld, K. Van Ingen, and B. Mijnheer, "Impact of simple tissue inhomogeneity correction algorithms on conformal radiotherapy of lung tumours," Radiother. Oncol. **60**, 299 (2001).

[65] A. Jones, I. Das, and F. Jones, "A Monte Carlo study of IMRT beamlets in inhomogeneous media," Med. Phys. **30**, 296 (2003).

[66] J. Chow, E. Wong, J. Chen, and J. Van Dyk, "Comparison of dose calculation algorithms with Monte Carlo methods for photon arcs," Med. Phys. **30**, 2686 (2003).

[67] E. E. Klein, L. M. Chin, R. K. Rice, and B. J. Mijnheer, "The influence of air cavities on interface doses for photon beams," Int. J. Radiat. Oncol. Biol. Phys. **27**, 419 (1993).

[68] P. J. Keall, J. V. Siebers, R. Jeraj, and R. Mohan, "Radiotherapy dose calculations in the presence of hip prostheses," Med. Dos. **28**, 102 (2003).

[69] P. Carrasco, N. Jornet, M. A. Duch, V. Panettieri, L. Weber, T. Eudaldo, M. Ginjaume, and M. Ribas, "Comparison of dose calculation algorithms in slab phantoms with cortical bone equivalent heterogeneities," Med. Phys. **34**, 3323 (2007).

[70] K. Ono, S. Endo, K. Tanaka, M. Hoshi, and Y. Hirokawa, "Dosimetric verification of the anisotropic analytical algorithm in lung-equivalent heterogeneities with and without bone-equivalent heterogeneities," Med. Phys. **37**, 4456 (2010).

[71] G. Rodrigues, M. Lock, D. D'Souza, E. Yu, and J. Van Dyk, "Prediction of radiation pneumonitis by dose-volume histogram parameters in lung cancer: a systematic review," Radiother. Oncol. **71**, 127 (2004).

[72] I. J. Das and F. Khan, "Backscatter dose perturbation at high atomic number interfaces in megavoltage photon beams." Med. Phys. **16**, 367 (1989).

[73] O. A. Sauer, "Calculation of dose distributions in the vicinity of high-Z interfaces for photon beams," Med. Phys. **22**, 1685 (1995).

[74] M. Urie, M. Goitein, W. R. Holley, and G. T. Y. Chen, "Degradation of the Bragg peak due to inhomogeneities," Phys. Med. Biol. **31**, 1 (1986).

[75] M. Goitein and J. M. Sisterson, "The influence of thick inhomogeneities on charged particle beams," Radiat. Res. **74**, 217 (1978).

[76] U. Schneider, B. Schaffner, T. Lomax, E. Pedroni, and A. Tourowsky, "A technique for calculating range spectra of charged particle beams distal to thick inhomogeneities," Med. Phys. **25**, 457 (1998).

[77] G. O. Sawakuchi, U. Titt, D. Mirkovic, and R. Mohan, "Density heterogeneities and the influence of multiple Coulomb and nuclear scatterings on the Bragg peak distal edge of proton therapy beams," Phys. Med. Biol. **53**, 4605 (2008).

[78] H. Szymanowski and U. Oelfke, "Two-dimensional pencil beam scaling: an improved proton dose algorithm for heterogeneous media," Phys. Med. Biol. **47**, 3313 (2002).

[79] D. Pflugfelder, J. J. Wilkens, H. Szymanowski, and U. Oelfke, "Quantifying lateral tissue heterogeneities in hadron therapy," Med. Phys. **34**, 1506 (2007).

[80] T. Yamashita, T. Akagi, T. Aso, A. Kimura, and T. Sasaki, "Effect of inhomogeneity in a patient's body on the accuracy of the pencil beam algorithm in comparison to Monte Carlo," Phys. Med. Biol. **57**, 7673 (2012).

[81] L. Hong, M. Goitein, M. Bucciolini, R. Comiskey, B. Gottschalk, S. Rosenthal, C. Serago, and M. Urie, "A pencil beam algorithm for proton dose calculations," Phys. Med. Biol. **41**, 1305 (1996).

[82] B. Bednarz, J. Daartz, and H. Paganetti, "Dosimetric accuracy of planning and delivering small proton therapy fields," Phys. Med. Biol. **55**, 7425 (2010).

[83] N. Dogan, J. V. Siebers, and P. J. Keall, "Clinical comparison of head and neck and prostate IMRT plans using absorbed dose to medium and absorbed dose to water," Phys. Med. Biol. **51**, 4967 (2006).

[84] B. Walters, R. Kramer, and I. Kawrakow, "Dose to medium versus dose to water as an estimator of dose to sensitive skeletal tissue," Phys. Med. Biol. **55**, 4535 (2010).

[85] H. Paganetti, "Dose to water versus dose to medium in proton beam therapy," Phys. Med. Biol. **54**, 4399 (2009).

[86] H. Liu and P. Keall, "D_m rather than D_w should be used in Monte Carlo treatment planning," Med. Phys. **29**, 922 (2002).

[87] M. Fippel and F. Nüsslin, "Comments on *converting absorbed dose to medium to absorbed dose to water for monte carlo based photon beam dose calculations*," Phys. Med. Biol. **45**, 17 (2000).

[88] W. Schneider, T. Bortfeld, and W. Schlegel, "Correlation between CT numbers and tissue parameters needed for Monte Carlo simulations of clinical dose distributions," Phys. Med. Biol. **45**, 459 (2000).

[89] F. Salvat, J. Fernández-Varea, and J. Sempau, PENELOPE-*2008: A Code System for Monte Carlo Simulation of Electron and Photon Transport*, edited by W. proceedings (OECD/Nuclear Energy Agency, Issy-les-Molineaux, France, 2008).

[90] J. Baró, J. Sempau, J. M. Fernández-Varea, and F. Salvat, "PENELOPE: an algorithm for Monte Carlo simulation of the penetration and energy loss of electrons and positrons in matter," Nucl. Instr. Methods Phys. Res. B **100**, 31 (1995).

[91] J. Sempau, A. Badal, and L. Brualla, "A PENELOPE-based system for the automated Monte Carlo simulation of clinacs and voxelized geometries—application to far-from-axis fields," Med. Phys. **38**, 5887 (2011).

[92] O. Chibani and C. Ma, "On the discrepancies between Monte Carlo dose calculations and measurements for the 18 MV Varian photon beam," Med. Phys. **34**, 1206 (2007).

[93] D. Sheikh-Bagheri and W. O. Rogers, "Sensitivity of megavoltage photon beam Monte Carlo simulations to electron beam and other parameters," Med. Phys. **29**, 379 (2002).

[94] A. Tzedakis, J. Damilakis, M. Mazonakis, J. Stratakis, H. Varveris, and N. Gourtsoyiannis, "Influence on initial electron beam parameters on Monte Carlo calculated absorbed dose distributions for radiotherapy photon beams," Med. Phys. **31**, 907 (2004).

[95] M. K. Fix, P. J. Keall, K. Dawson, and J. V. Siebers, "Monte Carlo source model for photon beam radiotherapy: photon source characteristics," Med. Phys. **34**, 3106 (2004).

[96] J. Pena, D. González-Castaño, and F. Gómez, "Automatic determination of primary elecron beam parameters in Monte Carlo simulation," Med. Phys. **34**, 1076 (2007).

[97] D. Sawkey and B. Faddegon, "Determination of electron energy, spectral width, and beam divergence at the exit window for clinical megavoltage x-ray beams," Med. Phys. **36**, 698 (2009).

[98] G. Ding, "Energy spectra, angular spread, fluence profiles and dose distributions of 6 and 18 MV photon beams: results of Monte Carlo simulations for a Varian 2100EX accelerator," Phys. Med. Biol. **47**, 1025 (2002).

[99] F. Verhaegen and J. Seuntjens, "Monte Carlo modelling of external radiotherapy photon beams," Phys. Med. Biol. **48**, 107 (2003).

[100] I. Kawrakow and M. Fippel, "Investigation of variance reduction techniques for Monte Carlo photon dose calculation using XVMC." Phys. Med. Biol. **45**, 2163 (2000).

[101] K. Bush, S. F. Zavgorodni, and W. A. Beckham, "Azimutal particle redistribution for the reduction of latent phase-space variance in Monte Carlo simulations," Phys. Med. Biol. **52**, 4345 (2007).

[102] L. Brualla, F. Salvat, and R. Palanco-Zamora, "Efficient Monte Carlo simulation of multileaf collimators using geometry-related variance-reduction techniques," Phys. Med. Biol. **54**, 4131 (2009).

[103] L. Brualla, F. Salvat, E. Franchisseur, S. García-Pareja, and A. Lallena, "Advanced variance reduction techniques applied to Monte Carlo simulation of linacs," http://www.maestro-research.org/idf-maestro/monte-carlo/14.brualla1.pdf (Institut Gustave Roussy, 2008) mAESTRO project – Monte Carlo.

[104] S. Agostinelli *et al.*, "GEANT4—a simulation toolkit," Nucl. Instrum. Methods Phys. Res. A **506**, 250 (2003).

[105] C. Z. Jarlskog and H. Paganetti, "Physics settings for using the Geant4 toolkit in proton therapy," IEEE Trans. Nucl. Sci. **55**, 1018 (2008).

[106] H. Paganetti, H. Jiang, S.-Y. Lee, and H. Kooy, "Accurate Monte Carlo simulations for nozzle design, commissioning and quality assurance for a proton radiation therapy facility," Med. Phys. **31**, 2107 (2004).

[107] M. Testa, J. Schuemann, H. M. Lu, and H. Paganetti, "Experimental validation of the TOPAS Monte Carlo system against phantom dose measurements in proton therapy," (2013), *submitted*.

[108] J. Ramos-Méndez, J. Perl, B. Faddegon, J. Schuemann, and H. Paganetti, "Geometrical splitting technique to improve the computational efficiency in Monte Carlo calculations for proton therapy," Med. Phys. **40**, 041718 (2013).

[109] F. Wu, Z. Zha, J. Li, and Z. Zhu, "LiF:Mg,Cu,P thin dosemeter for skin dose measurement," Radiat. Prot. Dosim. **33**, 331 (1990).

[110] G. G. Cai, F. Wu, Z. Y. Zha, and J. Li, "Beta energy dependence of LiF:Mg,Cu,P thermoluminescent films on thickness of sensitive layer," Radiat. Prot. Dosim. **40**, 53 (1992).

[111] Y. S. Horowitz, "LiF:Mg,Ti *vs.* LiF:Mg,Cu,P: the competition heats up." Radiat. Prot. Dosim. **47**, 135 (1993).

[112] P. Bilski, "Lithium fluoride: from LiF:Mg,Ti to LiF:Mg,Cu,P," Radiat. Prot. Dosim. **100**, 199 (2002), 13th International Conference on Solid State Dosimetry, ATHENS, GREECE, JUL 09-13, 2001.

[113] L. Duggan, C. Hood, H. Warren-Forward, M. Haque, and T. Kron, "Variations in dose response with x-ray energy of LiF:Mg,Cu,P thermoluminescence dosimeters: implications for clinical dosimetry," Phys. Med. Biol. **49**, 3831 (2004).

[114] L. Duggan and T. Kron, "Dose linearity of LiF:Mg,Ti and LiF:Mg,Cu,P in radiotherapy: Effect of time between dose and evaluation," Radiat. Prot. Dosim. **85**, 397 (1999).

[115] M. Budzanowski, J. C. Saez-Vergara, J. M. Gómez-Ros, A. M. Romero-Guitierrez, and E. Ryba, "The fading of different peaks in LiF:Mg,Cu,P (MCP-N and GR-200A) TL detectors," Radiat. Meas. **29**, 361 (1998), 3rd International Symposium on Luminescent Detectors and Transformers of Ionising Radiation (LUMDETR 97), USTRON, POLAND, OCT 06-10, 1997.

[116] M. Ptaszkiewicz, "Long-term fading of LiF:Mg,Cu,P and LiF:Mg,Ti thermoluminescence detectors with standard and modified activator composition," Radiat. Meas. **42**, 605 (2007), 6th European Conference on Luminescent Detectors and Transformers of Ionizing Radiation, Lviv, Ukraine, June, 2006.

[117] C. K. Harris, H. R. Elson, M. A. S. Lamba, and A. E. Foster, "A comparison of the effectiveness of thermoluminescent crystals LiF:Mg,Ti and LiF:Mg,Cu,P for clinical dosimetry," Med. Phys. **24**, 1527 (1997).

[118] P. Olko, P. Bilski, M. Budzanowski, M. Waligorski, A. Fasso, and N. Ipe, "Modelling of the thermoluminescence response of LiF:Mg,Cu,P (MCP-N) detectors after doses of low energy photons," Radiat. Prot. Dosim. **84**, 103 (1999), 12th International Conference on Solid State Dosimetry, BURGOS, SPAIN, JUL 05-10, 1998.

[119] S. D. Davis, C. K. Ross, P. N. Mobit, L. Van der Zwan, W. J. Chase, and K. R. Shortt, "The response of LiF thermoluminescence dosemeters to photon beams in the energy range from 30 kV X rays to Co-60 gamma rays," Radiat. Prot. Dosim. **106**, 33 (2003).

[120] P. N. Mobit, P. Mayles, and A. E. Nahum, "The quality dependence of LiF TLD in megavoltage photon beams: Monte Carlo simulations and experiments," Phys. Med. Biol. **41**, 387 (1996).

[121] M. Ginjaume, X. Ortega, M. A. Duch, N. Jornet, and A. Sánchez-Reyes, "Characteristics of LiF:Mg,Cu,P for clinical applications," Radiat. Prot. Dosim. **85**, 389 (1999).

[122] J. L. Kim, J. I. Lee, Y. H. Ji, B. H. Kim, J. S. Kim, and S. Y. Chang, "Energy responses of the LiF series TL pellets to high-energy photons in the energy range

from 1.25 to 21 MV," *14th International Conference on Soild State Dosimetry, New Haven, CT, JUN 27-JUL 02, 2004*, Radiat. Prot. Dosim. **119**, 353 (2006).

[123] A. Bartolotta, M. Brai, V. Caputo, R. Diliberto, D. Dimariano, G. Ferrara, P. Puccio, and A. S. Santamaria, "The response behavior of LiF:Mg,Cu,P thermoluminescence dosimeters to high-energy electron beams used in radiotherapy," Phys. Med. Biol. **40**, 211 (1995).

[124] P. N. Mobit, A. E. Nahum, and P. Mayles, "The energy correction factor of LiF thermoluminescent dosemeters in megavoltage electron beams: Monte Carlo simulations and experiments," Phys. Med. Biol. **41**, 979 (1996).

[125] V. Robar, C. Zankowski, M. Olivares-Pla, and E. B. Podgorsak, "Thermoluminescent dosimetry in electron beams: energy dependence," Med. Phys. **23**, 667 (1996).

[126] V. Nelsona, D. McLeanb, and L. Holloway, "Thermoluminescent dosimetry (TLD) for megavoltage electron beam energy determination," Radiat. Meas. **45**, 698 (2010), proceedings of the 7th European Conference on Luminescent Detectors and Transformers of Ionizing Radiation (LUMDETR 2009).

[127] P. Bilski, P. Olko, B. Burgkhardt, E. Piesch, and M. P. R. Waligorski, "Thermoluminescence efficiency of LiF:Mg,Cu,P (MCP-N) detectors to photons, beta-electrons, alpha-particles and thermal-neutrons," Radiat. Prot. Dosim. **55**, 31 (1994).

[128] D. Nahajowski, E. Gora, B. Rozwadowska-Bogusz, B. Lesiak, J.and Polak, D. Kabat, P. Zawadzki, and M. P. R. Waligorski, "Evaluation of the relative effectiveness of LiF-based TL detectors for electron radiotherapy beams over the energy range 6-20 MeV," Radiat. Meas. **43**, 879 (2008), 15th International Conference on Solid State Dosimetry, Delft, Netherlands, Jul 08-13, 2007.

[129] P. Olko, P. Bilski, W. Gieszczyk, L. Grzanka, and B. Obryk, "Microdosimetric analysis of response of LiF:Mg,Cu,P (MCP-N) TL detectors for alpha-particles and ultra-high doses of gamma-rays," Radiat. Meas. **46**, 1349 (2011).

[130] S. Pérez, M. Ginjaume, X. Ortega, M. A. Duch, and M. Roig, "Extremity and whole-body dosemeters for beta and beta-gamma fields based on LiF:Mg,Cu,P thin detectors," Radiat. Meas. **46**, 1349 (2011).

[131] M. Ginjaume, S. Pérez, X. Ortega, and M. A. Duch, "Comparison of two extremity dosemeters based on LiF:Mg,Cu,P thin detectors for mixed beta-gamma fields," Radiat. Prot. Dosim. **120**, 316 (2006).

[132] B. Obryk, P. Bilski, M. Budzanowski, M. Fuerstner, C. Ilgner, F. Jaquenod, P. Olko, M. Puchalska, and H. Vincke, "The response of different types of TL lithium fluoride detectors to high-energy mixed radiation fields," Radiat. Meas. **43**, 1144 (2008), 15th International Conference on Solid State Dosimetry, Delft, Netherlands, Jul 08-13, 2007.

[133] E. Carinou, A. Boziari, P. Askounis, A. Mikulis, and V. Kamenopoulou, "Energy dependence of TLD-100 and MCP-N detectors," Radiat. Meas. **43**, 599 (2008).

[134] M. J. Lawless, S. Junell, C. Hammer, and L. A. DeWerd, "Response of TLD-100 in mixed fields of photons and electrons," Med. Phys. **40**, 012103 (2013).

[135] P. Bilski and M. Puchalska, "Relative efficiency of TL detectors to energetic ion beams," Radiat. Meas. **45**, 1495 (2010).

[136] E. F. Mische and S. W. S. McKeever, "Mechanisms of supralinearity in lithium fluoride thermoluminescence dosemeters," Radiat. Prot. Dosim. **29**, 159 (1989).

[137] Y. S. Horowitz, S. Mahajna, L. Oster, Y. Weizman, D. Satinger, and D. Yossian, "The unified interaction model applied to the gamma-induced supralinearitty and sensitisation of peak 4 and 5 in LiF:Mg,Ti (TLD-100)," Radiat. Prot. Dosim. **78**, 169 (1998).

[138] C. G. Soares, S. Trichter, and S. Devic, *Clinical Dosimetry measurements in radiotherapy*, edited by D. W. O. Rogers and J. E. Cygler (Medical Physics Publishing, Madison, WI, 2009) Chap. Radiochromic film, pp. 759–813.

[139] M. Fuss, E. Sturtewagen, C. De Wagter, and D. Georg, "Dosimetric characterization of GafChromic EBT film and its implication on film dosimetry quality assurance," Phys. Med. Biol. **52**, 4211 (2007).

[140] O. A. Zeidan, S. A. Stephenson, S. L. Meeks, T. H. Wagner, T. R. Willoughby, P. A. Kupelian, and K. M. Langen, "Characterization and use of EBT radiochromic film for IMRT dose verification," Med. Phys. **33**, 4064 (2006).

[141] C. Huet, S. Dagois, S. Derreumaux, F. Trompier, C. Chenaf, and I. Robbes, "Characterization and optimization of EBT2 radiochromic film dosimetry system for precise measurements of output factors in small fields used in radiotherapy," Radiat. Meas. **47**, 40 (2012).

[142] H. C. L. Richley, A. C. John and S. Fletcher, "Evaluation and optimization of the new EBT2 radiochromic film dosimetry system for patient dose verification in radiotherapy," Phys. Med. Biol. **55**, 2601 (2010).

[143] J. G. H. Sutherlanda and D. W. O. Rogers, "Monte Carlo calculated absorbed-dose energy dependence of EBT and EBT2 film," Med. Phys. **37**, 1110 (2010).

[144] J. Baró, J. Sempau, F. Salvat, and J. M. Fernández-Varea, "PENELOPE: an algorithm for Monte Carlo simulation of the penetration and energy-loss of electrons and positrons in matter," Nucl. Instrum. Methods Phys. Res. Section B **100**, 31 (1995).

[145] J. Sempau and A. Badal, "`penEasy`, a modular main program amb voxelised geometry package (v.2008-06-15). – http://www.upc.edu/inte/descarregues.php," (2005).

[146] G. A. Failla, T. Wareing, Y. Archambault, and S. Thompson, *Acuros XB: Advanced Dose Calculation for the* ECLIPSE *Treatment Planning System*, Varian Medical System, Palo Alto, CA (2010).

[147] T. Han, J. K. Mikell, M. Salehpour, and F. Mourtada, "Dosimetric comparison of Acuros XB deterministic radiation transport method with Monte Carlo and model-based convolution methods in heterogeneous media," Med. Phys. **38**, 2651 (2011).

[148] T. Han, F. Mourtada, K. Kisling, J. K. Mikell, D. Followill, and R. Howell, "Experimental validation of deterministic Acuros XB algorithm for IMRT and VMAT dose calculations with the Radiological Physics Center's head and neck phantom," Med. Phys. **39**, 2193 (2012).

[149] J. Sievinen, W. Ulmer, and W. Kaissl, "AAA photon dose calculation model in Eclipse," Tech. Rep. (2005).

[150] I. Kawrakow and D. W. O. Rogers, "The EGSnrc code system: Monte Carlo simulation of electron and photon transport," Technical Report PIRS-701 (National Research Council of Canada, Ottawa, 2000).

[151] A. Fogliata, G. Nicolini, A. Clivio, E. Vanetti, P. Mancosu, and L. Cozzi, "Dosimetric validation of the Acuros XB advanced dose calculation algorithm: fundamental characterization in water," Phys. Med. Biol. **56**, 1879 (2011).

[152] A. Fogliata, G. Nicolini, A. Clivio, E. Vanetti, and L. Cozzi, "Dosimetric evaluation of Acuros XB advanced dose calculation algorithm in heterogeneous media," Radiat. Oncol. **6**, 82 (2011).

[153] K. Bush, M. I. Gagne, S. Zavgorodni, W. Ansbacher, and W. Beckham, "Dosimetric validation of Acuros XB with Monte Carlo methods for photon dose calculations," Med. Phys. **38**, 2208 (2011).

[154] L. Hoffmann, M. B. Jorgensen, L. P. Muren, and J. B. Peterson, "Clinical validation of the Acuros XB photon dose calculation algorithm, a grid-based boltzmann equation solver," Acta Oncol. **51**, 376 (2011).

[155] A. Fogliata, G. Nicolini, A. Clivio, E. Vanetti, and L. Cozzi, "Accuracy of Acuros XB and AAA dose calculation for small fields with reference to RapidArc stereotactic treatments," Med. Phys. **38**, 6228 (2011).

[156] T. Han, D. Followill, J. K. Mikell, R. Repchack, A. Molineu, R. Howell, M. Salehpour, and F. Mourtada, "Dosimetric impact of Acuros XB deterministic radiation transport algorithm for heterogeneous dose calculation in lung cancer," Med. Phys. **40**, 051710 (2013).

[157] M. W. K. Kan, L. H. T. Leung, and P. K. N. Yu, "Verification and dosimetric impact of Acuros XB algorithm on intensity modulated stereotactic radiotherapy for locally persistent nasopharyngeal carcinoma," Med. Phys. **39**, 4705 (2012).

[158] M. W. K. Kan, L. H. T. Leung, R. W. K. So, and P. K. N. Yu, "Experimental verification of the Acuros XB and AAA dose calculation adjacent to heterogeneous media for IMRT and RapidArc of nasopharygeal carcinoma," Med. Phys. **40**, 031714 (2013).

[159] L. Tillikainen, S. Siljamäli, H. Helminen, J. Alakuijala, and J. Pyyry, "Determination of parameters for multiple-source model of megavoltage photon beams using optimization methods," Phys. Med. Biol. **52**, 1441 (2007).

[160] A. Fogliata, G. Nicolini, A. Clivio, E. Vanetti, and L. Cozzi, "On the dosimetric impact of inhomogeneity management in theAcuros XB algorithm for breast treatment," Radiat. Oncol. **6**, 103 (2011).

[161] S. A. Lloyd and W. Ansbacher, "Evaluation of an analytic linear Boltzmann transport equation solver for high-density inhomogeneities," Med. Phys. **40**, 011707 (2012).

[162] H. Paganetti, B. S. Athar, M. Moteabbed, J. Adams, U. Schneider, and T. I. Yock, "Assessment of radiation-induced second cancer risks in proton therapy and IMRT for organs inside the primary radiation field," Phys. Med. Biol. **57**, 6047 (2012).

[163] A. M. Allen, T. Pawlicki, L. Dong, E. Fourkal, M. Buyyounouski, K. Cengel, J. Plastaras, M. K. Bucci, T. I. Yock, L. Bonilla, R. Price, E. E. Harris, and A. A. Konski, "An evidence-based review of proton beam therapy: the report of ASTRO's emerging technology committee," Radiother. Oncol. **103**, 8 (2012).

[164] M. Yoon, D. H. Shin, J. Kim, J. W. Kim, D. W. Kim, S. Y. Park, S. B. Lee, J. Y. Kim, H. J. Park, B. K. Park, and S. H. Shin, "Craniospinal irradiation techniques: A dosimetric comparison of proton beams with standard and advanced photon radiotherapy," Int. J. Radiat. Oncol. Biol. Phys. **81**, 637 (2011).

[165] B. Schaffner, E. Pedroni, and T. Lomax, "Dose calculation models for proton treatment planning using a dynamic beam delivery system: an attempt to include density heterogeneity effects in the analytical dose calculation," Phys. Med. Biol. **44**, 27 (1999).

[166] P. Petti, "Differential pencil beam dose calculations for charged particles," Med. Phys. **19**, 137 (1992).

[167] D. C. Westerly, X. Mo, W. A. Tomé, T. R. Mackie, and P. M. Deluca, "A generalized 2D pencil beam scaling algorithm for proton dose calculation in heterogeneous slab geometries," Med. Phys. **40**, 061706 (2013).

[168] J. Daartz, M. Engelsman, H. Paganetti, and M. R. Bussière, "Field size dependence of the output factor in passively scattered proton therapy: Influence of range, modulation, air gap, and machine settings," Med. Phys. **36**, 3205 (2009).

[169] D. Fontenot, W. D. Newhauser, C. Bloch, R. A. White, U. Titt, and G. Starkschall, "Determination of output factors for small proton therapy fields," Med. Phys. **34**, 489 (2007).

[170] U. Titt, Y. Zheng, O. N. Vassiliev, and W. D. Newhauser, "Monte Carlo investigation of collimator scatter of proton-therapy beams produced using the passive scattering method," Phys. Med. Biol. **53**, 487 (2008).

[171] B. Bednarz, J. Daartz, and H. Paganetti, "Dosimetric accuracy of planning and delivering small proton therapy fields," Phys. Med. Biol. **55**, 7425 (2010).

[172] A. Tourovsky, A. J. Lomax, U. Schneider, and E. Pedroni, "Monte Carlo dose calculations for spot scanned proton therapy," Phys. Med. Biol. **50**, 971 (2005).

[173] M. Kooy, S. J. Rosenthal, M. Engelsman, A. Mazal, R. L. Slopsema, H. Paganetti, and J. B. Flanz, "The prediction of output factors for spreadout proton bragg peak fields in clinical practice," Phys. Med. Biol. **50**, 5847 (2005).

[174] K. Parodi, H. Paganetti, E. Cascio, J. B. Flanz, A. A. Bonab, N. M. Alpert, K. Lohman, and T. Bortfeld, "PET/CT imaging for treatment verification after proton therapy: a study with plastic phantoms and metallic implants," Med. Phys. **34**, 419 (2007).

[175] D. J. Sheskin, *Handbook of parametric and nonparametric statistical procedures*, 3rd ed., edited by Chapman and Hall/CRC (CRC Press LLC, 2000 N. W. Corporate Blvd., Boca Raton, Florida 33431 (USA), 2004).